ISOBUTANOL PRODUCTION IN A BIOREACTOR FOR INCOMPATIBLE GASES (BIG)

By

YANGMU CHLOE LIU

A DISSERTATION

Submitted to
Michigan State University
in partial fulfillment of the requirements
for the degree of

Chemical Engineering—Doctor of Philosophy

2014

ABSTRACT

ISOBUTANOL PRODUCTION IN A BIOREACTOR FOR INCOMPATIBLE GASES (BIG)

By

YANGMU CHLOE LIU

Electrofuels are carbon-neutral, renewable transportation fuels generated using non-photosynthetic CO_2 fixation. Biological conversion of H_2, CO_2 and O_2 into alcohols is emerging as a promising strategy for producing electrofuels while reducing greenhouse gas emission. However, development of this process presents significant bioreactor-design challenges. First, these fermentations have unusually high demands for gas mass transfer. Second, the need to simultaneously deliver H_2 and O_2 creates safety issues, because these gases are incompatible, forming a flammable mixture over the range of 4 to 94% H_2. Third, alcohols are typically inhibitory to the microbial biocatalysts, making their *in situ* removal desirable for continuous bioreactor operation.

This dissertation describes development of a novel Bioreactor for Incompatible Gases (BIG) to address these challenges. The BIG features a hollow fiber configuration, in which the microbial biocatalysts are immobilized in the porous fiber walls. A liquid phase containing microbubbles of one gaseous reactant is pumped through the hollow fibers, and a gas phase containing another gaseous reactant(s) incompatible with the first is maintained outside the fibers. In this way, rapid mass transfer to the immobilized cells of both gaseous reactants is achieved without creating hazardous gas mixtures. *In situ* product removal can be achieved from the liquid stream (for nonvolatile products) and/or the gas stream (for volatile products).

A prototype bench-scale BIG was designed, fabricated, and integrated with an Opto22-based control system that monitored and controlled the composition of the gas phase, dissolved

oxygen concentration in the liquid phase, and temperature. The control system was programmed to make intelligent operational decisions in response to process contingencies. The BIG system was inoculated with an isobutanol (IBT)-producing strain of *Ralstonia eutropha* and operated stably for up to 19 days, during which continuous, autotrophic IBT production from H_2, CO_2 and O_2 was achieved for the first time.

A dynamic mathematical model was developed to describe the interplay of multispecies and multidirectional gas mass transfer, along with complex cellular kinetics involving mixed-gas substrates. The simulation results were used to interpret experimental findings and simulate BIG performance under a range of operating conditions. The experimental and modeling results established the unexpected finding that *R. eutropha* cells both produced and consumed IBT, depending on the local H_2 concentration. The BIG prototype reactor and associated mathematical models are generic and could describe production of a variety of biofuels from incompatible gases.

To my parents,
and
To Aaron

ACKNOWLEDGEMENTS

There are so many people without whose help and support I would not have made it this far. First and foremost I would like to thank my advisor R. Mark Worden for the opportunity to join his lab, and for his support, guidance and patience throughout my study. Your optimism has helped me through the most difficult part of this project. I would also like to thank Scott Calabrese-Barton, Claire Vieille and Dennis Miller for their time and guidance as members on my Ph.D. committee.

Part of this dissertation is the result of collaboration with my former colleague Soumen Maiti, whom I would like to thank for his contribution to the experimental work. I would also like to thank the undergraduate students I have worked with on the project, Derek Montgomery, Jillian Robertson, and Dexter Gregg, for their help.

I would also like to express my gratitude to people who have helped me with various aspects of my work: Anthony Sinskey's research group at Massachusetts Institute of Technology for their help in understanding the metabolic characteristics of the biocatalyst, especially Chris Brigham and Jingnan Lu; Carol Flegler for her indispensable assistance with microscopy imaging; and Lee Alexander for training me in various sterile techniques.

I know I would not be where I am without my parents. Thank you Mom and Dad for making me believe that I am capable of anything I put my mind to, and for believing in me. Thank you for doing what might be the most difficult thing for a parent—letting your only daughter move half way across the globe to a country you've never been to, knowing fully that our conversations will be subjected to the whims of the intercontinental internet connection.

Special thanks to Aaron for his love, support and words of encouragement. You have been the best companion I could have asked for in my life.

Finally, I wish to extend my sincerely gratitude to all my family and friends for being there for me during the past few years.

TABLE OF CONTENTS

LIST OF TABLES

LIST OF FIGURES

KEY TO SYMBOLS

$A_{membrane1}$	Membrane inner area
$A_{membrane2}$	Membrane outer area
δ	Membrane thickness
$C_{reservoir,O_2}$	O_2 concentration in the reservoir
D_{app}	Apparent diffusion coefficient
D_{app,O_2}	Apparent O_2 diffusion coefficient
D_{app,H_2}	Apparent H_2 diffusion coefficient
D_{app,CO_2}	Apparent (measured) CO_2 diffusion coefficient
DCW	Dry cell weight
D_e	Effective diffusion coefficient (in biofilm)
D_{iw}	Diffusion coefficient of solute in solvent
D_M	Membrane diffusion coefficient
D_{M,O_2}	O_2 membrane diffusion coefficient
D_{M,H_2}	H_2 membrane diffusivity
D_{M,CO_2}	CO_2 membrane diffusivity
DO	Dissolved oxygen
ϵ	Membrane porosity
F_L	Flow rate in the lumen
F_S	Flow rate in the shell

IBT	Isobutanol
k_{H,CO_2}	Henry's coefficient of CO_2 at 298K
L	Fiber length [m]
N	Number of fibers
$N\|_{r=R_1}$	Diffusion flux at membrane inner surface
$P_{reservoir,CO_2}$	CO_2 partial pressure in reservoir
R	Gas constant, 8.314[J/K/mol]
R_1	Inner radius of hollow fiber
R_2	Outer radius of hollow fiber
T	Temperature [K]
V_R	Reservoir volume [m^3]
V_T	Total volume [m^3]

1 INTRODUCTION

1.1 Motivation and Problem Description

With the global energy demand rising and instability in oil-exporting countries, the scientific community has been searching for environmentally responsible and economically viable approaches to harvest energy and convert it into forms suitable to meet societal needs (e.g., transportation fuels). Solar, wind, geothermal and hydropower energy sources are being considered as alternatives to conventional fossil fuels.[1, 2]

Solar energy holds great potential because of its ubiquitous availability. Currently, the alternative fuel industry is based largely on the photosynthetic capture of solar energy as carbohydrates in food crops, wood, switchgrass, and corn stover.[3] The carbohydrates are then recovered from the plant material, converted into sugars, and then used in fermentations to produce bioethanol, biobutanol, etc.

However, the biomass refining processes required to convert the plant material (biomass) into a fermentable sugar stream can be costly because the biomass typically needs to be harvested, pre-treated then hydrolyzed with enzymes.[4, 5] Moreover, photosynthesis is inherently inefficient; a typical crop plant has a sunlight-to-biomass efficiency of only 1%-3% of the overall solar radiation.[6] On the other hand, with advances in photovoltaic technology, commercial solar panels have reached efficiencies up to 21.0%,[7] suggesting that transportation fuels could be produced more efficiently via mature electrofuel technologies.

In the electrofuel platform, solar energy is harvested and converted into liquid fuels without the involvement of photosynthesis. In one approach, photovoltaic materials convert solar energy into electricity, which is then used to electrolyze water into H_2 and O_2. The storage, transportation, and use of H_2 as a transportation energy source are energy intensive. However, by

using engineered microbes as biocatalysts, H_2 and CO_2 can be converted into a convenient, energy-rich liquid fuel, such as isobutanol (IBT). Thus, the electrofuel platform has the potential to circumvent inefficient photosynthetic solar energy collection, as well as energy intensive biomass pre-treatment and carbohydrate hydrolysis to potentially generate higher yields.[8]

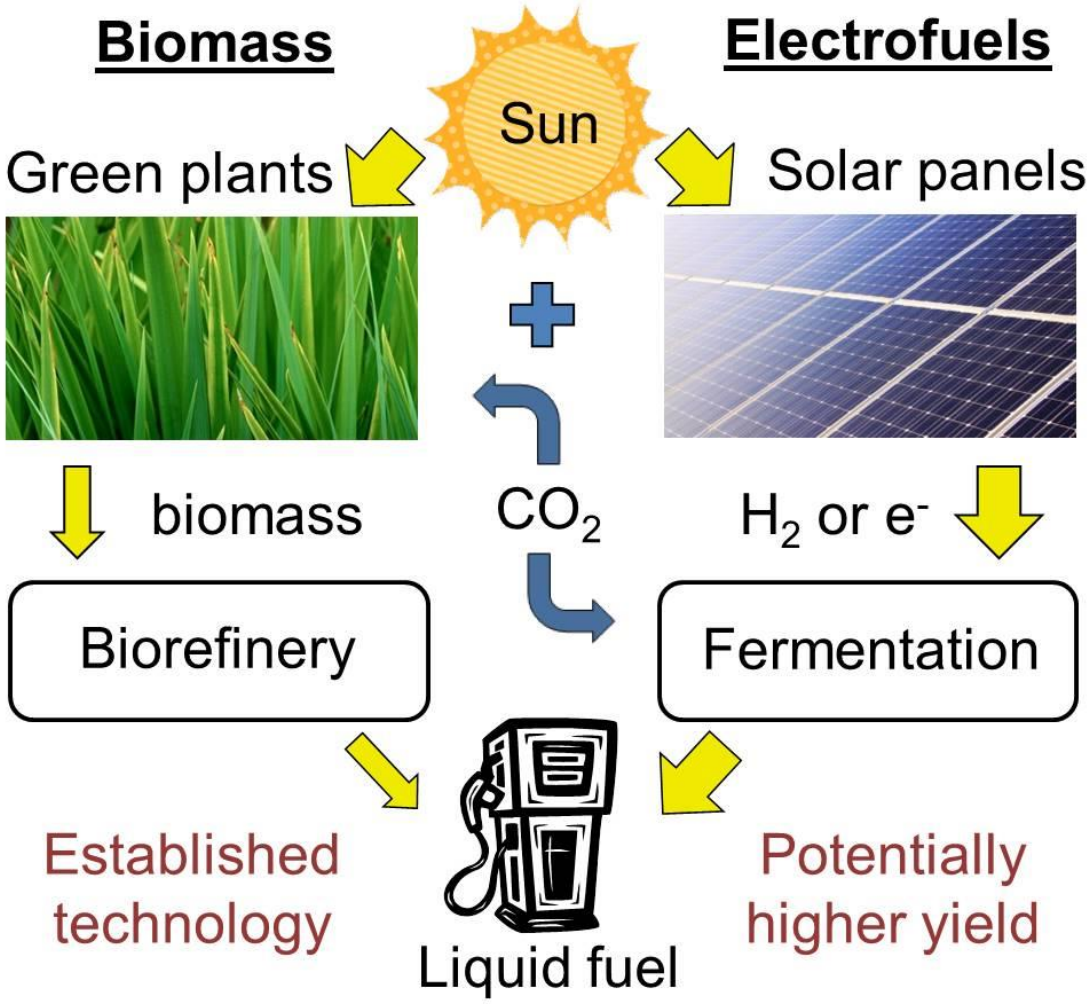

Figure 1.1 Schematic comparison between biomass-based alternative fuel platform (left) and electrofuel platform (right). For interpretation of the references to color in this and all other figures, the reader is referred to the electronic version of this dissertation.

In most cases, microbes that can utilize H_2 or CH_4 as a source of energy need an electron acceptor, such as O_2,[9, 10] sulfate[11] or nitrate[12] to receive the electrons generated when

oxidizing H_2 and CH_4. For economic reasons, O_2 is preferred in industrial processes. Conventional fermentation vessels are poorly designed for using flammable gases and O_2 as substrates for several reasons. First, the traditional method to increase the gas mass transfer rates is to increase the impeller power in stirred tanks, which reduces bubble size and increases interfacial area. However, this approach scales up unfavorably, resulting in unaffordable power requirements in commercial-scale bioreactors.[13] Second, these fermentations require many more moles of gas to be transferred per mole of product than conventional aerobic fermentations. About 9 moles of H_2 would be consumed per C-mole of IBT produced by *Ralstonia. eutropha*.[14] In contrast, only about 0.25 moles of O_2 are consumed per C-mole of product in a typical aerobic fermentation.[15] Thus, gas mass transfer, which is already rate-limiting in most aerobic fermentations, is much more challenging for gas-intensive fermentations. Third, most microbes used for the electrofuel fermentations simultaneously require both a flammable gas (CO, H_2, or CH_4) and O_2.[9, 14] Existing methods to rapidly deliver both a flammable gas and O_2 to the cells would generate potentially explosive gas mixtures. Thus there is an urgent need for a scalable bioreactor system that can cost-effectively achieve extremely high mass transfer rates without gas-phase mixing of incompatible gases.

As solar-derived H_2 is made more available by increased efficiency achieved by photovoltaic materials, a bioreactor where biosynthesis of liquid fuels can be safely carried out with high yields remain the key piece of technology that can make the Electrofuel platform feasible.

The goal of this project includes two aspects: 1) to construct a prototype bioreactor system that would allow simultaneous enhanced mass transfer of incompatible gaseous feeds to the bacterial culture without creating an explosive mixture with an integrated *in situ* product

recovery system, and 2) to develop a comprehensive mathematical model to obtain insights on the interplay between mass transfer and cellular kinetics in the system to design strategies for performance improvement and future system scale-up.

1.2 Background

1.2.1 Alternative Fuels and Strategies for Production

Alternative liquid fuels of current research interests include ethanol,[16] IBT,[17] *n*-butanol,[17] etc. IBT has advantages over ethanol, includinghigher energy content (33 MJ/kg for IBT versus 27 MJ/kg for ethanol[18]) and better compatibility with current pipeline infrastructure due to its lower tendency to cause stress corrosion cracking.[19] Moreover, they can also be converted to alkenes, which are gateway chemicals that can be hydrogenated, esterified or polymerized to synthesize a diverse group of compounds with various applications.[17]

Intensive research is being carried out to develop and improve production methods for these alternative fuels, and many of the approaches use microbes as the catalyst. These "biocatalysts" have several advantages over their inorganic counterparts:[20] (1) using metabolic engineering, the microbes could be "tailored" to utilize certain substrate(s) as the carbon or energy source; (2) microbes produce fewer by-products (higher product specificity); (3) microbial fermentations usually take place under mild conditions as opposed to some inorganic catalytic reactions; and (4) well-designed fermentation processes typically do not generate inorganic pollutants. As a result, using fermentation-based processes may reduce operating costs and minimize the impact on the environment.

Microbes can produce fuels from a variety of substrates. The most common substrates are sugars derived from biomass sources, including wood, switchgrass, corn stover, corn, etc.

However, the process of converting the biomass into sugars can be costly because the biomass typically needs to be harvested, pre-treated, and then hydrolyzed with enzymes.

On the other hand, solar-derived H_2 is predicted to be increasingly available with technical advancements in solar water splitting, [21-23] suggesting that H_2 may ultimately be an economically viable substrate for microbial fuel production.

1.2.2 Isobutanol Production by *Ralstonia eutropha*

Ralstonia eutropha is a gram-negative bacterium that can use H_2 as its energy source and CO_2 as its carbon source. This microbe has flexible metabolic pathways and therefore is able to carry out both heterotrophic growth, where the microbe uses complex organic carbon substrates (e.g., sugars), and autotrophic growth, where the microbe uses inorganic sources (e.g., CO_2 and H_2).[12] When the nitrogen source is limited, this microbe accumulates poly-β-hydroxybutyrate (PHB) in the form of intracellular storage granules, which can be harvested and used to manufacture biodegradable thermoplastics.[16] Of all the bacteria that synthesize PHB, *R. eutropha* is the most commonly used, owing to its ability to accumulate high levels of PHB (on the order of 60 g/L[24]) when grown on a simple medium.[25]

The metabolic carbon flux in *R. eutropha* can be re-routed to synthesize IBT instead of PHB. Our collaborators on this project, Dr. Anthony Sinskey's team in the Massachusetts Institute of Technology Biology Department, have removed the PHB-producing pathway in *R. eutropha* and constructed an IBT synthesis pathway based on the native pathway for valine biosynthesis from pyruvate.[26] By introducing a heterologous ketoacid decarboxylase, the valine precursor 2-ketoisovalerate is converted to isobutyraldehyde and then reduced by an alcohol dehydrogenase to IBT.[27]

Even though the technology to produce IBT from sugars is close to commercialization,[28] the only published work on IBT production from CO_2 is in photosynthetic cyanobacterium *Synechococcus elongatus*, where the resulting IBT titer was less than 1 g/L.[27] The ability of wild-type *R. eutropha* to accumulate PHB at a level of 60 g/L from autotrophic feeds[24] suggests that engineered *R. eutropha* could achieve a high level of IBT productivity.

1.2.3 Fermentation of Gases with Low Aqueous Solubilities

Wild type *R. eutropha* is able to accumulate PHB using CO_2 as the carbon source and H_2 as the energy source.[10, 29-32] With the PHB synthesis pathway genetically deleted, and IBT-producing pathway inserted, the engineered *R. eutropha* strains are able to produce IBT both heterotrophically[33] and autotrophically, as demonstrated in Chapter 2.

Developing a fermentation process in which the carbon and energy sources are all gases presents significant engineering challenges. In fermentations with sparingly soluble gases such as H_2 or CO, the rate-limiting step is typically gas-to-liquid mass transfer.[34-36] Besides using high-shear impellers and increasing impeller rates,[34, 37] engineering approaches commonly used to enhance gas-liquid mass transfer in fermentations include 1) gas sparging through fritted glass[38, 39] with intensive agitation; 2) gas delivery in microbubbles;[40] and 3) use of a continuous gas phase, with counter flow of gas and liquid through a packed column containing immobilized cells.[38, 41]

The incompatible nature of H_2 and O_2 gases presents other engineering challenges. H_2 has a wide explosive range (4%-75% in air), and therefore mixing H_2 with O_2 at virtually any ratio raises serious safety concerns. Little guidance is provided in the literature on bioreactor designs that simultaneously provide rapid mass transfer of incompatible gases while preventing formation of explosive gas mixtures. In one published patent application, surfactants were used

to maintain an energy-rich gas (methane) and oxygen as discrete bubbles for fermentation applications. However, this approach would add significant costs to the operation and downstream product purification. The primary goal of this project is to design, assemble, and operate a bioreactor that provides sufficient oxygen and hydrogen mass transfer to the cells without creating a potentially explosive gas mixture.

1.3 Organization of This Dissertation

1.3.1 Continuous Isobutanol Production in A Bioreactor for Incompatible Gases (BIG)

Chapter 2 introduces the design concept of a Bioreactor for Incompatible Gases (BIG), describes the design and fabrication of a prototype BIG system, and presents results documenting the first continuous, autotrophic IBT production. This part of the project was carried out in collaboration with Dr. Soumen Maiti (a postdoctoral researcher in the Department of Chemical Engineering and Materials Science). Each of the collaborators made equal contributions to the work, which demonstrated the system's ability to produce IBT both heterotrophically and autotrophically, and identified the key factors affecting the BIG's IBT productivity. The *R. eutropha* strains were provided by Dr. Anthony Sinskey at Massachusetts Institute of Technology.

1.3.2 Mass Transfer in a Bioreactor for Incompatible Gases (BIG)

Chapter 3 describes efforts to measure the mass transfer rates of O_2, CO_2 and IBT in hollow fiber membranes. Experimental methods were developed for each solute. Three approaches for data analysis were applied, including two numerical derivations and simulations in COMSOL Multiphysics®.

1.3.3 Simulation of Isobutanol Production in a Bioreactor for Incompatible Gases (BIG)

Chapter 4 describes a comprehensive mathematical model of the BIG system that takes into account multiphase, multispecies gas mass transfer and includes a structured cell kinetic model. The model was solved numerically using COMSOL Multiphysics® using various parameters to obtain insights on the operation conditions' impact on the systems performance.

1.4 Acknowledgments

Funding for this research was provided by the Department of Energy ARPA-E Electrofuels program subaward No. 5710002852.

2 CONTINUOUS ISOBUTANOL PRODUCTION IN A BIOREACTOR FOR INCOMPATIBLE GASES (BIG)

2.1 Introduction

Electrofuels are carbon-neutral, renewable transportation fuels produced via non-photosynthetic CO_2 fixation.[42, 43] With the advancement in photovoltaic technologies, solar-derived H_2 is expected to become more available for use as electron donor to reduce CO_2 and store energy in C-H bonds within multi-carbon organic compounds, such as isobutanol (IBT). IBT offers advantages over ethanol as a liquid fuel, including a lower vapor pressure, lower hygroscopicity and higher energy density. It can be blended at any ratio with gasoline and used as automotive fuel with existing infrastructure and engines.[44] Moreover, IBT can also be converted to alkenes, gateway chemicals that can be hydrogenated, esterified or polymerized to synthesize a diverse group of compounds with various applications.[17]

Most biofuel production strategies utilize heterotrophic carbon sources, such as sugars derived from biomass, such as wood, switchgrass, and corn stover.[3] However, the biomass refining to obtain sugars can be costly because the biomass needs to be harvested, pre-treated then hydrolyzed with enzymes.[4, 5] Moreover, photosynthesis inherently has a lower solar energy yield than photovoltaics, suggesting that transportation fuels could be produced more cheaply via mature electrofuel technologies than via a photosynthetic platform. Photosynthesis of a typical crop plant has a sunlight-to-biomass efficiency of only 1%-3% of the overall solar radiation,[6] as opposed to 20.1%, the highest efficiency afforded by a commercial solar panel.[7] Also, carbon-neutral electrofuels would not raise atmospheric CO_2 levels as do fossil fuels.

Ralstonia eutropha, also known as *Alcaligenes eutropha*, *Wausteria eutropha* or *Cupriavidus necator*, is a facultatively autotrophic Gram-negative bacterium that has been used

commercially to produce poly-β-hydroxybutyric acid (PHB), a biodegradable polymer,[25, 45, 46] with a maximum titer of 60 g/L.[24] Nitrogen limitation is known to promote PHB accumulation in the wild type[30] and the same regulation was used to trigger IBT production[33]. A native valine biosynthetic pathway in the wild type *R. eutropha* was engineered by Lu, Brigham [33] to produce IBT after the PHB-producing pathway was removed. The engineered strain retained the wild type strain's ability to utilize both heterotrophic and autotrophic carbon sources, with carbon flux to IBT production being stimulated under nitrogen limitation.

Construction of a bioreactor system for autotrophic production of IBT poses a unique set of engineering challenges. First, these fermentations are expected to be highly mass-transfer limited. Although the overall stoichiometry for autotrophic IBT production will depend on a number of factors, including how much ATP is consumed for cell maintenance, an approximate stoichiometry based on known reaction pathways in *R. eutropha* (Equation 2.1)[10] indicates that 9 moles of H_2 would be consumed per C-mole of CO_2 reduced to IBT. In contrast, only about 0.25 moles of O_2 are consumed per C-mole of glucose consumed in a typical aerobic fermentation.[15] Moreover, both H_2 and O_2 have low aqueous solubilities, resulting in low driving force for mass transfer. The combination of a higher demand for gas mass transport and a small driving force indicates that the well-known challenges associated with achieving sufficient gas mass transfer rates in aerobic fermentations would likely be at least one order of magnitude more severe for fermentations that produce biofuels from H_2 and CO_2. Since the stoichiometric coefficients represent the demand on the gas substrates, and the aqueous solubility and diffusivity indicate the difference in each substrate's mass transfer characterisitics, the ratio of gas substrates' stoichiometric coefficients versus the product of their aqueous solubilities and diffusivities can be used as a qualitative gauge of their individual mass transfer challenge, as

summarized in Table 2.1. Even though H_2 has a higher diffusivity in water, the mass transfer challenge it poses is still more than twice of O_2, making H_2 mass transfer highly likely to be a rate-limiting step. Second, the need to simultaneously deliver H_2 and O_2 creates safety issues because these gases are incompatible, forming a flammable mixture over the range 4 to 94% H_2. Third, like most alcohols, IBT is inhibitory to the bacterial cells, making its *in situ* removal desirable for continuous bioreactor operations.

$$4CO_2 + 12O_2 + 36H_2 \rightarrow C_4H_{10}O + 31H_2O \qquad 2.1$$

Table 2.1 Comparison of mass transfer challenges posed by the three gas substrates.

Gas	**Amount required (mole/mole of isobutanol)**	**Solubility in water (1 atm, 25°C) (mole gas/kg water)[47]**	**Diffusivity in water ($\times 10^{-5}$ cm^2/s)**	**Mass transfer resistance (stoichiometric coefficient/(solubility ·diffusivity)) (kg·s/(mole ·cm2))**
H_2	36	7.90×10^{-4}	4.50[48]	1.01×10^{9}
O_2	12	1.32×10^{-3}	2.10[49]	4.33×10^{8}
CO_2	4	3.45×10^{-2}	1.92[49]	6.04×10^{6}

Existing bioreactor systems and strategies are not well suited to address this unique set of engineering challenges. The strategy of simply mixing the gases at a ratio out of explosive limit results in severe O_2 limitations.[45] In addition, error in controlling the gas mixture or fluctuations in cell metabolic activity could allow formation of explosive gas mixtures. A second approach is to use a potentially explosive gas mixture, but contain it within an explosion-proof reactor designed to withstand the pressure increase that would result if the gas phase ignited.[50] A disadvantage of this approach is that fermenters able to withstand extremely high internal pressures are expensive to fabricate and scale up. Another strategy used excessive gas in the

form of emulsions stabilized with surfactants, which would add significant costs to the operation and downstream product purification.

This chapter presents a novel Bioreactor for Incompatible Gases (BIG) concept that facilitates simultaneous and rapid mass transfer of two sparingly soluble and incompatible gases while preventing formation of explosive gas mixtures. A prototype BIG system was developed that uses Opto-22 control system to monitor and regulate the feeding gas flow rates in the system to ensure safe operation and minimize wasted gas. The prototype BIG system was used with a recombinant strain of *R. eutropha*, and it is the first to continuously produce IBT autotrophically on H_2, CO_2 and O_2.

2.2 Materials and Methods

2.2.1 Microorganisms and Media

Methods used to develop the *R. eutropha* strains Re2061 and Re2425/pJL26 used in this study have been reported previously.[33] Briefly, Re2061 is a derivative of the wild type strain with the PHB-producing pathway removed, and Re2425/pJL26 uses the overexpression of plasmid-borne, native branched-chain amino acid biosynthesis genes and the overexpression of heterologous ketoisovalerate decarboxylase gene to channel excess carbon from the PHB production to biosynthesis of IBT. Re2061 was used in experiments on immobilization techniques, while Re2425/pJL26 was used in all the IBT-producing and -consumption experiments presented in this work.

The strains were cultivated at 30°C in either rich media consisting of 2.75 % (w/v) dextrose-free tryptic soy broth (TSB) (Becton-Dickinson, Sparks, MD, USA) or minimum media that contained per liter: 4.0 g NaH_2PO_4, 4.6 g Na_2HPO_4, 0.45 g K_2SO_4, 0.39 g $MgSO_4$, 0.062 g

$CaCl_2$, and 1 mL/L of a trace metal solution. The trace salt solution contained 15 g/L $FeSO_4 \cdot 7H_2O$, 2.4 g/L $MnSO_4 \cdot H_2O$, 2.4 g/L $ZnSO_4 \cdot 7H_2O$, 0.48 g/L $CuSO_4 \cdot 5H_2O$ and 0.1 M HCl. For heterotrophic growth, 2% (w/v) fructose was added as carbon and energy source. For autotrophic growth, H_2, CO_2 and O_2 gases were provided from compressed-gas cylinders. Two initial ammonium chloride concentrations were used, 0.1% (w/v) was used to promote growth while 0.01% (w/v) was used to facilitate product formation. All media used for Re2061 contained a final gentamicin concentration of 10 μg/mL, and additionally, all media used for Re2425/pJL26 also contained 200 μg/mL kanamycin.

The stock culture was grown on TSB agar plates, from which a single colony was picked and cultured in 2-mL TSB medium. After overnight incubation, the 2-mL TSB culture was then used to inoculate 100 mL minimal growth medium in a flask, which was shaken in an incubator until it reached exponential growth phase before it was used as inoculum for three 1-L minimal medium cultures in Erlenmeyer flasks.

2.2.2 Bioreactor for Incompatible Gases (BIG)

The proposed hollow-fiber bioreactor (Figure 2.1) has the biocatalyst immobilized on, or entrapped within, the walls of hollow fiber membranes that separate the bioreactor housing into a lumen side (inside the hollow fibers) and a shell side (outside the hollow fibers).

H_2 and O_2 are provided from opposite sides of the membrane with H_2 in gas phase and O_2 dissolved in the liquid medium. If necessary, the H_2 mass transfer rate can be enhanced by increasing the pressure, thus increasing the solubility (C^*) and raising the driving force for gas dissolution, as suggested by Equation 2.2, where N is the total flux of gas-liquid mass transfer,

k_L is the mass transfer coefficient, a is the interfacial area, and C is the aqueous concentration of dissolved gas.

$$N_g = k_L a(C^* - C) \qquad 2.2$$

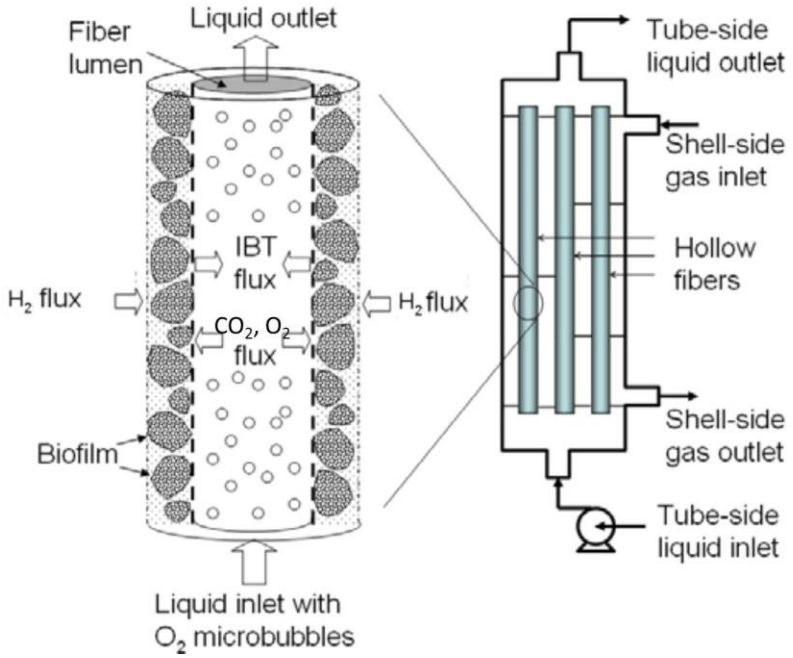

Figure 2.1 Design concept for a bioreactor for incompatible gases (BIG) for autotrophic IBT production.

On the other hand, the mass transfer of O_2 can be enhanced by using microbubble dispersion. Microbubbles, which have been used to enhance gas transportation in fermentations,[40, 51-53] can improve the mass transfer rate by orders of magnitudes. As demonstrated in Equation 2.3, the volumetric gas mass transfer rate is dependent on the specific interfacial area and the concentration gradient. The specific interfacial area of spherical bubbles (a) is inversely correlated with the bubble diameter, as is the gradient of gas concentration around the bubbles at steady state.[40] Therefore, a 100-fold decrease in bubble size could potentially enhance the mass transfer rate by ten thousand fold.

$$N_g = D \cdot a \cdot \frac{dC}{dr} \quad (2.3)$$

Moreover, the surface tension between aqueous and gaseous phases also results in a difference in pressure inside and outside a bubble, denoted Laplace pressure. Laplace pressure is proportional to the surface tension σ and inversely proportional to the bubble radius r (Equation 2.4); therefore the very small r values of microbubbles make Laplace pressure effects potentially significant. As O_2 dissolves in the water, the bubble size decreases, further elevating the Laplace pressure and thus further aiding the O_2 dissolution process.

$$\Delta P = \frac{2\sigma}{r} \quad (2.4)$$

By feeding H_2 and O_2 from opposite sides of the membrane, the bioreactor design allows bacterial culture sufficient access to both gases while keeping them separate. Significant mixing of H_2 and O_2 due to transport across the membrane is unlikely to happen for these reasons: 1) The pores of the hollow fiber membrane are filled with bacterial cells in aqueous environment, and both of the gases are sparsely soluble in water, limiting the flux between the lumen and shell side of the membrane; 2) The bacteria will consume most of the gas that diffuses into the membrane; 3) The selected membrane will have a pore size that won't allow O_2 microbubbles to pass.

Hollow fiber membrane reactors have been extensively used in industrial scale wastewater treatments. The reactor designs are modularized and highly scalable, reaching a processing capacity up to 3×10^7 gal/day.[54, 55]

2.2.3 Hollow Fiber Membrane Selection

To select a suitable hollow fiber membrane for this application, the following criteria were used: 1) the material should be hydrophilic so that the membrane can provide a humid

environment for the bacteria; 2) Based on scanning electron microscopy (SEM, JEOL JSM-6610LV) image (Figure 2.2), the rod-shape *R. eutropha* cells have a typical diameter of 0.5 μm and an average length of about 1.5 μm. To allow the cells to be embedded at a high density, the membrane should have asymmetric pore size distribution with pores significantly larger than the cells on one side and smaller pores (submicron size) on the other side so that the bacterial cells can be retained in the larger pores; 3) for analytical purposes, the membrane material should be chemically resistant to the reagents used to extract protein from immobilized cells and should not interfere with protein assays.

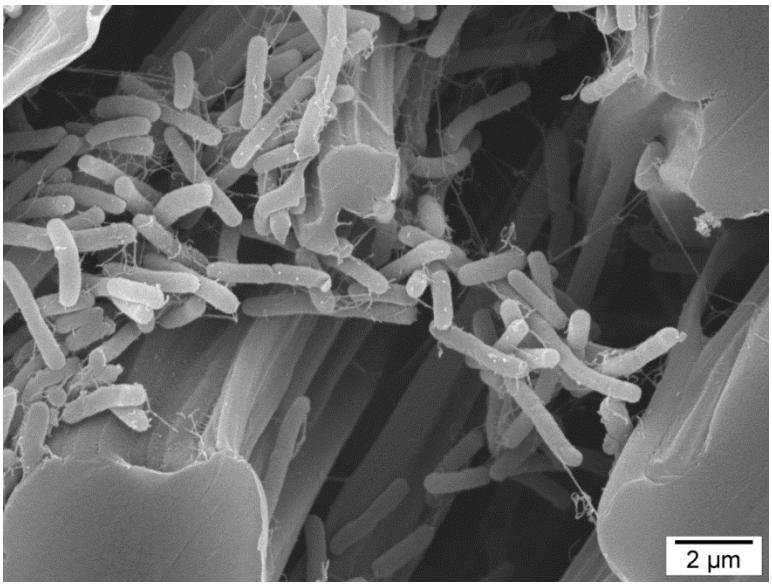

Figure 2.2 SEM image of immobilized *R. eutropha* cells (Re2061).

Initially, a number of hollow fiber membranes were considered, including polysulfone (CLF2E110, GE Healthcare, Pittsburg, PA), polypropylene, polyvinylidene fluoride (PVDF) and mixed cellulose ester hollow fiber membranes (Spectrum Laboratories, Inc., Rancho Dominguez, CA). However, preliminary SEM examinations found that the pore sizes of all the membranes are too small for cells to be embedded into the pores (Figure 2.3-Figure 2.6).

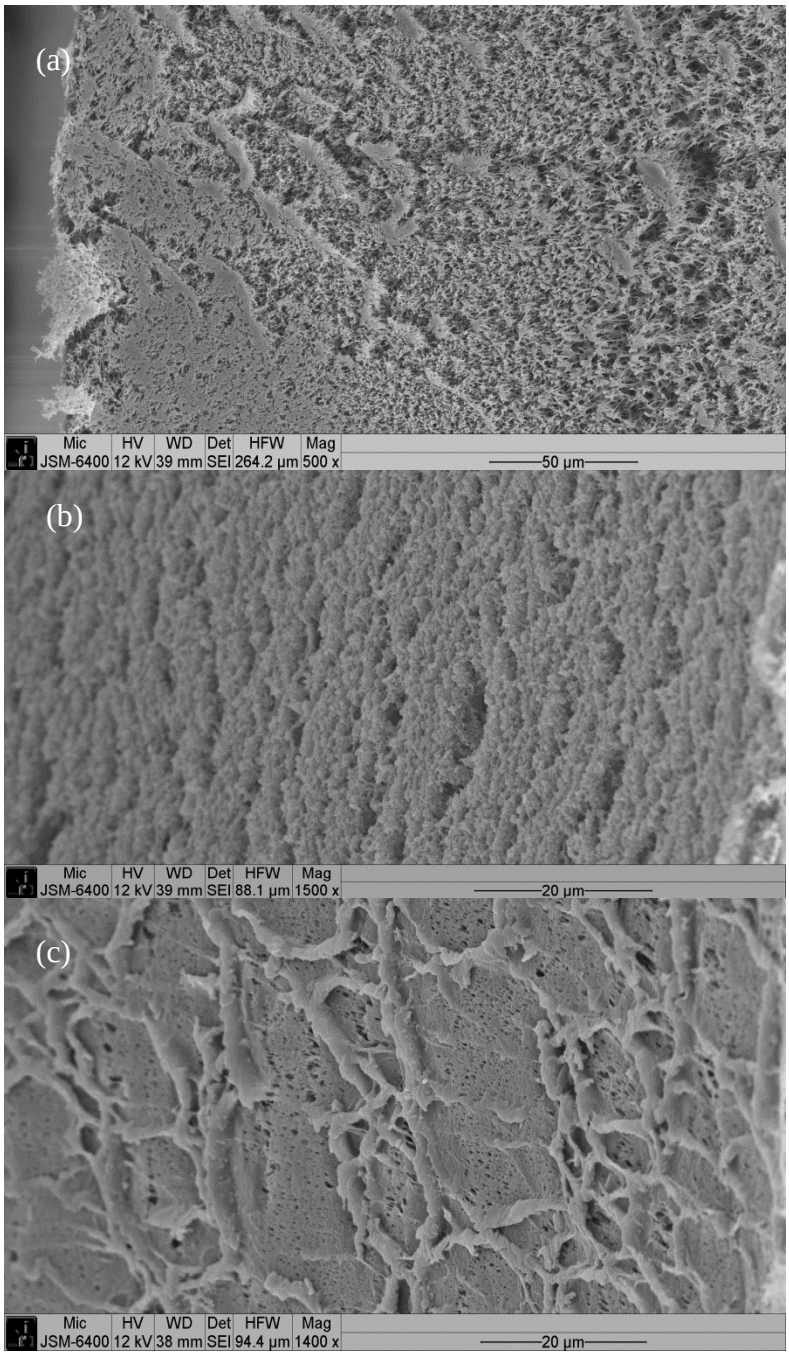

Figure 2.3 SEM images of (a) cross section, (b) inner surface and (c) outer surface of polysulfone hollow fiber membrane. This type of polysulfone hollow fiber membrane showed relatively uniform size distribution on the scale of 1 µm and is therefore not suitable for cell immobilization by embedding.

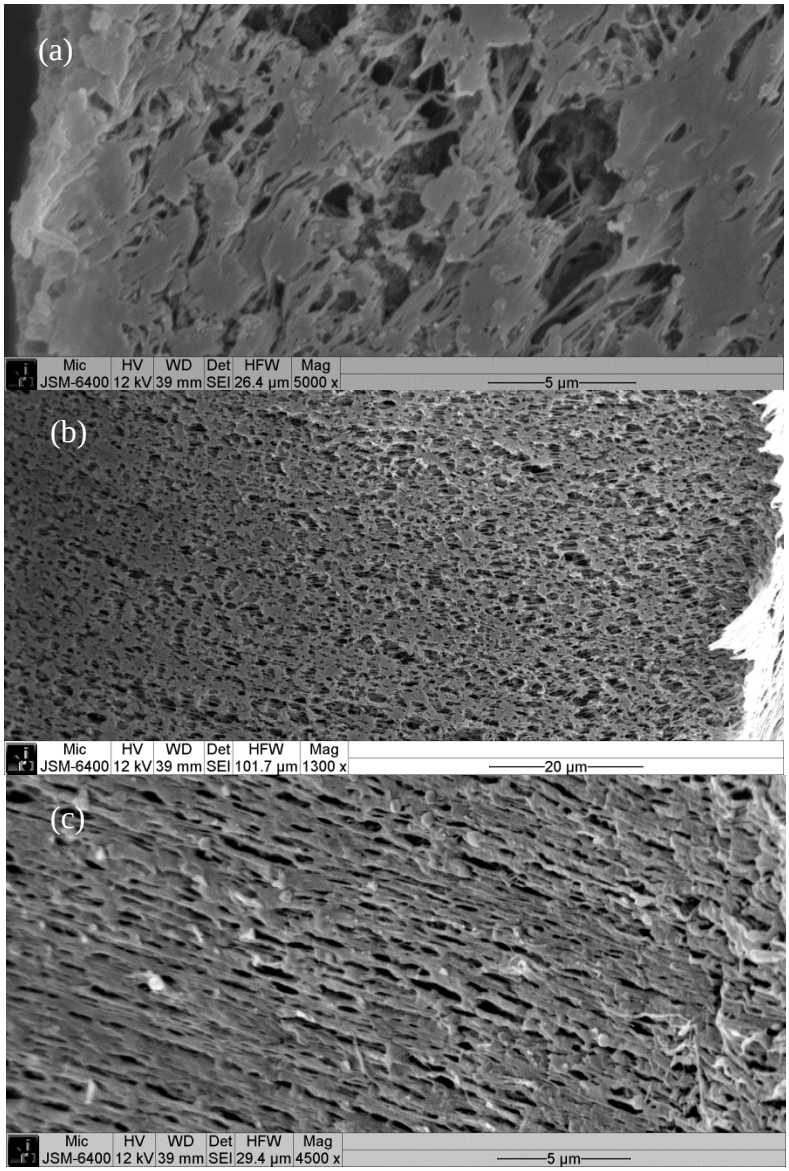

Figure 2.4 SEM images of (a) cross section, (b) inner surface and (c) outer surface of polypropylene hollow fiber membrane. The membrane showed pore size in the 1-5 µm range and therefore is not optimal for cell immobilization by embedding.

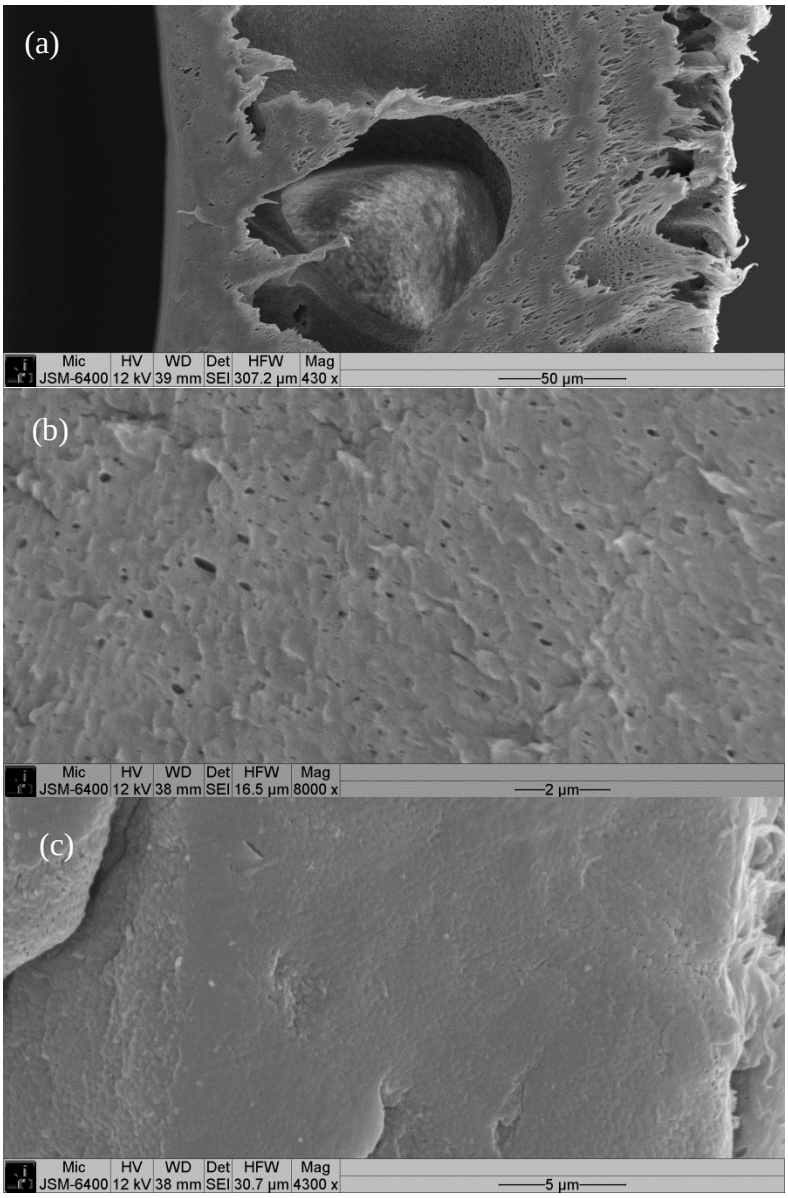

Figure 2.5 SEM images of (a) cross section, (b) inner surface and (c) outer surface of polyvinylidene fluoride hollow fiber membrane. Even though the membrane has large internal "pockets" large enough to accommodate cells, the pores on its inner and outer surface exhibit submicron sizes, making it unsuitable as immobilization matrix.

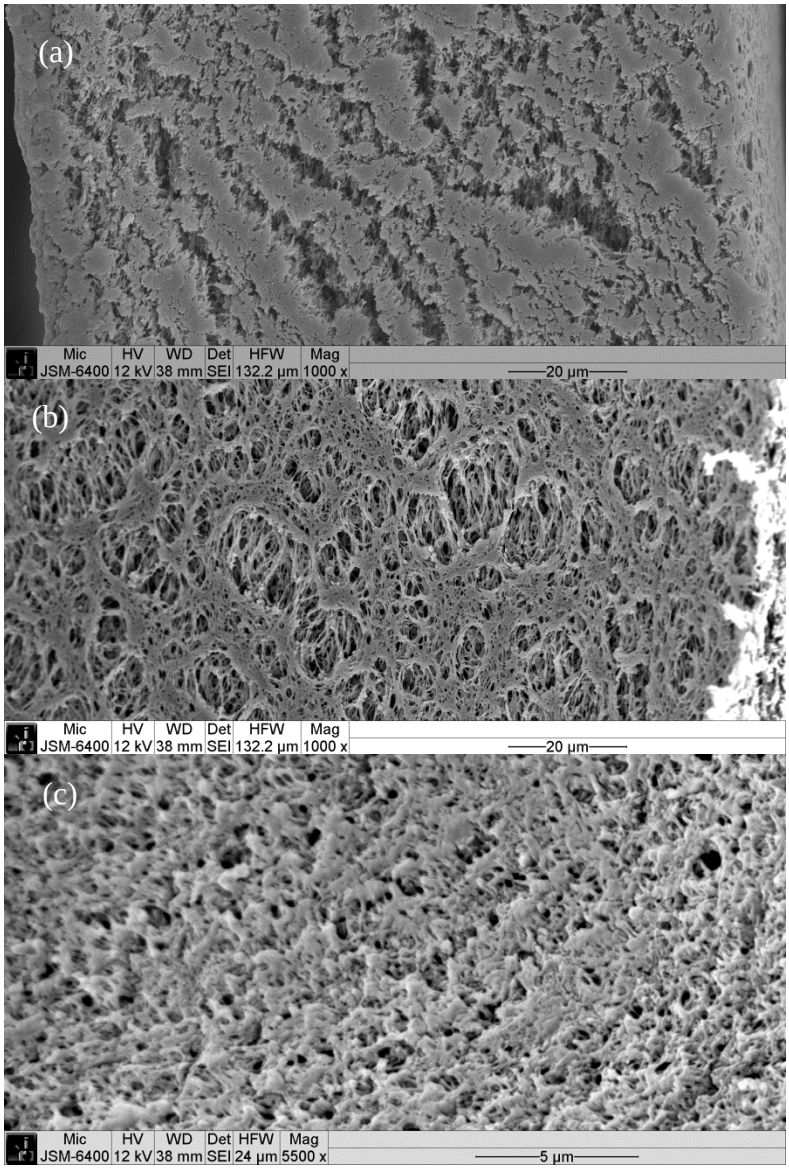

Figure 2.6 SEM images of (a) cross section, (b) inner surface and (c) outer surface of mixed cellulose ester hollow fiber membrane. The pore sizes exhibited are also non-ideal for cell immobilization.

Ultrafiltration membranes fulfill the requirement on pore size distribution since they typically have anisotropic pore size distributions with a skin layer with the designated nominal pore size and a "spongy layer" with macroporous structure to provide extra mechanical strength without adding resistance to the permeate flow. XM-50 hollow fiber membrane has been successfully used for whole cell immobilization, and the material, a polyacrylonitrile/polyvinylchloride copolymer, is reasonably hydrophilic. Therefore, an XM-50 ultrafiltration hollow fiber cartridge was chosen as the reactor (hereafter noted as HFR, HF, 1018-1.0-45-XM50, Koch Membrane System, Wilmington, MA). The membrane has a skin layer on the lumen side with a nominal pore size of 50 kDa, while the shell-side pore size is on the 10-100 μm scale and large enough for the cells to enter and become entrapped in the fiber wall.

2.2.4 Cell Immobilization and Hollow Fiber Membrane Cleaning

Prior to experiments, the hollow fiber cartridge was sanitized by incubating the HFR lumen, fiber wall, and shell space with 500 ppm aqueous sodium hypochlorite (NaClO) solution for at least 2 h. Afterwards, the HFR was thoroughly rinsed with sterile water. The experiments on immobilization techniques were carried out with strain Re2061.

The cells were grown on fructose-based minimal medium until they reached exponential growth phase and then used to inoculate the HFR. For incubation immobilization method, 1-cm fiber segments were incubated in the exponentially growing culture at 30˚C for 48 h (Figure 2.7 left).

For filtration immobilization, cells from 3-L exponentially growing culture were harvested, rinsed 3 times with 0.1 M phosphate buffer saline (PBS) at pH 7.4 to prevent carry-over of fructose and metabolic intermediates from the spent heterotrophic medium, and re-

suspended in 200-250 mL fructose-free minimal media. The concentrated *R. eutropha* culture was placed in a 300 mL sample cylinder (AA0359 304L-HDF4-300CC, Swagelok, Solon, OH) connected to the HFR shell side, and the cells were forced into the pores of the membrane spongy layer from the lumen by applying pressure on the shell side using compressed air (Figure 2.7 right). Because pores on the inner membrane skin were too small to allow cell passage, the cells were filter-immobilized within the large pores of the membrane spongy layer.

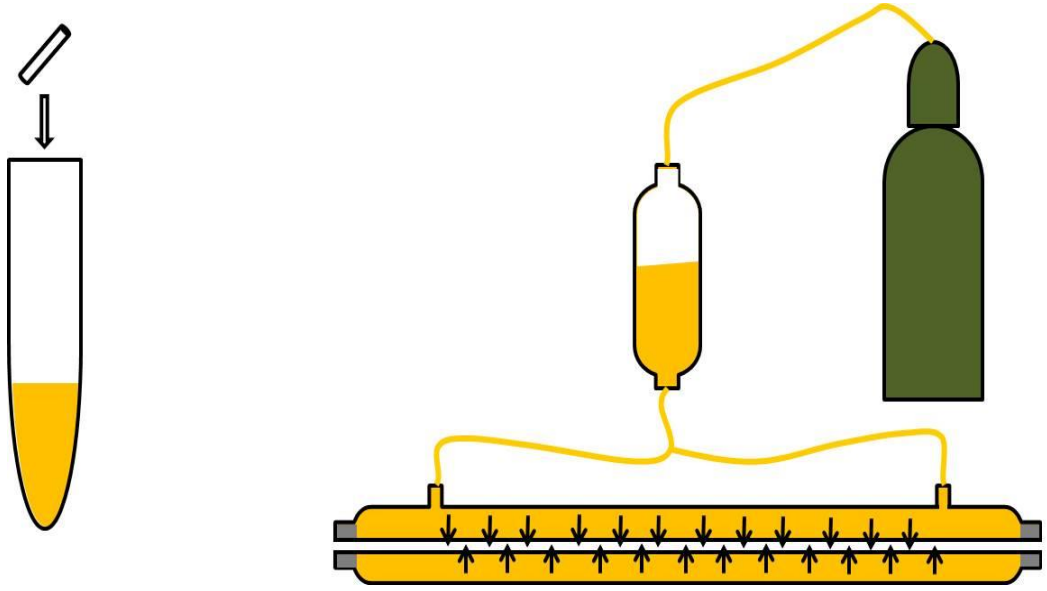

Figure 2.7 Illustration for cell immobilization/membrane inoculation. LEFT: inoculation by incubation; RIGHT: inoculation by filtration.

After experiments, the hollow fibers were rinsed repeatedly by forcing sterile water from lumen to shell in order to flush out embedded cells. The water rinsate (rinsate 1) was collected. To further remove cell mass from the hollow fibers, the lumen, fiber wall, and shell side were filled with 1M NaOH aqueous solution and incubated at room temperature for 6~8 h to lyse the cells and extract the protein.[56] After the incubation, the protein extract was collected, and the membrane was rinsed with copious de-ionized water until the rinsate reached neutral pH. All the alkaline rinsate (rinsate 2) was collected for protein quantitation.

2.2.5 Measurement of Biomass, Ammonium and IBT Concentration

For planktonic cultures, the cell density was measured using an HP 8452 diode array spectrophotometer (Hewlett-Packard, Palo Alto, CA).

For experiments with cell immobilization techniques, 1-cm hollow fiber segments were collected and incubated in 1 M NaOH at 125˚C for 15 min to lyse the cells before the protein contents were quantitated with fluorescamine assay.

For experiments with immobilized cells in hollow fiber modules, the final cell mass was measured by totaling the cell mass in the rinsates. Cell mass in rinsate 1 was quantified by its optical density at 600 nm (OD600) before the cells were collected by centrifugation and lysed using the same alkaline incubation as for the hollow fiber membrane. The protein content in this extract was used as a reference to measure the cell mass in rinsate 2 (Equation 22.5).

$$M_2 = \frac{C_2 \times V_2'}{C_1 \times V_1'} \times (x_1 \times V_1) \qquad 2.5$$

M_2 is the total cell mass in rinsate 2, $x_1$and V_1 are the cell density and volume of rinsate 1, C_1 and $V_1'$are the protein concentration and volume of the protein extract from rinsate 1, and C_2 and V_2' are the protein concentration and volume of the rinsate 2 protein extract.

Immobilized cell mass was estimated by total protein content as quantitated using fluorescamine assay. Fluorescamine reacts with primary amines in proteins and forms highly fluorescent moieties. The intensity of the fluorescent response correlates linearly with protein concentration at lower protein concentrations (0-500 µg/mL). The assay procedure has been described by Held. Briefly, 50 µl aliquots of 10.8 mM (3mg/ml) fluorescamine (F9015, Sigma-Aldrich Corporation, Missouri, MO) dissolved in acetone were added to 150 µL of diluted samples and bovine serum albumin (BSA, 05470, Sigma-Aldrich, Missouri, MO) standards in a

96-well plate (82050-728, Greiner Bio-One, Monroe, NC) and mixed immediately before the fluorescence responses were determined using a 400 nm, 30 nm bandwidth, excitation filter and a 460 nm, 40 nm bandwidth emission filter. The protein concentrations of the samples were determined using the BSA standard curve.

The concentration of NH_4^+ was measured using an assay kit (AA0100, Sigma-Aldrich, St. Louis, MO). IBT was measured using a Bruker® GC-450 gas chromatograph (Bruker Corporation, Billerica, MA) outfitted with a Varian® CP7416 column and an flame ionization detector.

2.2.6 Operation of Bioreactor for Incompatible Gases (BIG)

The components used in the BIG system included two ENMET GSM-60 gas sensors (ENMET Corporation, Ann Arbor, MI), a Sartorius BIOSTAT® Bplus Fermenter with a 1-L vessel (Sartorius Stedim Biotech, S.A., Göttingen, Germany), an Opto22 SNAP-PAC-R1 programmable automation controller (Opto22, Temecula, CA), MasterFlex Pumps (Model 7523-00 and 77200-12, Cole-Parmer, Vernon Hills, IL), a hollow fiber reactor (HF, 1018-1.0-45-XM50, membrane area 1 ft^2, Koch Membrane System, Wilmington, MA), Omega FMA6500 digital mass flow controllers (Omega Engineering, Inc., Stamford, CT), and solenoid valves (Clark-Cooper Division, Magnatrol Valve Corporation, Cinnaminson, NJ).

2.2.6.1 Heterotrophic Operation with Immobilized Cells

Heterotrophic operations were carried out in the first stage of some experiments to rapidly increase the immobilized cell density and to verify the ability of the immobilized cells to heterotrophically produce IBT. The system was set up as illustrated in Figure 2.8, with a flow-through configuration on the shell side and 0.4 L fructose-based minimal medium circulated in

the lumen. The pressure at the shell side was maintained by a 1-psig check valve at the vent. Air was supplied through a Millex HA 0.45 μm filter (EMD Millipore, Billerica, MA) to the shell side at 5 psig. No gas was fed to the reservoir. The IBT in the shell effluent gas was recovered using a Graham style condenser (Z531405, Sigma-Aldrich, Milwaukee, WI) with 0˚C ethanol as coolant. Samples were collected from the reservoir for measurement of fructose, IBT and NH_4Cl.

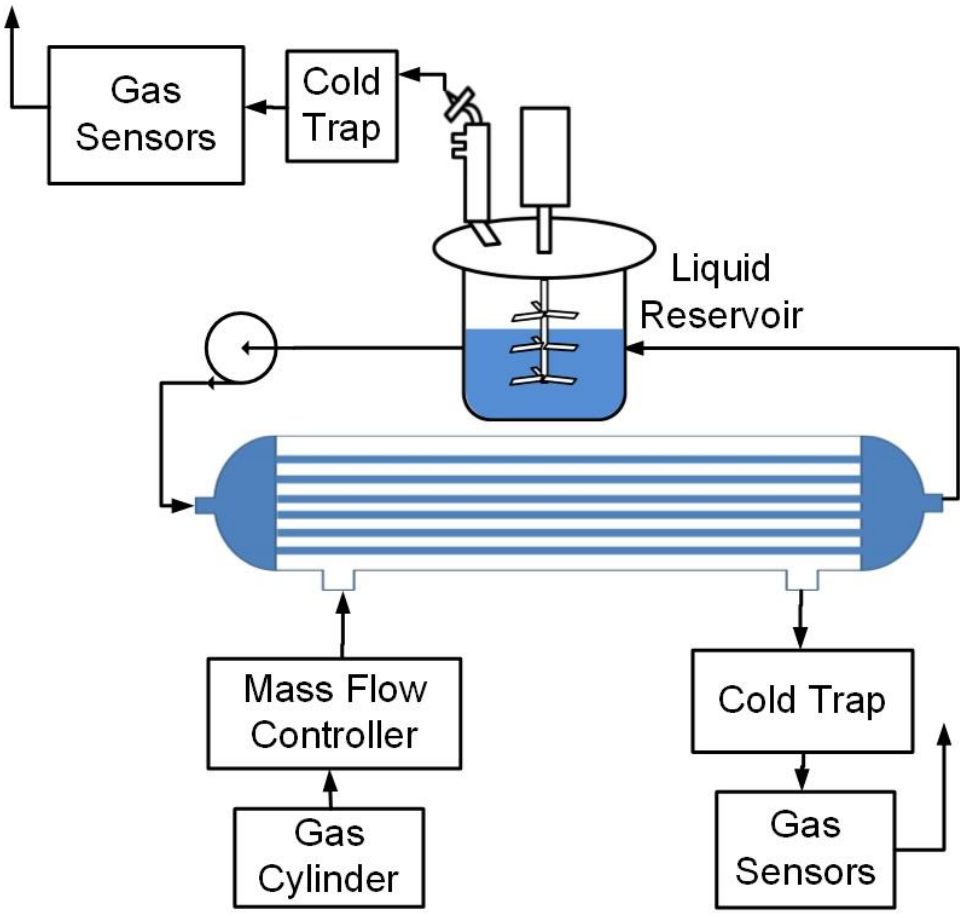

Figure 2.8 Hetetrophic operation setup with flow through configuration at the shell side.

2.2.6.2 Autotrophic Operation with Immobilized Cells

The BIG system was modified for autotrophic operations as depicted in Figure 2.9. Instead of air, H_2 and CO_2 were fed to the shell at 0.1 L/min and 0.02 L/min respectively. A peristaltic pump recirculates 0.4 L fructose-free minimal medium from the reservoir through the lumen. A flow-through configuration was used on the shell side, with the exiting gas sent to an ENMET sensor (GSM-60, ENMET Corporation, Ann Arbor, MI) to monitor O_2 concentration. The pressure at the shell side was maintained by using a 1-psig check valve at the vent.

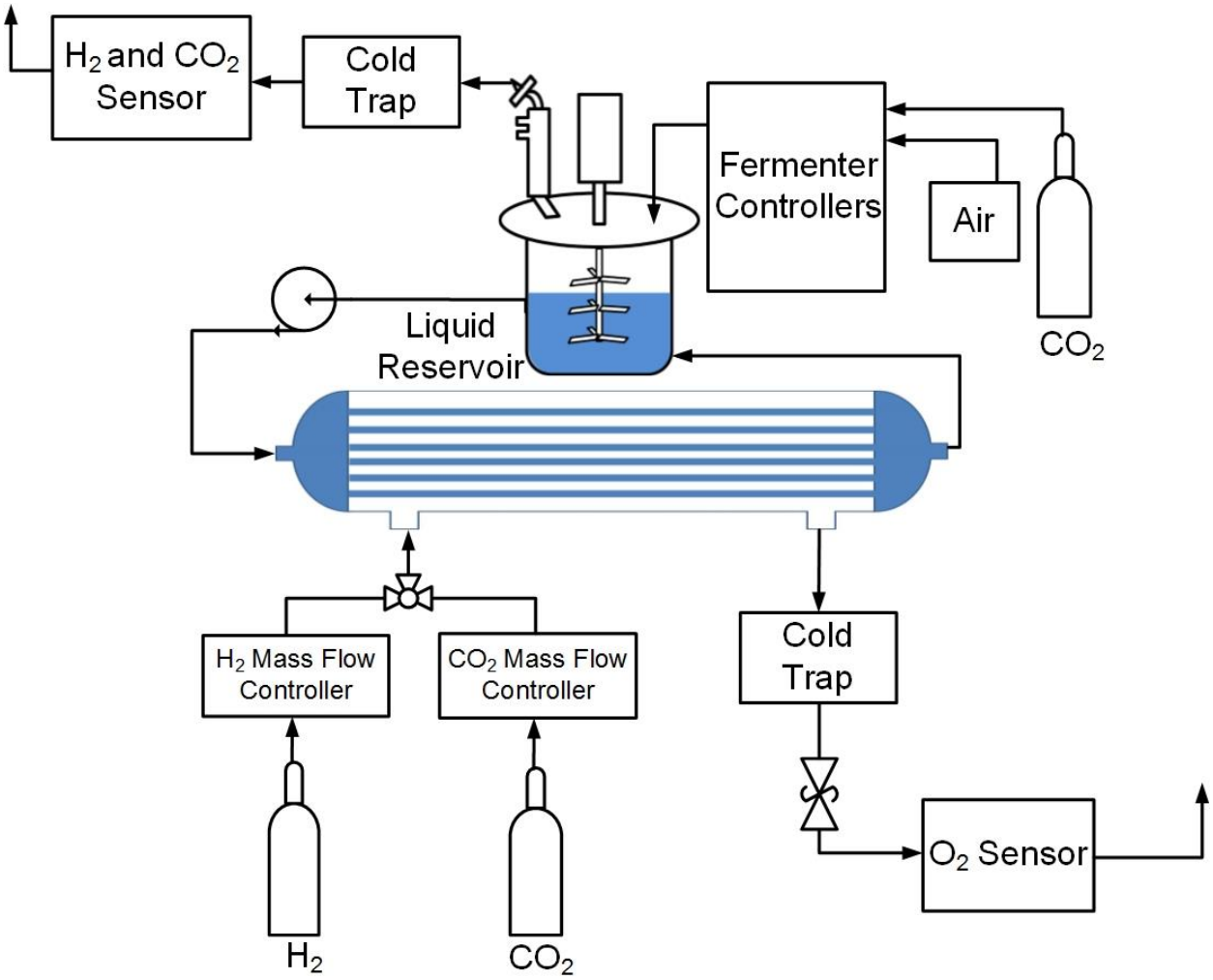

Figure 2.9 Experimental setup for autotrophic operation flow-through configuration at the shell side.

A mixture of air and CO_2 was fed to the medium reservoir in a 9:1 ratio. The gas flow rate into the reservoir was regulated by the fermentor control tower to maintain dissolved O_2 (DO) level at 80% air saturation. To minimize IBT loss to gas stripping, a cold trap was attached to the reservoir exhaust. A second ENMET gas sensor was installed to monitor the O_2, CO_2 and H_2 concentrations in the exhaust gas from the reservoir vent. Liquid samples were collected from the reservoir for IBT and NH_4^+ analysis.

2.2.6.3 Autotrophic Operation with Planktonic Cells

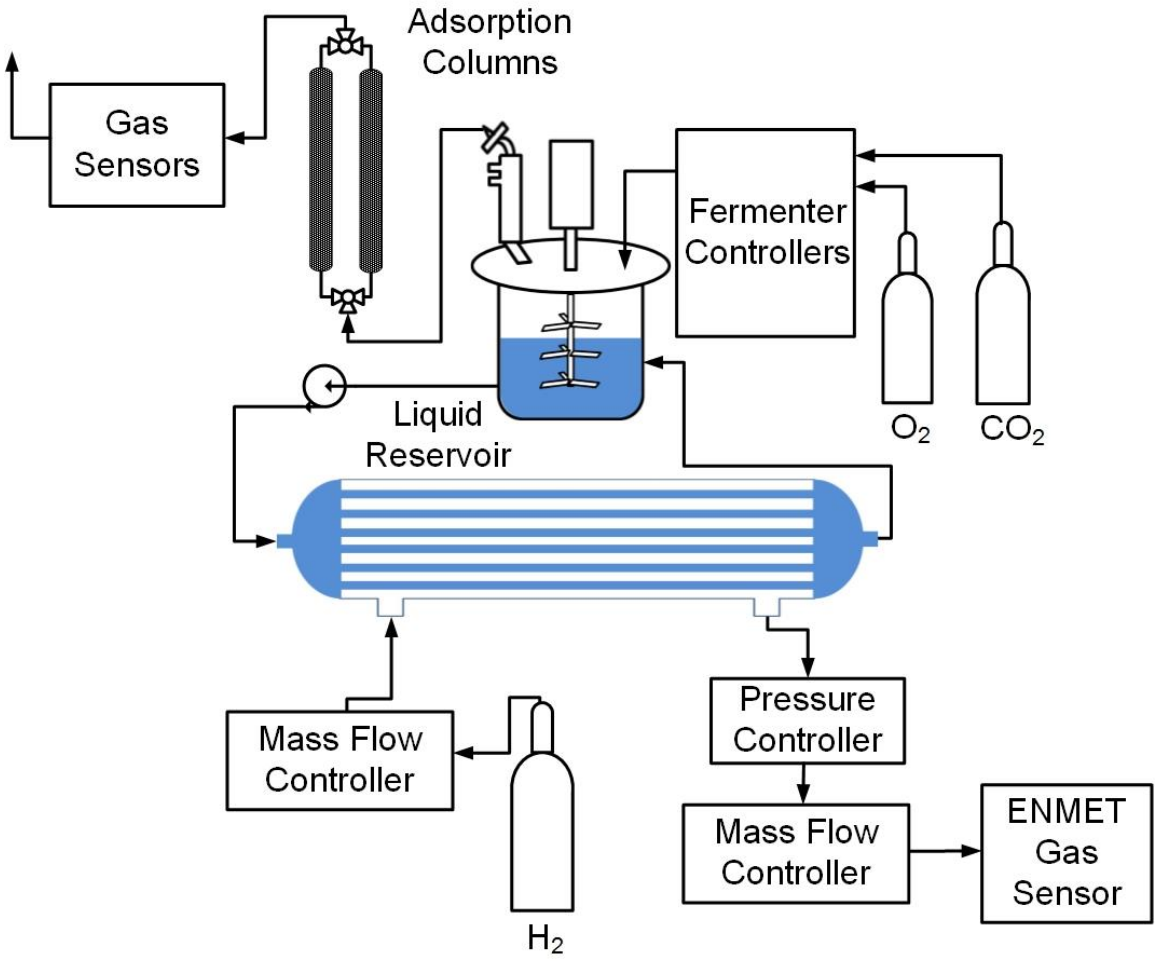

Figure 2.10 Autotrophic setup for planktonic cells with dead-end configuration on the shell side.

Figure 2.10 shows the system configuration used for autotrophic operations with planktonic (suspended) cultures of *R. eutropha*. Several improvements were made on the basis of the setups used with immobilized cells. A dead-end configuration was used for shell gas feeding to reduce the amount of gas required for the process and minimize the IBT loss in the effluent gas stream. The dead-end configuration also allows more accurate pressure control with a digital back pressure controller (Alicat Scientific, Tucson, AZ). Pure H_2 was fed to the system to avoid dilution by CO_2. The reservoir DO was controlled at 80%-100% air saturation using a mixture of air (0.4 L/min) and pure O_2. Carbon dioxide (0.2-0.3 L/min) was sparged into the reservoir liquid. The 0.5-L planktonic culture was circulated through the system using a peristaltic pump.

Two variations were used with this setup. In Setup 1, the reservoir liquid was recirculated through the lumen of the HFR, while pure H_2 was fed to the shell in a dead-end configuration at 15 psig. The recycled liquid returning from the HFR was delivered into the headspace above the reactor vessel liquid, so that any H_2-containing gas bubbles generated within the HFR would disengage from the returning liquid stream and enter the Sartorius headspace without being entrained into the agitated liquid in the Sartorius vessel. In Setup 2, H_2 was delivered to the lumen side in a dead-end configuration with pressure controlled at 15 psig, while the reservoir liquid was circulated through the shell. The recycled liquid was injected directly into the liquid within the Sartorius vessel, so that any H_2-containing gas bubbles generated within the HFR would be entrained into the agitated liquid in the Sartorius vessel. A small amount of the H_2 gas stream was vented from the BIG at designated intervals to purge any gases (e.g. CO_2) that might accumulate and dilute the H_2. The vented gas was sent through an ENMET gas sensor to ensure that O_2 never exceeded a critical level. There was no gas flow through the shell except during the occasional venting periods. The liquid stream exiting the HFR was directly injected into the

liquid in the reservoir, rather than dispensing it into the gas headspace above the liquid, as was done in Setup 1.

In both setups, the system was equipped with a glass column (I.D. 10 mm, length 50 cm, Omnifit®, Diba Industries, Danbury, CT) packed with Dowex® Optipore SD-2 polymeric resin (The Dow Chemical Company, Midland, MI) to recover IBT from the reservoir effluent gas.

Samples were collected from the reservoir for measurement of cell density, IBT and ammonium. Ammonium chloride was added as needed to avoid nitrogen limitation. Samples were collected from the culture vessel for measurement of cell density, IBT and NH_4^+. Methanol was used periodically to desorb IBT from the resin column and thereby measure the amount of IBT adsorbed. Two resin columns were alternately used for either adsorbing or desorbing IBT, so the reactor could be operated continuously without IBT accumulation to toxic levels.

2.2.6.4 Opto22-based Control Network and Safety Measures

Due to safety concerns when using H_2 gas in an aerobic environment, solenoid valves, mass flow controllers and gas sensors were used to monitor and regulate gas flow rates and composition in various regions of the BIG system. To implement centralized control over the instruments, an Opto22-based control network was constructed, as shown in Figure 2.11. The Opto22 SNAP-PAC system consisted of an automation processor and 10 I/O modules. The input modules received the analog or digital readings from the instruments and passed them on to the I/O processor, which ran the user-defined control strategies and adjusted the output signal accordingly. The output signals were then relayed to the instruments via the output modules.

Figure 2.11 shows an Opto22 control strategy used for autotrophic operation of the BIG system described in Figure 2.9. The sensors closely monitored the gas composition in the reservoir head space and HFR shell. If any mixing of H_2 and O_2 were detected, a pre-defined set

of actions would be executed to flush out the potentially hazardous mixture. If a H_2 leak were detected in the walk-in fume hood, the control system would trigger an alarm and shut the solenoid valves on the gas cylinders.

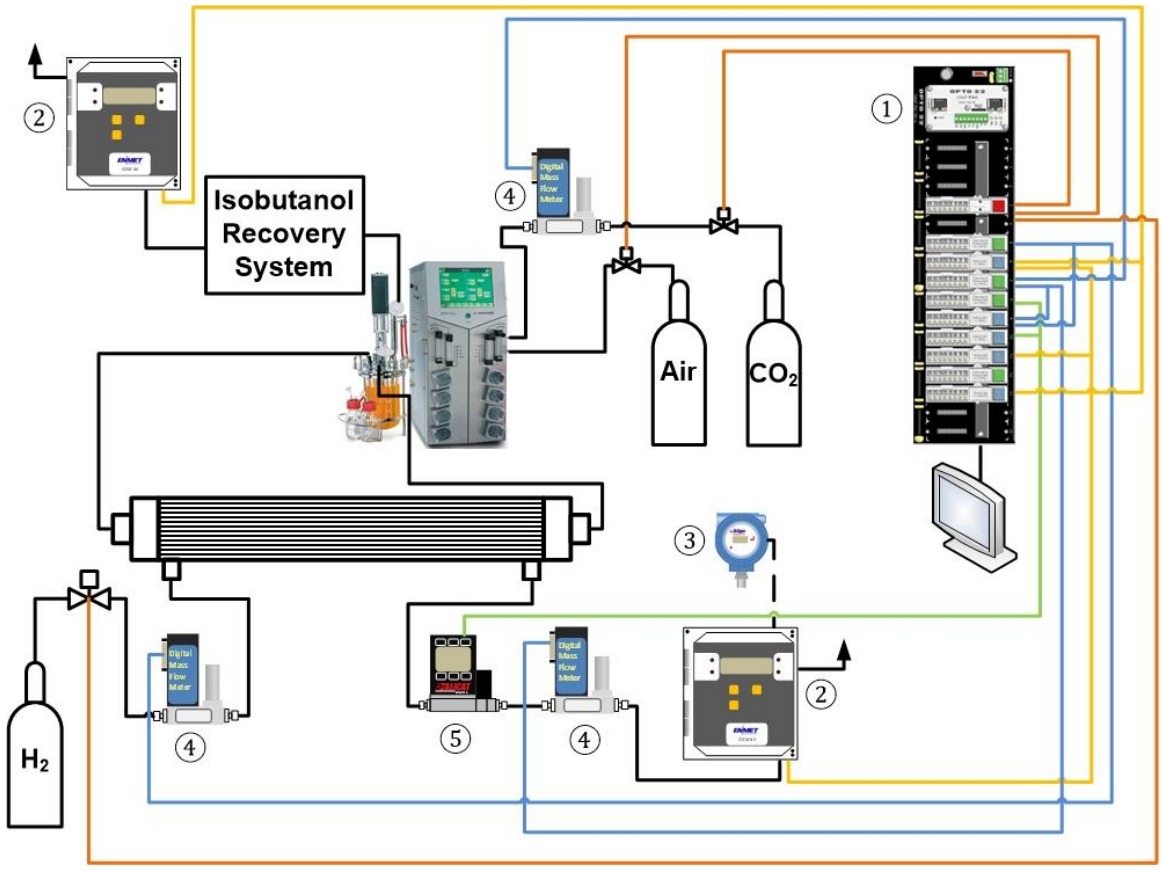

Figure 2.11 Schematic of the Opto22-based control network. ①Opto22 controllers; ②ENMET gas sensors; ③environmental H_2 sensor; ④mass flow controller; ⑤pressure controller. Black lines indicate tubings for gas and liquid transportation. Colored lines indicate the electric wires: blue-mass flow controller; orange-gas sensors; red-solenoid valves; green-pressure controller.

2.2.6.5 IBT consumption

To measure the rate of IBT uptake by the cells, IBT was fed to a 0.5 L high density culture that was initially grown on fructose to a reservoir OD of approximately 7 before the carbon feed was switched to IBT.

The fermenter's control strategy monitored the DO level in the culture. When the energy source became depleted, the cells' metabolism rapidly decreased, causing a spike in DO level. The control system was programmed to respond to such spikes by adding an aliquot of the energy source (IBT). The subsequent increase in cellular metabolism caused the DO level to drop again. In this way, the control system allowed the IBT level to be maintained at a low level to avoid toxicity, and the rate of IBT consumption to be measured by the average rate of IBT delivery to the reactor.

To avoid loss of IBT by gas stripping, an HFR was used to provide O_2 via diffusion across the membrane from the shell side in a dead-end configuration (Figure 2.12).

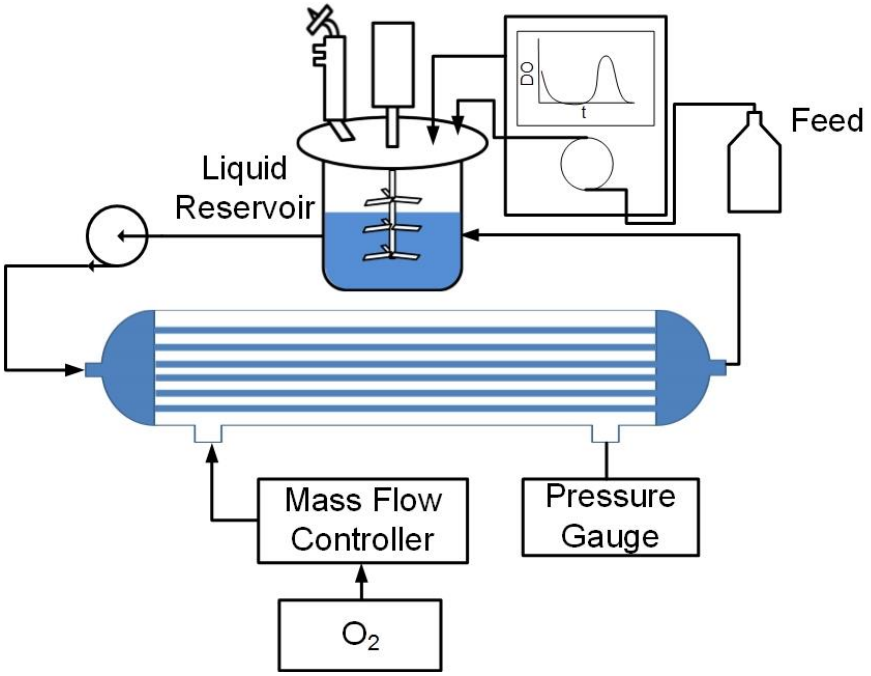

Figure 2.12 System configuration for IBT feeding experiment.

2.3 Results and Discussion

2.3.1 Cell Immobilization

Figure 2.14 shows cross-sectional SEM images of hollow fiber membranes inoculated by filtration (a) versus incubation (b). With filtration, the cells were embedded in the macroporous structure of the fiber wall, achieving a much higher cell density (Figure 2.14a) than a membrane incubated in *R. eutropha* culture for 48 h (Figure 2.14b). A similar result was obtained from fluorescamine assay (Figure 2.13). A high initial cell density could shorten the growth phase and increase the culture's resistance against contamination.

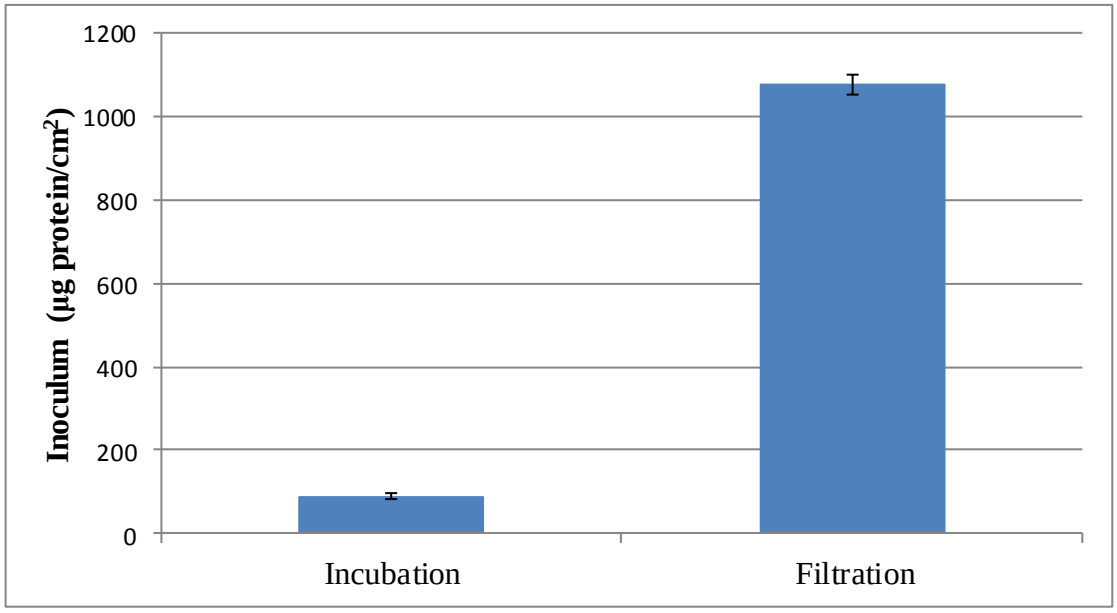

Figure 2.13 Comparison of initial cell density achieved by incubation and filtration.

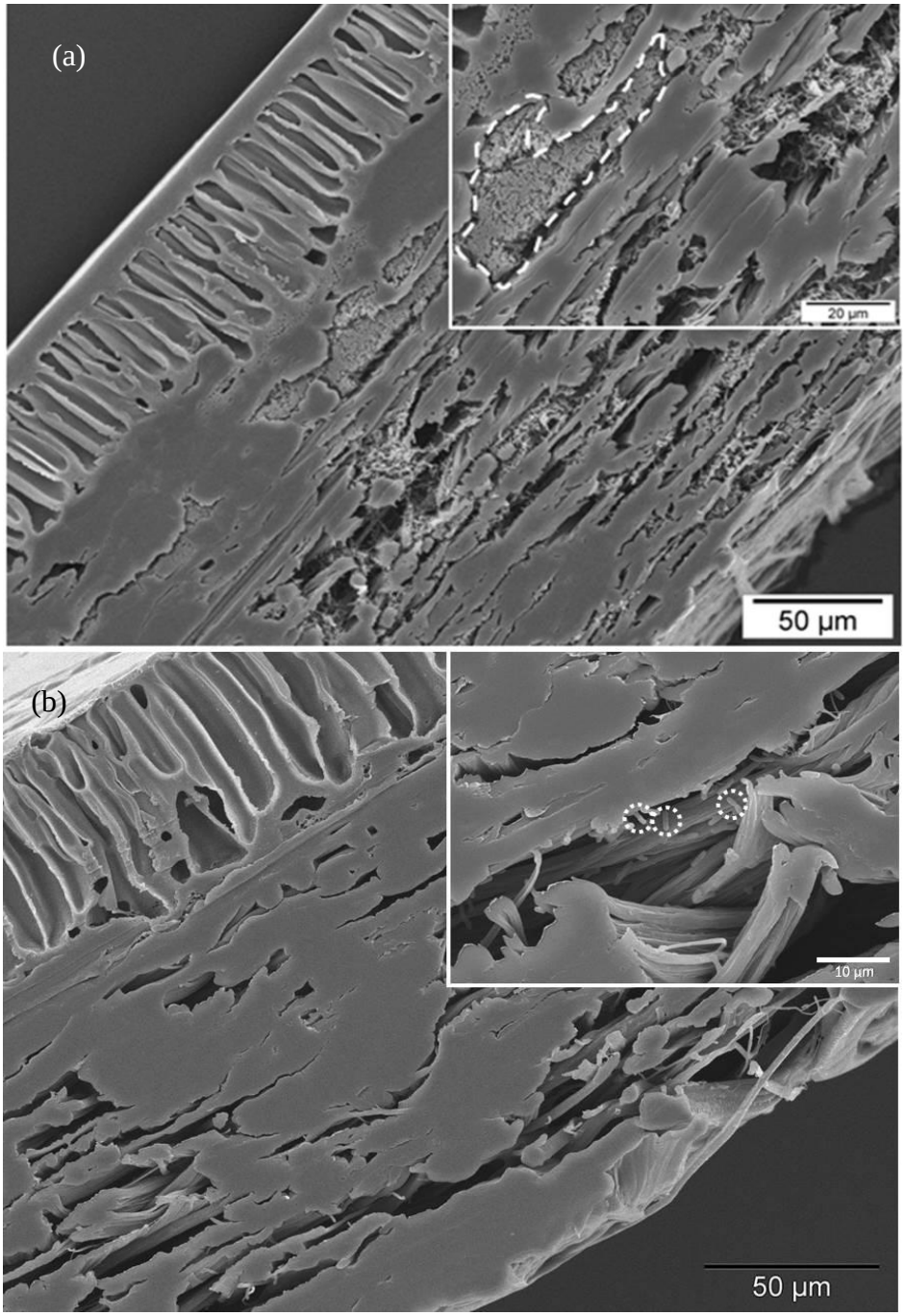

Figure 2.14 Scanning Electron Microscopy (SEM) image of XM-50 membrane cross-section (a) after filtration inoculation (b) after incubation in exponentially growing *R. eutropha* culture for 48 h.

2.3.2 BIG Operation with Immobilized Cells

The experimental results are summarized in Figure 2.15. This experiment comprised of three stages. The first stage spanned 0-168 h, when only heterotrophic feed was present. The second stage started when autotrophic operation was initiated at 168 h with fructose still present in the liquid medium and ended when the medium was replaced with fructose-free medium at 244 h. In the third and last stage only autotrophic substrates were present in the system.

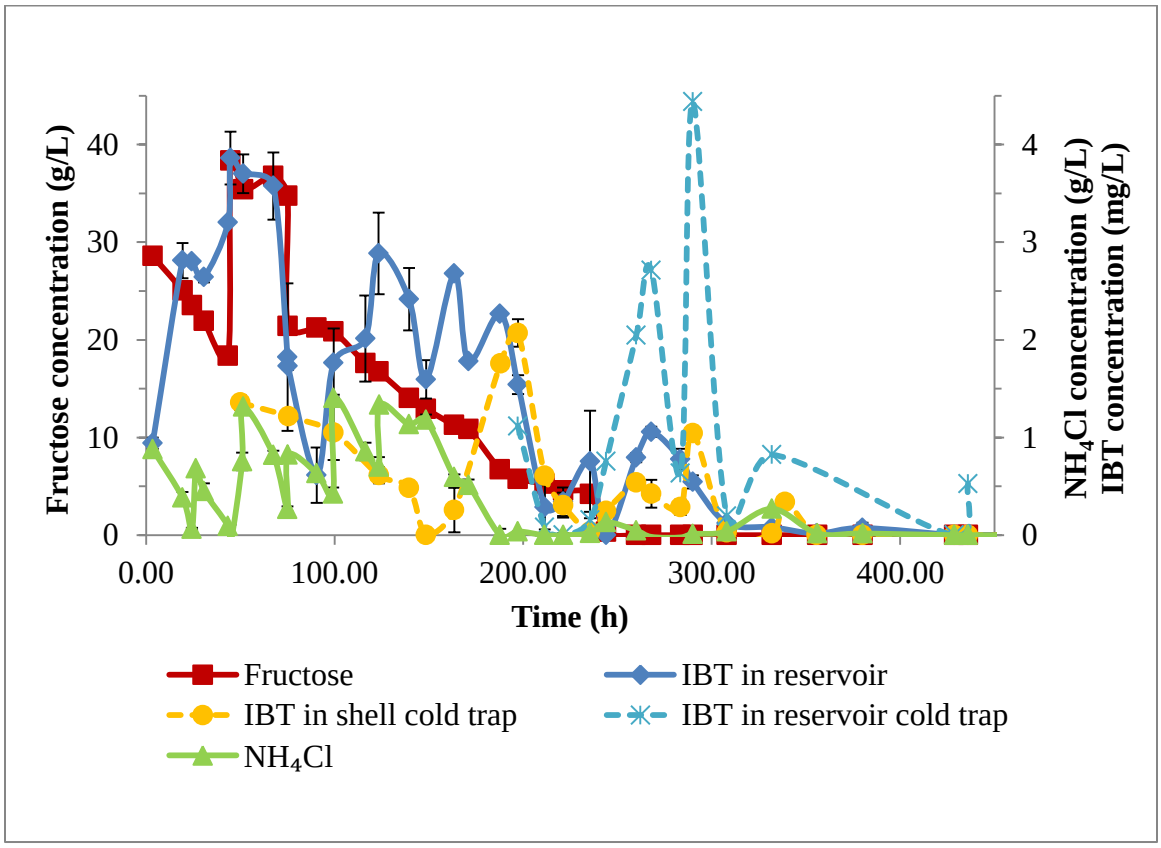

Figure 2.15 Experimental results from heterotrophic and autotrophic operation with immobilized cells.

During the first stage, IBT production occurred at low levels, most likely due to the high NH_4^+ concentration maintained to facilitate cell growth on fructose. After the autotrophic operation was initiated at 168 h, a spike in the IBT concentration in the shell side cold trap was

observed, suggesting an increase in the local IBT concentration on the outer surface of the membrane, possibly due to the addition of CO_2 as a second carbon source. A second increase in the IBT concentrations in both the shell side and reservoir exhaust cold traps was observed after the liquid in the culture was replaced with fructose-free medium at 244 h, providing preliminary evidence of IBT autotrophic production in the BIG system. The IBT concentration in the liquid reservoir reached a maximum of 1.05 mg/L at 268 h. The increased IBT concentration was accompanied by a drop in NH_4^+ concentration from 0.13 g/L to undetectable levels ($< 2\times10^{-4}$ g/L).

As NH_4^+ concentration dropped below 0.05 g/L, the IBT concentration also decreased,suggesting that a threshold concentration of NH_4Cl may be required for IBT production during the transition from heterotrophic to autotrophic operation to sustain enzyme synthesis while the cells are adapting to new carbon and energy sources. Growth of planktonic cells was first observed in lumen liquid at the same time, possibly a result of either autotrophic growth, or cell growth in the liquid phase using autotrophically produced IBT.

The BIG system was continuously operated first heterotrophically then autotrophically for a total of 19 consecutive days without contamination. Protein assays showed that the total immobilized cell mass grew from 1.56 ± 0.02 to 4.22 ± 0.58 g dry cell weight (DCW) during the experiment. Ammonium chloride concentrations suggested that most of the growth occurred during Stage 1. IBT production was measured during all stages. Initial IBT concentrations were lower than anticipated. Possible explanations for the low IBT production include a non-optimum autotrophic medium, gas mass transfer limitations, and consumption of IBT produced in one region of the hollow fiber by cells in another region.

Subsequently, two experiments with higher initial cell densities did not yield higher IBT concentrations. Various combinations of operating conditions (H_2 pressure, DO set point, NH_4^+ concentration) were also tested but did not yield a significant increase in IBT concentration**.**

2.3.3 IBT Consumption by *R. eutropha*

A hypothesis was formulated to explain the observations that the IBT production was low, was weakly influenced by the substrate concentrations, and decreased as the cell density increased. The hypothesis was that in regions of the reactor where the autotrophic carbon and energy sources were available, the cells would produce IBT, but in regions where the carbon and/or energy sources were depleted, the cells would consume IBT. In principle, the cells only need an electron acceptor (O_2) to utilize IBT as a carbon and energy source, whereas all three of the gaseous substrates (H_2, CO_2 and O_2) must be present for autotrophic IBT synthesis. Because H_2 and O_2 are provided to the cells by diffusion from opposite sides of the fiber wall, and H_2 has the highest mass-transfer challenge parameter (Table 2.1), it is conceivable that there would be regions within the fiber walls where the cells were producing IBT and other, H_2 depleted, zones that were consuming IBT. In addition, growth of cell mass within the fiber walls would simultaneously increase the gas uptake rate and decrease the gas diffusion rate by blocking pores through the fiber wall. Consequently, H_2 depletion, and thus IBT consumption, would be expected to increase at higher cell densities, consistent with the experimental trends.

To test the hypothesis, experiments were conducted to assess IBT consumption by the *R. eutropha* cells. During the fed-batch growth experiments, IBT was added on demand as the only carbon and energy source. Figure 2.16 shows the fructose, NH_4Cl and IBT concentration curves marked with arrows. IBT was added to the culture several times and immediately consumed, as indicated by the spikes in IBT concentration. The highest IBT consumption measured was 62 mg

IBT/ (g cell·h), a significant rate compared to the observed IBT production. The maximum specific growth rate on IBT was 0.033 h^{-1} with a yield of 2.13 g IBT/g DCW cell.

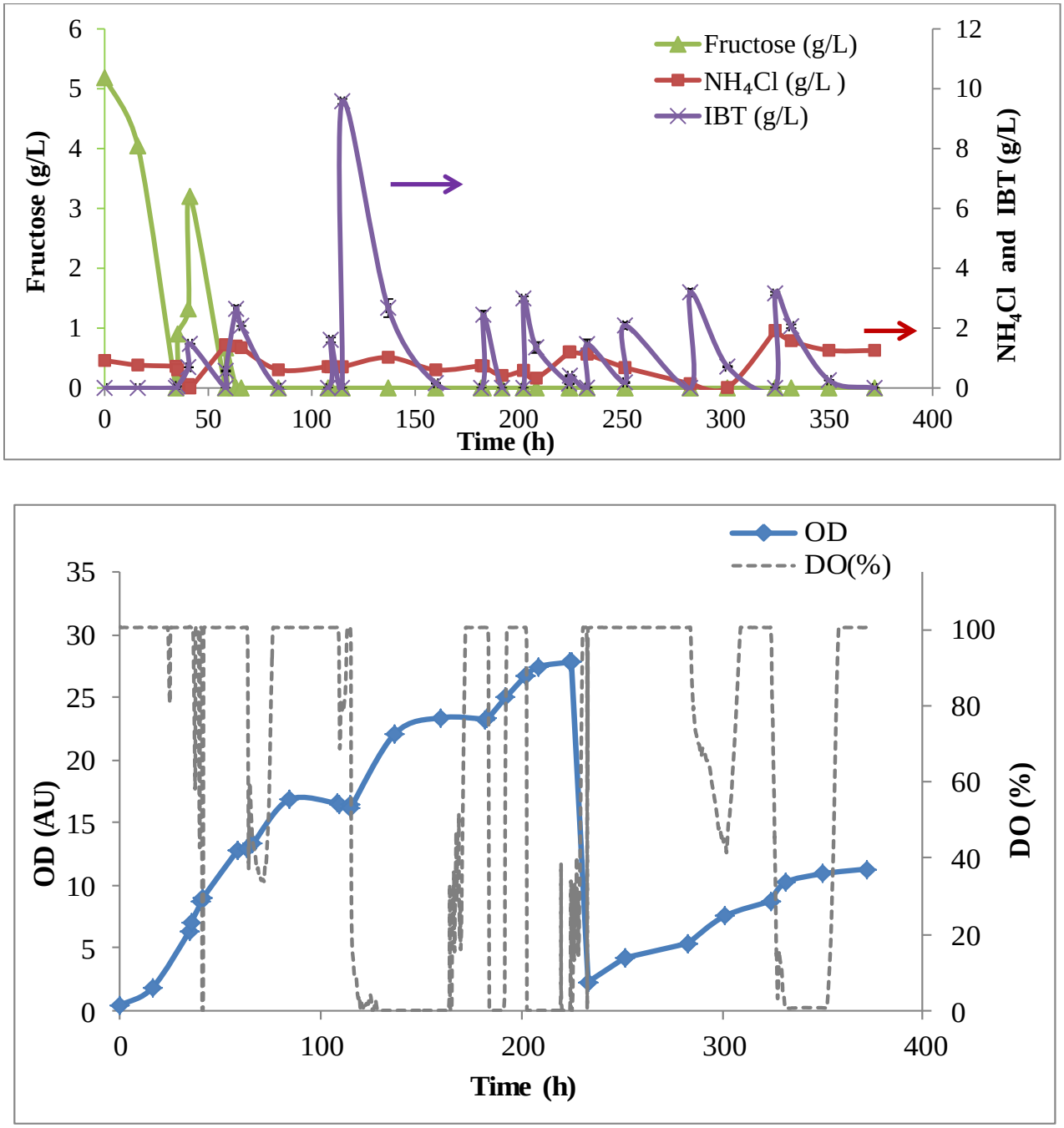

Figure 2.16 Fructose, NH_4Cl and IBT concentrations from an IBT feeding experiment using *R. eutropha* strain Re2425.

2.3.4 Autotrophic Operation with Planktonic Cells

The finding that the cells consumed IBT under aerobic conditions in the absence of other energy sources suggested that higher reactor productivity might be achieved by operating the BIG under autotrophic conditions that reduced the likelihood of forming H_2 depleted zones. Because the high cell density achieved in the hollow fiber walls could lead to rapid H_2 uptake and sharp H_2 concentration gradients in the radial direction, additional fermentation experiments were conducted using Setup 1 in which the *R. eutropha* Re2425/pJL26 cells were grown in suspension rather than being immobilized in the fiber wall. This mode of operation allowed the cell density to be readily measured by OD and adjusted if desired.

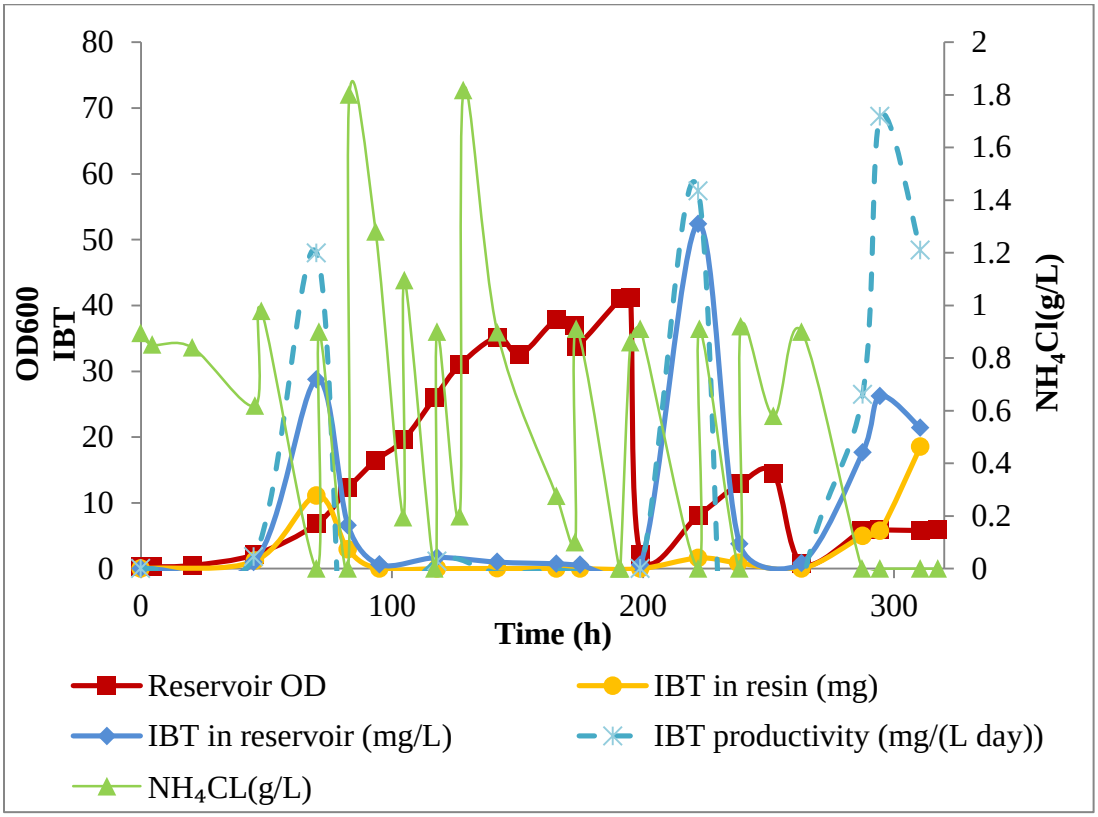

Figure 2.17 Experiment results of BIG autotrophic operation with planktonic cells.

Early in the experiment, the specific growth rate during autotrophic growth was 0.053 h^{-1}, and the IBT production rate was 48 mg/ (L·day). After 70 h (Figure 2.17) the culture's OD_{600} was 6.8 and nitrogen was limiting. To increase the productivity, cell growth was encouraged by adding NH_4Cl. The cells resumed growing at slower rate, but the net production of IBT became very low even after NH_4^+ had been depleted.

At 129 h, to confirm that minerals were not rate limiting, $CaCl_2$, $MgSO_4$ and trace elements were added, but there was no increase in IBT production. At 170 h, the culture medium was replaced with fresh medium to eliminate potentially inhibitory metabolic intermediates that might have accumulated in the liquid during fermentation. This step was achieved by centrifuging the lumen liquid at 2455×g in an Avanti® J-E centrifuge (Beckman Coulter, Inc., Pasadena, CA), and then re-suspending the cells in an equal volume of fresh medium and then returning the cell suspension to the reservoir. However, medium replacement had virtually no effect on IBT formation.

To test the hypothesis that the lack of IBT production was caused by high cell density that would cause H_2 depletion and IBT consumption, the culture was diluted to an OD_{600} of 2.2 at 199 h. After dilution, the cells began growing autotrophically again at a rate of 0.057 h^{-1} with concurrent IBT production that peaked at about 60 mg/ (L day) at an OD of about 8. The cells were diluted again at 263 h to an OD_{600} of 0.76, leading to resumption of cell growth at a specific rate of 0.084 h^{-1} and IBT production. A peak IBT production rate of about 68 mg/ (L day) was measured with specific production rate at 1.39 mg/ (g DCW h) when NH_4^+ became limiting at an OD of about 6 (Figure 2.17).

These results provided strong support for the hypothesis that H_2 limitation at high cell density causes the drop in IBT production, and are consistent with other experimental results

suggesting that IBT consumption when H_2 becomes depleted greatly reduces the net IBT production rate. In this case, as the cell density increased beyond a threshold value, IBT generation dropped precipitously.

Another autotrophic experiment was carried out with Setup 2 (Figure 2.18). The initial specific growth rate of Re2425/pJL26 under autotrophic conditions was 0.11 h^{-1}. As ammonium became limiting at 35 h, IBT was produced with a specific production rate of 6.20 mg/ (g DCW h), and a peak volumetric production rate of 323 mg/ (L day). Both of these values are higher than those achieved in Setup 1, possibly because the direct injection of the recycled liquid into the reservoir liquid allowed small bubbles of H_2 from the HFR to be dispersed throughout the liquid contents of the vessel, thereby achieving some degree of H_2 transfer to the culture in the vessel as well as the HFR.

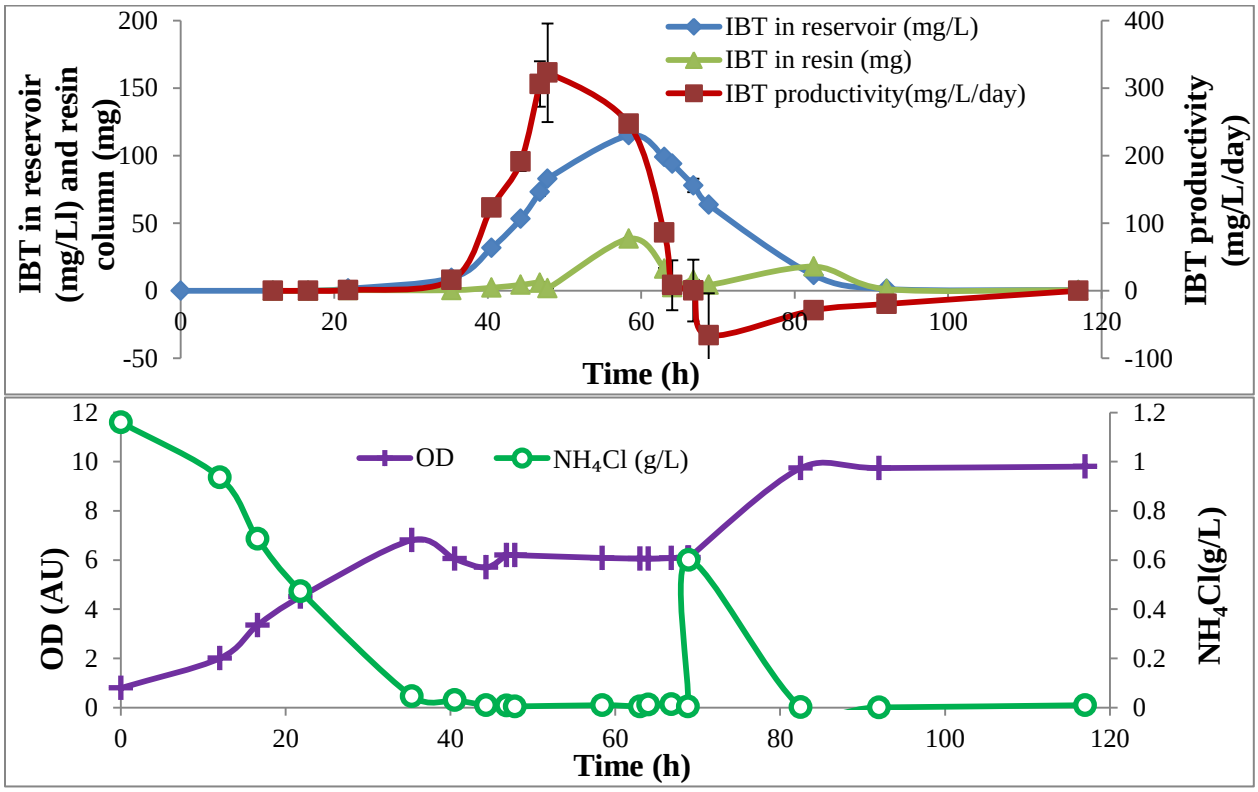

Figure 2.18 Experiment results of BIG autotrophic operation with planktonic cells.

However, when the OD reached about 10, the net IBT production plummeted, even under ammonium-limiting conditions. At around 92 h, when the BIG was not producing IBT, the CO_2 and O_2 sparging rate into vessel liquid and liquid flow rate through the shell side of HFR were increased, but IBT production did not increase. Pyruvic acid was produced at a level of about 8 g/L at low cell density, but this metabolic intermediate was also taken up by the cells at higher cell density.

The higher IBT production achieved with planktonic cells compared to immobilized cells can be attributed to the prevention of H_2-depleted zones within the reactor. The filtration-inoculation method achieved high initial cell densities, a typical inoculum used for cell immobilization was 220 mL of concentrated culture at OD_{600} of 24. The enhanced H_2 mass transfer was not sufficient to sustain such high cell density. In addition, growth of cell mass within the fiber wall would simultaneously increase the gas uptake rate and decrease the gas diffusion rate due to cell blockage of pores in the fiber wall. As a result, H_2 depletion, and thus IBT consumption, would be expected to increase at higher cell densities, consistent with the experimental trends. Also, H_2 mass transfer was enhanced by a higher supply pressure (15 psig) in experiments with planktonic cells.

2.4 Conclusions

A novel bioreactor system was constructed for autotrophic IBT production. To our knowledge, the BIG is the first bioreactor to facilitate mass transfer of two sparingly soluble, incompatible gaseous reactants without forming hazardous gas-phase mixtures. The reactor design simultaneously addresses both the mass transfer and safety issues, and therefore helps advance the Electrofuel initiative. This design could also be applied in methanotrophic fermentations, or other fermentations that simultaneously consume O_2 and a flammable gas. This

system can be operated with immobilized or planktonic cultures and offers a novel platform for autotrophic production of liquid fuels directly from cheap gas substrates, such as CO_2 and CH_4.

The relative low levels of autotrophic IBT production observed with both immobilized and planktonic cells is likely a result of consumption of cellular IBT consumption when H_2 mass transfer becomes limiting. Improved IBT production levels are likely to result if IBT consumption pathways are identified and eliminated, or if H_2 transport is further enhanced, possibly by operating the HFR at a higher pressure when stronger membranes are used.

3 MASS TRANSFER IN THE BIOREACTOR FOR INCOMPATIBLE GASES (BIG)

3.1 Background

In the BIG design, the incompatible O_2 and H_2 gases are physically separated by the hollow fiber walls. The gases diffuse into the spongy layer from opposite directions and are consumed by the immobilized cells. Under conditions in which gas mass transfer is rate-limiting, the diffusivities of the substrates and products will have a significant impact on the system dynamics. To accurately describe the mass transfer in BIG system in a mathematical model (Chapter 4) and subsequently optimize the system's operating conditions, the apparent diffusion coefficients (D_{app}) of O_2, CO_2, and IBT in the hollow fiber membranes were measured for a range of lumen liquid flow rates. The effect of flow rate on the apparent diffusion coefficients was modeled using both empirical correlation and COMSOL simulations to separate the diffusion resistance of the lumen flow and obtain accurate estimates of the diffusivities.

3.1.1 Measurement of Diffusion Coefficients in Membranes

The theoretical and experimental aspects of determining a diffusion coefficient (D) in planar membranes have been thoroughly covered in a number of books and journal articles.[57-59] A common experimental setup consists of two diffusion chambers separated by a membrane with known surface area. The liquid in the chambers is assumed to be well mixed, so there is no film resistance between the bulk liquid and the membrane. The volumes of the chambers are large enough so that the solute concentration in the chamber initially devoid of the solute can be assumed to be throughout the experiment. The solute concentration in the other chamber is measured regularly, and the total amount of diffused solute is plotted versus time. The plot is

then analyzed using a mass balance equation to determine the membrane diffusion coefficient from either the slope of the linear region (denoted steady state analysis) or the *x*-axis intercept of the extrapolated linear line (as in time lag analysis).[59, 60]

3.1.2 Diffusion in Porous Membrane

There is a large body of research on diffusion and permeation in porous membranes.[60-64] The apparent diffusion coefficient (D_{app}) of a solute relative to the aqueous diffusion coefficient (D_{iw}) is affected by the void fraction (porosity, ϵ) and tortuosity (τ) of the pore structure. If the solute partitions into the membrane, a partition coefficient, K_p, can be used to analyze the data. In macroporous and microporous membranes with pore sizes ranging from 5 nm to 1.0 μm, the apparent diffusion coefficient is described using Equation 3.1.

$$D_{app} = D_{iw}\frac{\epsilon K_p}{\tau} \qquad 3.1$$

Since immobilized cells can occupy space in pores and thus reduce the membrane's porosity, the apparent diffusion coefficient is likely to be affected by the density of immobilized cells. However, there is no consensus in the literature regarding how to compensate for such effects. Mignot and Junter[59] found that diffusivities of L-malic acid and glucose in an agar membrane decreased linearly with the logarithm of cell density for cell densities between 20 ng and 2 mg dry cell wt./ cm^3 agar. Linear and quasi-linear correlations between cell density and diffusion coefficient were also reported for cell densities up to 300 mg wet wt. /g gel in polyacrylamide gel membrane[65] and at 40 mg dry wt. /cm^{-3} gel in Ca-alginate beads[66]. Hannoun and Stephanopoulos[60] found no effect of 20 wt.% yeast cells on the apparent diffusion coefficient of glucose and alcohol in 2% alginate membrane. However, the 2 % agar membranes used in the studies mentioned above have an estimated nominal pore size of 500-700 nm[67], and

the alginate beads have surface pore sizes between 6.8 and 16.6 nm[68], much smaller than the pore size in the XM-50 membrane spongy layer (Figure 3.2a). Moreover, the solutes used in these studies are organic molecules such as fructose and L-malic acid, all of which are significantly larger than the gas molecules used in BIG. It's likely that in the macroporous spongy layer of a membrane such as XM-50 with pore sizes on the order of 10 μm (Figure 3.2c), the effect of porosity on gas diffusivity is very slight, and the majority of diffusion resistance stems from the skin layer, which has a molecular weight cut-off (MWCO) at 50 kDa. According to a correlation established by Guo and Santschi[69], a 50-kDa MWCO has a nominal pore size of 5 nm. Since the skin layer's pore size is too small to allow *R. eutropha* cells to be embedded, its diffusion resistance will not be affected by cell immobilization.

There is very little literature on immobilized cells in macroporous polymer membrane with pore sizes significantly larger than that of gel membranes, but the effect of immobilized cells on solute diffusivity in the spongy layer can be estimated using data from biofilms. Stewart[70] reviewed experimental measurements of effective diffusion coefficients in biofilms, as summarized in Figure 3.1. The general trend suggests that higher cell densities could result in more significant diffusion retardation. The diffusion coefficient in biofilms with the highest cell density, 400 g/L, is 9% of the aqueous value. However, at less extreme cell densities (up to 50 g/L) the diffusion coefficients through biofilm are on the same magnitude as in water. It is reasonable to assume that the diffusion coefficients through the immobilized cells are similar to that those obtained in biofilms with similar cell densities.

Therefore, the membrane diffusivities measured with empty membranes were measured and used as reasonable estimates for model simulation at low cell densities.

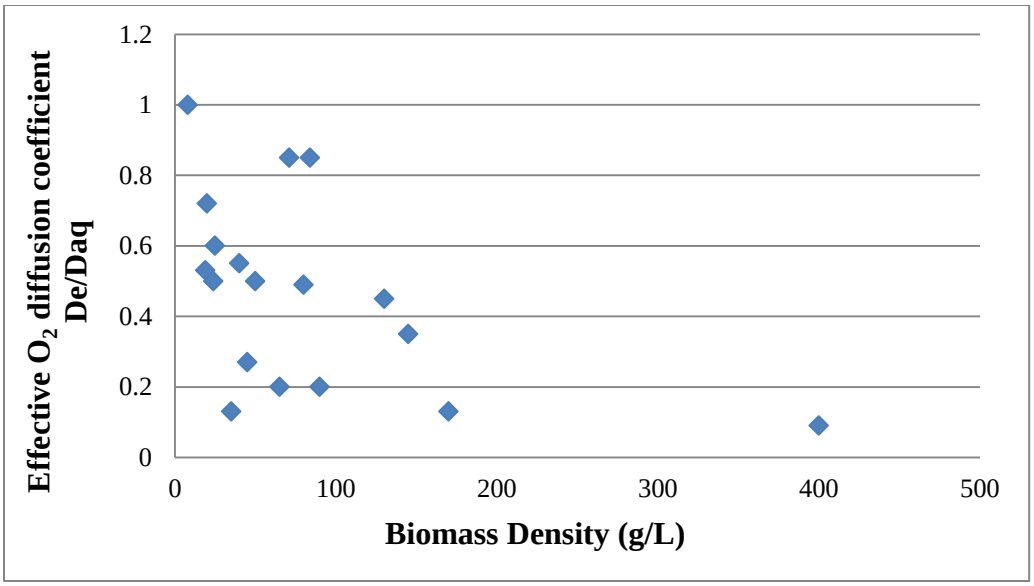

Figure 3.1 Summarized relative diffusion coefficient of O_2 in biofilm.[70]

Figure 3.2b and c are SEM (JEOL JSM-6610LV Scanning Electron Microscopy) images of inner and outer surfaces of XM-50 hollow fiber membranes, respectively. The inner surface seems smooth at the magnification of 4500, suggesting very small pore size. The XM-50 membrane has a molecular weight cut-off (MWCO) of 50 kDa, which corresponds to a nominal pore size of 5 nm according to Guo et al..[69] On the contrary, the outer surface of the membrane exhibits pores on the order of 10-100 μm.

The SEM images of XM-50 membrane cross section (Figure 3.2a) show two distinct layers: one with lateral pores facing the outer (shell) surface and one with comb-shape pores residing closer to the inner (lumen) surface of the membrane. The comb-shape pores have sizes large enough to embed *R. eutropha* cells, but in an image of membrane cross section with immobilized cells (Figure 2.14a), very few cells are observed in the comb-shape layer. Therefore, the interface between the two layers must also have small pore sizes as well as the inner surface.

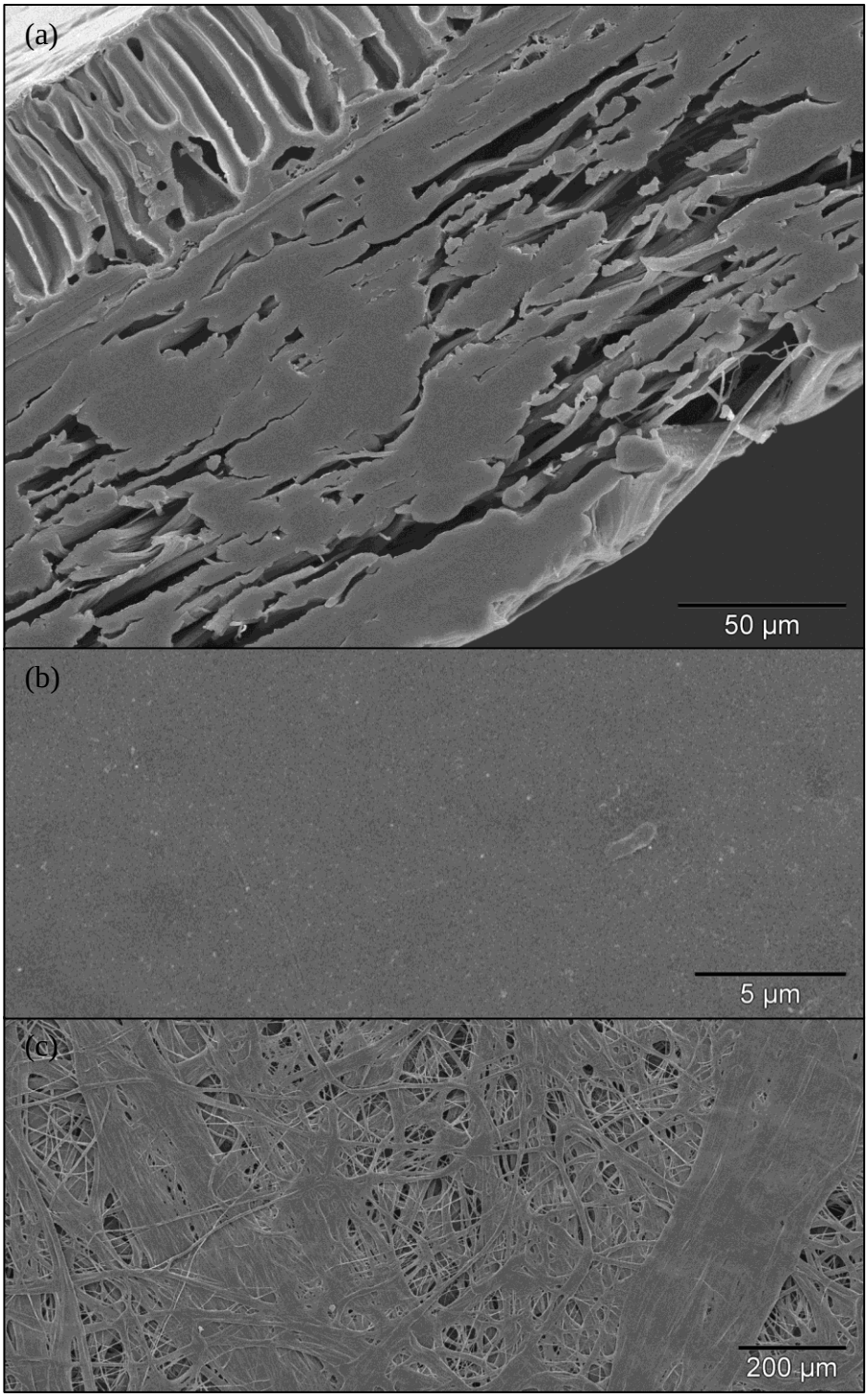

Figure 3.2 (a)SEM image of XM-50 membrane cross section. Upper left side is the lumen surface. The support layer has a macroporous structure with size on the order of 10 nm. (b) Inner surface of XM-50 hollow fiber membrane. (c) Outer surface of XM-50 hollow fiber membrane.

3.2 Experimental Setup

3.2.1 Measuring O_2 Membrane Diffusivity

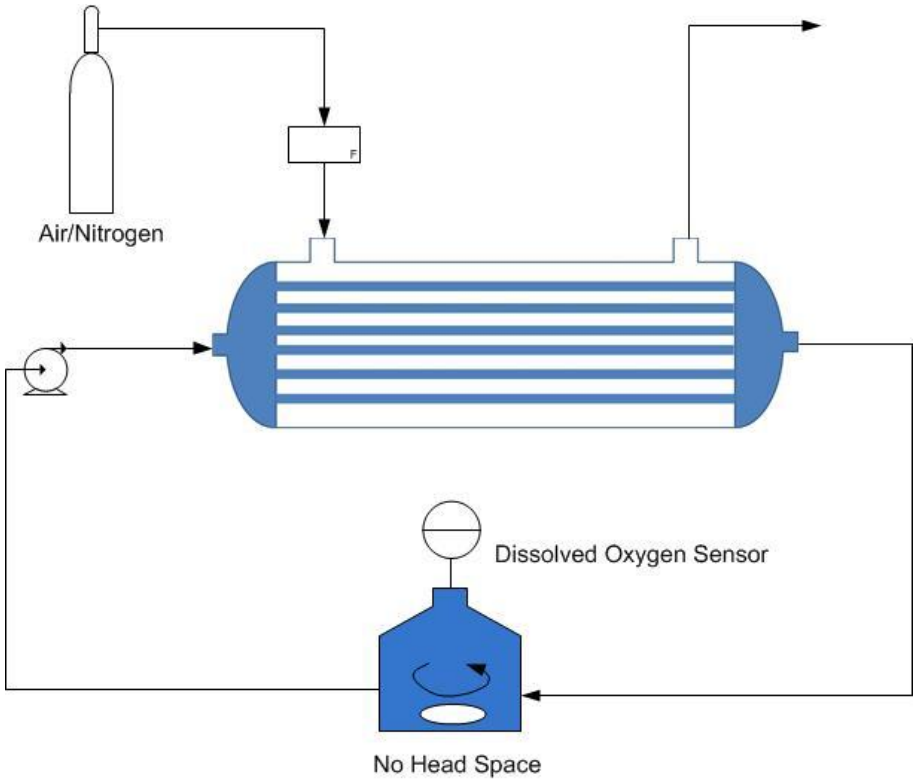

Figure 3.3 Schematic of the experimental system used to measure O_2 mass transfer between the gas phase in the shell and the aqueous phase circulating through the fiber lumen.

The experimental system is shown schematically in Figure 3.3. The membrane diffusivity of O_2 was originally measured in mixed cellulose ester fiber (X32M-601-02N, Spectrum Labs, Inc., Rancho Dominguez, CA), and additional measurements were made in XM-50 (polyacrylonitrile-polyvinyl chloride copolymer) membrane (HF, 1018-1.0-45-XM50, Koch Membrane Systems, Wilmington, MA). Purified water was recirculated through the hollow fiber lumen and a small, well-mixed liquid reservoir that contained a dissolved O_2 (DO) sensor. When measuring O_2 diffusivity in cellulose ester membrane, the reservoir volume was 16 mL. An

optical dissolved O_2 sensor was kindly provided by Prof. Ruby Ghosh[71]. The N_2 flow rate through the reactor shell was 385 mL/min. The O_2 diffusivity in the XM-50 membrane was measured using a Sartorius® Bplus fermentation vessel as the liquid reservoir with a 1.5 L volume and the fermentor's built-in dissolved O_2 sensor. Liquid flow was circulated using a peristaltic pump with a Masterflex standard pump head (Cole-Parmer, Vernon Hills, IL). N_2 gas was continuously fed through the shell at a flow rate of 1 L/min to provide a driving force for O_2 diffusion. It is essential in the setup to leave no headspace in the liquid reservoir, since otherwise the liquid-gas mass transfer between the reservoir liquid and headspace would interfere with the measurement.

3.2.2 Measuring CO_2 Membrane Diffusivity

The process of CO_2 dissolution in water is complicated by its coupling with dissociation of carbonic acid. High levels of dissolved CO_2 can lead to a drop in pH value, and, as a result, the rate of dissolution can be limited by the rate of bicarbonate formation from dissolved CO_2.

To avoid these complications, the system shown schematically in Figure 3.4 was used to measure the CO_2 diffusion coefficient in cellulose ester membranes (X32M-601-02N, SpectrumLabs, Inc., Rancho Dominguez, CA). Reverse-osmosis purified water equilibrated with air (21% O_2, 79% N_2) was pumped through the lumen without recirculation using a peristaltic pump (Model 7523-00 with Quick-load® pump head model 7021-20) while a gas mixture with an initial composition of 5% CO_2, 21% O_2 and balance N_2 was recirculated though the shell at 105 mL/min. Changes in the CO_2 concentration in the gas phase were then monitored as a function of time using a gas-phase CO_2 sensor (Series 9500, Alpha Omega Instruments, Lincoln, RI).

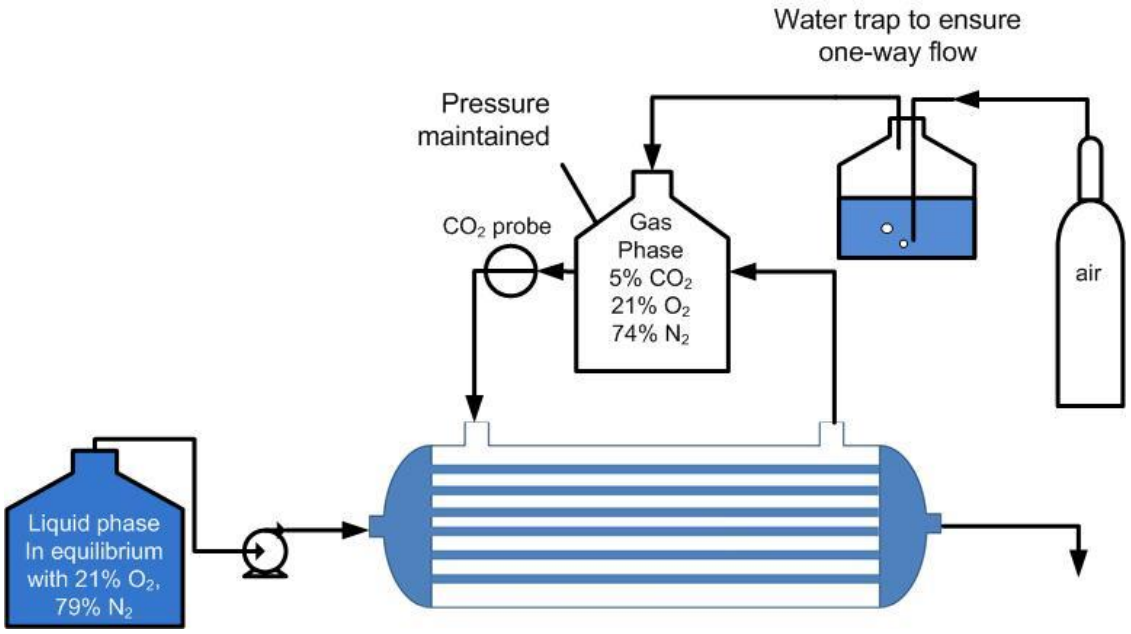

Figure 3.4 Schematic of the experimental system used to measure CO_2 mass transfer between the gas phase in the shell and the aqueous phase circulating through the fiber lumen.

By keeping the liquid flow rate through the lumen relatively high, a very low liquid-phase CO_2 concentration was maintained, circumventing the complication with carbonic acid formation at high CO_2 concentrations. Since the liquid was in equilibrium with 21% O_2, there was no driving force for O_2 mass transfer across the membrane. Also, since the Henry's law constant of N_2 (1,639 L·atm/mol) is much greater than that of CO_2 (29.4 L·atm/mol)[72], the flux of N_2 desorbed into the gas was much smaller than that of CO_2 adsorption and could be neglected. As CO_2 dissolved into the liquid stream, the total amount of gas in the reservoir was reduced. To avoid a reduction in pressure, the reservoir was connected to an air cylinder with a water trap that releases air (21% O_2 and 79% N_2) into the chamber as the CO_2 diffused across the membrane.

3.2.3 Measuring IBT Membrane Diffusivity

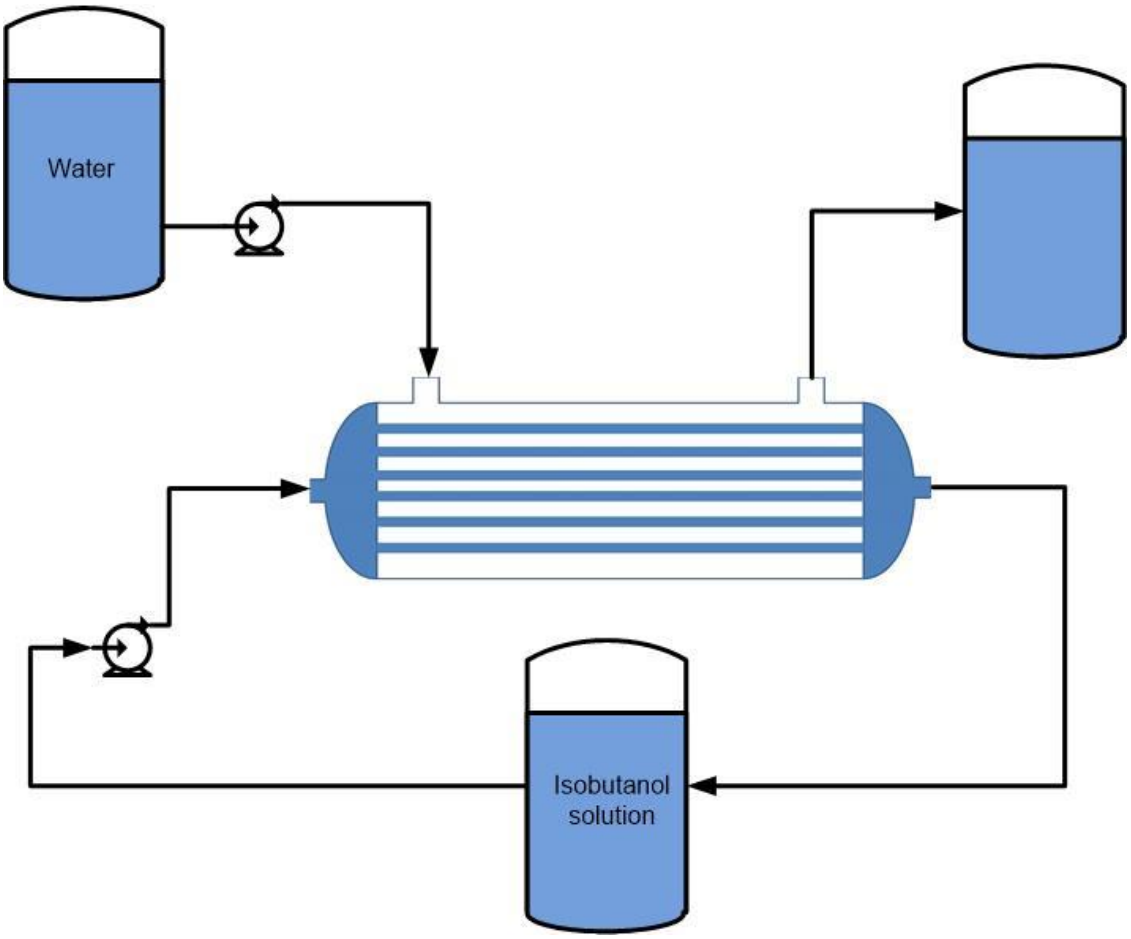

Figure 3.5 System configuration for measuring IBT apparent diffusion coefficient across the XM-50 membrane.

The IBT diffusion coefficient in the XM-50 hollow fiber membrane was measured using the experimental system shown in Figure 3.5. The system consisted of a hollow fiber module (HF, 1018-1.0-45-XM50, Koch Membrane Systems, Wilmington, MA) and a well mixed 200-mL reservoir that contained an IBT aqueous solution. The IBT solution had an initial concentration, C_0, of 5 g/L (0.068 M), and was continuously recycled through the fiber lumen at various flow rates using a peristaltic pump with Masterflex Easy-Load® pump head (Cole-Parmer, Vernon Hills, IL). Since the water flow through shell was not recycled, the IBT

concentration in the shell was assumed to be zero, so the driving force for IBT diffusion was only a function of IBT concentration in the lumen side. Liquid samples were taken from the reservoir regularly and analyzed using a Bruker® GC-450 gas chromatograph (Bruker Corporation, Billerica, MA) outfitted with a Varian® CP7416 column and an flame ionization detector.

The setups used for measuring membrane diffusivities of O_2, CO_2 and IBT are summarized in Table 3.1.

Table 3.1 Summary of the experimental setups used to measure diffusion coefficients of O_2, CO_2 and IBT.

Solute	Diffusion Direction	Measured Concentration
O_2	Lumen liquid → Shell gas	Dissolved O_2 in lumen liquid
CO_2	Shell gas → Lumen liquid	CO_2 composition in shell gas
IBT	Lumen liquid → Shell liquid	IBT in lumen liquid

3.3 Data Analysis

3.3.1 O_2

Even though the systems used to measure diffusion coefficients of O_2, CO_2 and IBT varied from one another, their designs all aimed to obtain a negligible solute concentration on one side of the membrane, thus making the diffusion driving force only the function of concentrations on the other side. Therefore the data analysis for the three solutes was similar. The method used for the O_2 diffusion coefficient measurement is described below as an example. Three approaches were used (described in Sections 3.3.1.1-3.3.1.3). In the analysis, all the membrane diffusion coefficients were assumed isotropic.

3.3.1.1 Simplistic calculation

An unsteady-state mass balance on O_2 in liquid phase was developed to calculate the apparent diffusion coefficient across the membrane (Equation 3.2). V_T is the total liquid volume in the system; $C_{reservoir,O_2}$ is the O_2 concentration as measured in the reservoir; $N|_{r=R_1}$ is the diffusion flux at membrane inner surface; D_{app,O_2} is the apparent O_2 diffusion coefficient in the membrane, and $A_{membrane}$ is the membrane area.

$$V_T \frac{dC_{reservoir,O_2}}{dt} = N|_{r=R_1} A_{membrane} = D_{app,O_2} \left.\frac{dC_{O_2}}{dr}\right|_{r=R_1} A_{membrane} \quad 3.2$$

In the first approach, denoted "simplistic" derivation, the mass balance was based on the following assumptions: 1) the curvature in the membrane fiber wall was negligible ($\left.\frac{dC_{O_2}}{dr}\right|_{r=R_1} = \frac{C_{lumen,O_2}}{\Delta r}$); 2) the liquid in the entire system, including the reservoir liquid and the dead volume in the tubing and reactor, had a constant volume and was well mixed, with negligible axial and radial dissolved O_2 concentration gradient ($C_{lumen,O_2} = C_{reservoir,O_2}$).

Based on these assumptions, Equation 3.2 can be integrated to give Equation 3.3, whose form suggests that the natural log of dissolved O_2 concentration should follow a linear relationship with respect to time with N_2 flow in the shell side, and that the slope is a function of the apparent diffusion coefficient of O_2 across the membrane ($D_{app,\,O_2}$).

$$\ln(C_{reservoir,O_2}) = -\frac{D_{app,O_2} A_{membrane1}}{\Delta r V_T} t + ln\left(C_{reservoir,O_2,0}\right) \quad 3.3$$

$$A_{membrane1} = 2\pi R_1 LN \quad 3.4$$

In Equation 3.3, D_{app,O_2} is the apparent diffusion coefficient of O_2 between the lumen liquid stream and gas phase in the shell side, $A_{membrane1}$ is the hollow fiber membrane area, Δr is

the thickness of hollow fiber membrane, and V_T is the total liquid volume in the system (lumen, tubing, and reservoir).

3.3.1.2 Rigorous Calculation

While the above-mentioned assumptions greatly simplify the derivation, they are not strictly valid. First, the curvature of the membrane wall may not be negligible for the geometries used. The thickness of the XM-50 hollow fibers is 0.033 cm, and the ID is 0.11 cm; also, the thickness of the cellulose ester hollow fiber is 0.015 cm, and the fiber ID is at 0.1 cm. Second, even though a significant portion of the liquid in the system is well-mixed, the rest of the liquid in the lumen space doesn't have a uniform concentration. Third, at lower lumen flow rates, there is likely to be a significant drop in O_2 concentration between the inlet and outlet. Taking all of these factors into account but ignoring radial O_2 concentration gradients within the lumen, Equation 3.5 (denoted the "rigorous" calculation) was derived, and the detailed derivation is included in Appendix A.

$$lnC_{reservoir,O_2} = \frac{F_L}{V_R}\left(exp\left(-\frac{2D_{M,O_2}\pi NL}{F_L ln\frac{R_2}{R_1}}\right)-1\right)t + lnC_{reservoir,O_2,0} \qquad 3.5$$

where:

F_L = Flow rate of liquid in the lumen [m^3/min]

V_R = Reservoir volume [m^3]

L = Fiber length [m]

D_{M,O_2}= O_2 Membrane diffusion coefficient [m^2/min]

N = Number of fibers

R_1= Fiber inner radius [m]

R_2 = Fiber outer radius [m]

3.3.1.3 COMSOL Simulation

The membrane diffusivity experiments were simulated using COMSOL Multiphysics®. COMSOL Multiphysics® is a powerful commercial software package capable of simulating coupled physics phenomena, ranging from chemical reactions and diffusion to acoustics and electromagnetics, in a 3-dimensional space. The software creates a mesh in the model space and uses finite element method (FEM) to solve the models, with the error controlled using a variety of numerical solvers.

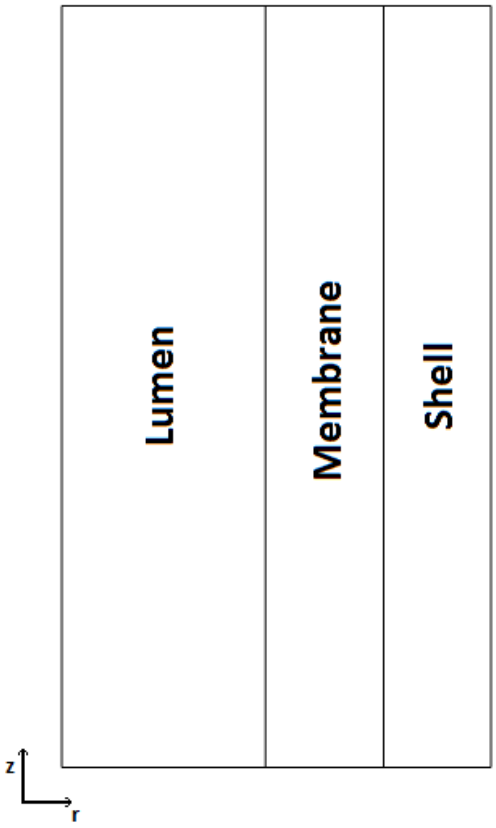

Figure 3.6 Geometry of a single fiber in the hollow fiber reactor.

The axisymmetric model constructed in COMSOL included 3 domains: lumen, membrane and shell (Figure 3.6). The phase in each domain was assigned according to the specific experimental setup, and the dimensions of each domain were defined according to the membrane module used. Since in the experiments the membranes were saturated with water, the membrane domain was assumed to be an aqueous phase. The calculated Reynolds number of the lumen flow ranged between 5 and 160, and therefore the lumen flow was assumed to be fully developed laminar flow with a parabolic velocity profile. Since the cross section of the reactor shell had a highly irregular shape, the shell flow was assumed to be turbulent and have a uniform concentration. Mass balance equations were used to describe both diffusive and convective mass transfer in lumen and shell (Equation 3.6), whereas convection was considered negligible in the membrane domain (Equation 3.7). An ordinary differential equation (Equation 3.8) was used to update the reservoir concentration based on the reservoir volume, flow rate and effluent concentration. The natural log of the reservoir concentration was plotted against time, and the membrane diffusion coefficient was varied in the simulation until the slope matched the experimental result.

$$\frac{\partial C_i}{\partial t} + \nabla \cdot (-D_i \nabla C_i) + u \cdot \nabla C_i = 0 \tag{3.6}$$

$$\frac{\partial C_i}{\partial t} + \nabla \cdot (-D_i \nabla C_i) = 0 \tag{3.7}$$

$$V_R \frac{dC_{i,reservoir}}{dt} = F(C_{i,outlet} - C_{i,reservoir}) \tag{3.8}$$

In Equation 3.6 and 3.7, C_i is the concentration of a chemical species with diffusion coefficient D_i. The flow velocity in either lumen or shell is represented by u. In Equation 3.11, V_R is the reservoir volume, $C_{i,reservoir}$ is the concentration in the reservoir, $C_{i,outlet}$ is the

average concentration at the lumen outlet for O_2 and IBT, and shell outlet concentration for CO_2. F is the lumen flow rate for O_2 and IBT, and shell flow rate for CO_2.

The concentrations of all chemical species at the lumen-membrane interface are assumed to be continuous. Instantaneous gas-liquid equilibria are assumed for gaseous substrates and volatile chemical species, such as IBT, at the membrane-shell interface.

A comparison of the assumptions made in the three types of calculations is summarized in Table 3.2. The COMSOL model used the fewest simplifying assumptions and took into account the mass transfer in lumen radial and axial directions. The COMSOL results therefore represent only the membrane diffusion coefficient instead of the compounded "apparent" diffusion coefficient, so the COMSOL predictions are considered the most accurate of the three approaches.

Table 3.2 Comparison of the assumptions made in three different types of calculation.

Type of Calculation	**Assumptions**
Simplistic (Equation 3.3)	1) No membrane curvature 2) No concentration gradient in the radial and axial direction 3) All the liquid in the system is well mixed (no dead volume in the reactor lumen)
Rigorous (Equation 3.5)	1) Membrane curvature accounted 2) No concentration gradient in the radial direction 3) Concentration gradient in the axial direction in the space originally containing solute 4) Dead volume in the reactor lumen
COMSOL	1) Membrane curvature accounted 2) Concentration gradient in lumen radial direction 3) Concentration gradient in the axial direction 4) Dead volume in the reactor lumen

3.3.2 CO_2

A mathematical model analogous to that previously described for measuring O_2 transfer was applied to determine the apparent CO_2 diffusion coefficient (D) across the spongy layer. The

equations derived from simplistic (Equation 3.9) and rigorous (Equation 3.11) calculations are listed below. The derivation is also attached in appendix A. Since the CO_2 content was measured in partial pressure, the variables used in the derivation have been adapted accordingly.

$$lnP_{reservoir,CO_2} = -\frac{D_{app,CO_2} A_{membrane2} RTk_H}{\Delta r V_T} t + lnP_{reservoir,CO_2,0} \quad 3.9$$

$$A_{membrane2} = 2\pi R_2 LN \quad 3.10$$

$$lnP_{CO_2,reservoir} = \frac{F_G}{V_R}\left(exp\left(-\frac{2\pi N D_{app,CO_2} Lk_{H,CO_2} RT}{F_G ln\frac{R_2}{R_1}} \right) - 1 \right) t + lnP_{CO_2,reservoir,0} \quad 3.11$$

The slope was determined using linear regression and then used to calculate the corresponding D_{app} value. The process was repeated three times for each of four different liquid flow rates.

3.3.3 Isobutanol

The experimental setup of IBT apparent diffusion coefficient measurement was very similar to that used for O_2 in that they both measure the solute diffusion from lumen to shell, and therefore the equations derived from simplistic (Equation 3.12) and rigorous (Equation 3.14) calculations were also similar:

$$lnC_{reservoir,IBT} = -\frac{D_{app,IBT} A_{membrane1}}{\Delta r V_T} t + lnC_{reservoir,IBT,0} \quad 3.12$$

$$A_{membrane1} = 2\pi R_1 LN \quad 3.13$$

$$lnC_{reservoir,IBT} = \frac{F_L}{V_R}\left(exp\left(-\frac{2D_{app,IBT}\pi NL}{F_L ln\frac{R_2}{R_1}} \right) - 1 \right) t + lnC_{reservoir,IBT,0} \quad 3.14$$

3.4 Results

An example of the natural log of dissolved O_2 (DO) versus time plot is shown in Figure 3.7. As expected, the plot is highly linear. The slope was determined using linear regression and then used to calculate the corresponding D_{app,O_2} value using both simplistic (Equation 3.3) and rigorous (Equation 3.5) derivations. The results obtained from 4 different liquid flow rates are summarized in Table 3.3.

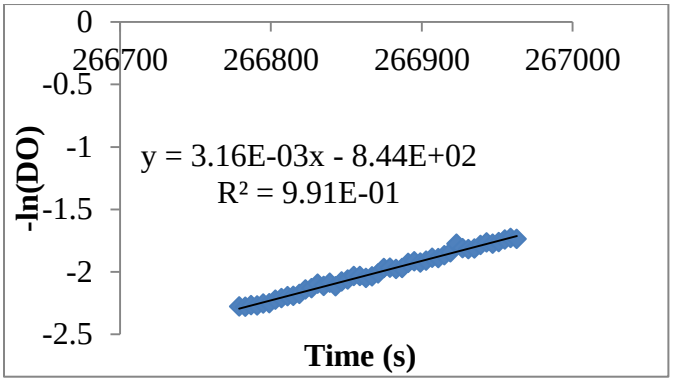

Figure 3.7 Dissolved O_2 versus time data used to determine the apparent diffusion coefficient for oxygen through the spongy layer of the hollow fiber membrane.

Table 3.3 Apparent diffusion coefficients for O_2 transport across the spongy layer of the hollow fiber membrane.

Liquid Flow Rates (mL/min)	**D_{app,O_2} ($\times 10^{-10}$ m^2/s) (simplistic calculation)**	**D_{app,O_2} ($\times 10^{-10}$ m^2/s) (rigorous calculation)**
15	8.93 ± 0.03	5.05 ± 0.02
47	11.50 ± 1.17	5.97 ± 0.64
72	13.99 ± 0.92	7.16 ± 0.35
95	14.29 ± 0.38	7.27 ± 0.20

Data collected from CO_2 and IBT diffusion measurement experiments were processed using corresponding equations, with calculated results summarized in Table 3.4 and Table 3.5.

Table 3.4 Apparent diffusion coefficients for CO_2 transport across the spongy layer of the hollow fiber membrane.

Liquid Flow Rates (mL/min)	**D_{app,CO_2} ($\times 10^{-10}$ m^2/s) (simplistic calculation)**	**D_{app,CO_2} ($\times 10^{-10}$ m^2/s) (rigorous calculation)**
15	3.30 ± 0.07	2.90 ± 0.06
49	4.52 ± 0.08	3.98 ± 0.07
73	5.01 ± 0.32	4.42 ± 0.28
100	5.27 ± 0.39	4.65 ± 0.35

Table 3.5 Apparent diffusion coefficients for IBT transport across the spongy layer of the hollow fiber membrane.

Liquid Flow Rates (mL/min)	**$D_{app,IBT}$ ($\times 10^{-10}$ m^2/s) (simplistic calculation)**	**$D_{app,IBT}$ ($\times 10^{-10}$ m^2/s) (rigorous calculation)**
22	1.42 ± 0.40	0.91 ± 0.03
45	2.03 ± 0.25	1.20 ± 0.05
58	2.15 ± 0.14	1.34 ± 0.09
80	2.86 ± 0.19	1.78 ± 0.12
132	3.61 ± 0.44	2.24 ± 0.28
184	3.42 ± 0.04	2.11 ± 0.03

The results showed that the diffusion coefficient was affected by the liquid flow rate at low flow rates, but the effect decreased at higher flow rates. In a classic liquid film model,[49] this phenomenon is considered a result of the shrinking diffusion boundary layer in laminar flows as the flow rate increases. As demonstrated in Figure 3.8, the apparent diffusion resistance across the hollow fiber membrane($\frac{L}{D_{app}}$) consists of resistance across the membrane ($\frac{L}{D_{membrane}}$) and across a diffusion boundary layer on the membrane ($\frac{1}{k}$) (Equation 3.15), where *L* is the thickness

of membrane, D_{app} is the apparent diffusivity, $D_{membrane}$ is the diffusivity in the membrane, and k is the mass transfer coefficient, which is affected by the liquid velocity. At low liquid flow rates, the mass transfer coefficient is small, and the diffusion boundary layer is rate limiting. However, as the flow rate is raised, the diffusion boundary layer becomes thinner, causing mass transfer coefficient k to increase and eventually ceasing to limit the overall rate of diffusion.

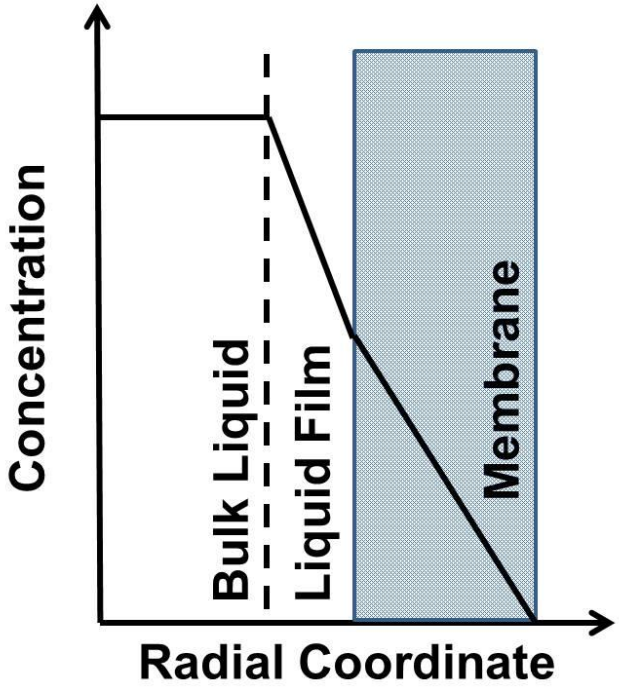

$$\frac{\delta}{D_{app}} = \frac{1}{k} + \frac{\delta}{D_m}$$

Figure 3.8 The apparent diffusion resistance across the hollow fiber membrane consists of resistance of the membrane ($\frac{\delta}{D_{membrane}}$, δ is the thickness of membrane and $D_{membrane}$ is the diffusivity in the membrane) and a liquid film on the membrane inner surface (the reciprocal of mass transfer coefficient k). The liquid film gets thinner as the liquid flow rate rises, and its resistance to diffusion becomes insignificant at very high flow rates.

The impact of liquid flow rate on diffusion resistance across the diffusion boundary layer can be described by an empirical correlation of Sherwood number (Sh) and Reynolds number (Re) for laminar flow in a pipe[49] (Equation 3.163.18), where δ is the membrane thickness; D is

the solute diffusivity in water; ρ is the density of fluid; d is the diameter of fiber; L is the fiber length and v is the fluid velocity. Given this correlation and the measured diffusion coefficients at various flow rates, the membrane diffusivity can be extracted by fitting experimental data to Equation 3.15. The dashed lines in Figure 3.9-Figure 3.11 represent the simulation results, which show a similar trend as found in experimental results. The membrane diffusivity of O_2, CO_2, and IBT obtained are summarized in Table 3.6.

$$\frac{\delta}{D_{app}} = \frac{\delta}{D_{membrane}} + \frac{1}{k} \quad 3.15$$

$$Sh = \frac{kd}{D} = 1.62 Re^{\frac{1}{3}} Sc^{\frac{1}{3}} \left(\frac{d}{L}\right)^{\frac{1}{3}} = 1.62 \left(\frac{d^2 v}{LD}\right)^{\frac{1}{3}} \quad 3.16$$

$$Re = \frac{\rho d v}{\mu} \quad 3.17$$

$$Sc = \frac{\mu}{\rho D} \quad 3.18$$

Table 3.6 Summary of membrane diffusivities of O_2, CO_2 and IBT obtained from film theory fitting using simplistic and rigorous calculation results, compared to their aqueous diffusivities.

Solute	**$D_{membrane}$ ($\times 10^{-10}$ m^2/s) (simplistic calculation)**	**$D_{membrane}$ ($\times 10^{-10}$ m^2/s) (rigorous calculation)**	**$D_{aqueous}$ ($\times 10^{-10}$ m^2/s)**
O_2	24.3	8.56	21.0[49]
CO_2	5.60	4.77	19.2[49]
IBT	2.44	1.68	8.40[73]

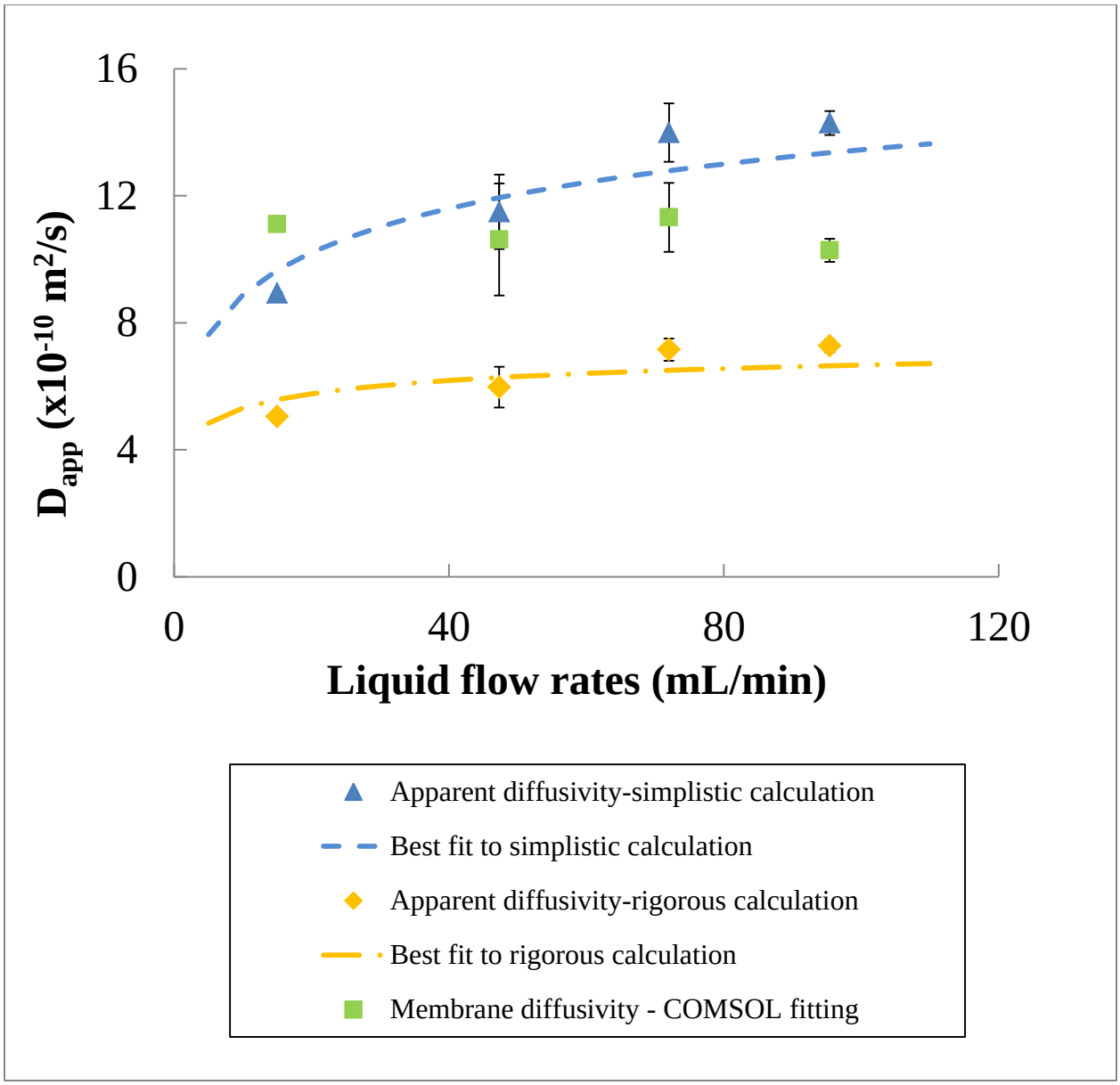

Figure 3.9 Calculated apparent diffusion coefficients of O_2 at different liquid flow rates with simulated correlation between apparent diffusion coefficients and liquid flow rates.

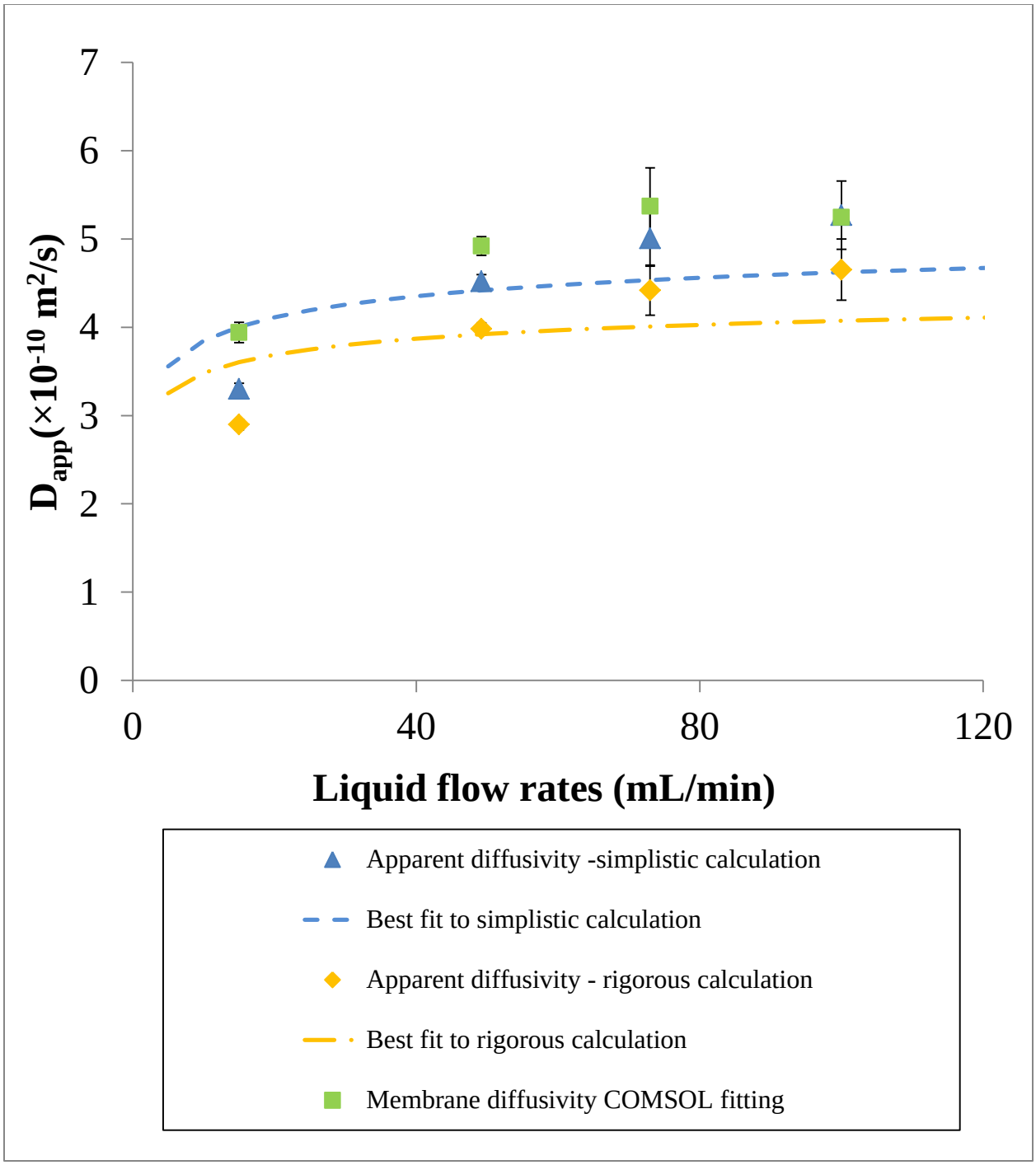

Figure 3.10 Calculated apparent diffusion coefficients of CO_2 at different liquid flow rates with simulated correlation between apparent diffusion coefficients and liquid flow rates.

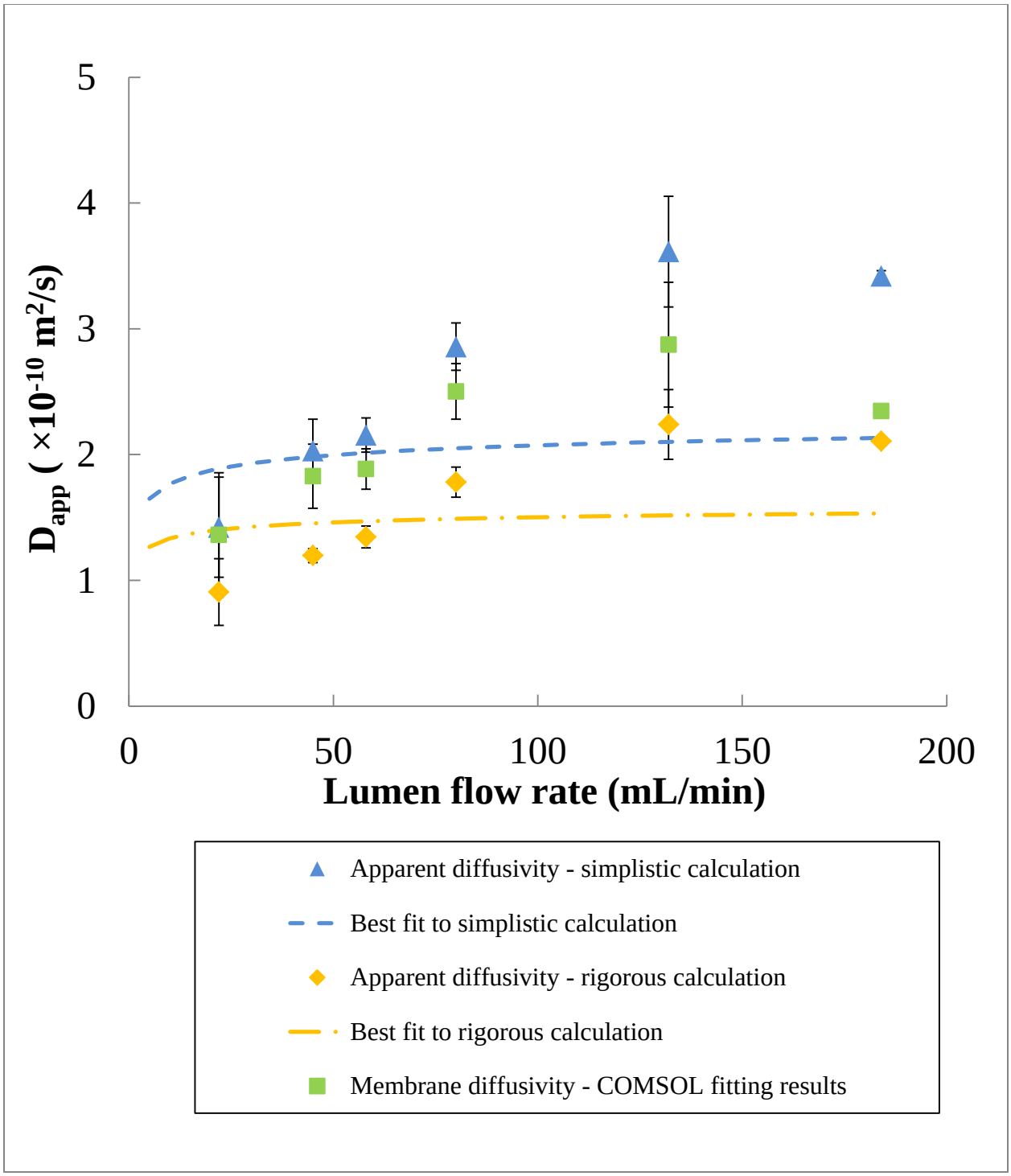

Figure 3.11 Calculated apparent diffusion coefficients of IBT at different liquid flow rates with simulated correlation between apparent diffusion coefficients and liquid flow rates.

3.5 Discussion

3.5.1 Effect of Membrane Type

O_2 diffusion coefficient measurements were carried out with both mixed cellulose ester membrane and XM-50 hollow fiber membrane to verify whether the difference between the two membrane types would result in significant variation in membrane diffusivity. As shown in Table 3.7, the calculated membrane diffusivities are roughly 50% to 90% higher in XM-50 membrane than in mixed cellulose ester membrane. Part of the increase is due to a higher lumen velocity used in the measurement.

Table 3.7 Comparison of D_{app} measured in mixed cellulose ester membrane and XM-50 hollow fiber membrane

Membrane type	**Lumen flow velocity (cm/s)**	$\boldsymbol{D_{app}}$ **(simplistic)** **(× 10^{-10} m^2/s)**	$\boldsymbol{D_{app}}$ **(rigorous)** **(× 10^{-10} m^2/s)**
Mixed cellulose ester, pore size 0.2μm	2.3	8.93	5.05
XM-50, MWCO 50 kDa	3.1	13.5	9.75

3.5.2 Effect of Simplifying Assumptions

The deviations between diffusion coefficient results from the three approaches can be interpreted in terms of the underlying assumptions/simplifications. As summarized in Table 3.8, simplifications were made on four variables: membrane curvature, axial gradient, lumen radial gradient and dead volume.

3.5.2.1 Membrane Curvature

Neglecting membrane curvature could lead to either overestimated or underestimated apparent diffusion coefficient, depending on the membrane surface area used in calculation. In a

curved membrane, at pseudo steady state, the concentration gradient would be highest at the membrane inner surface, where the area normal to diffusion flux is at the smallest, as indicated in Figure 3.12.

For O_2 and IBT, the solute diffuses from the lumen to the shell, and the simplistic calculations were carried out on the basis of membrane inner surface. While the simplistic calculation neglected the membrane curvature and assumed a linear concentration profile within the membrane, in actuality the profile is curved to achieve a constant total flux through the thickness of membrane: as the solute diffuses outward, the area normal to the diffusive flux increases, and correspondingly the concentration gradient decreases. Therefore, simply using the concentration difference divided by the membrane thickness causes the concentration gradient at the inner surface to be underestimated, and hence the diffusion coefficient overestimated. The curvature would cause a similar effect with CO_2, when the solute diffuses from shell side to lumen, but to an opposite effect---the apparent diffusion coefficient is underestimated.

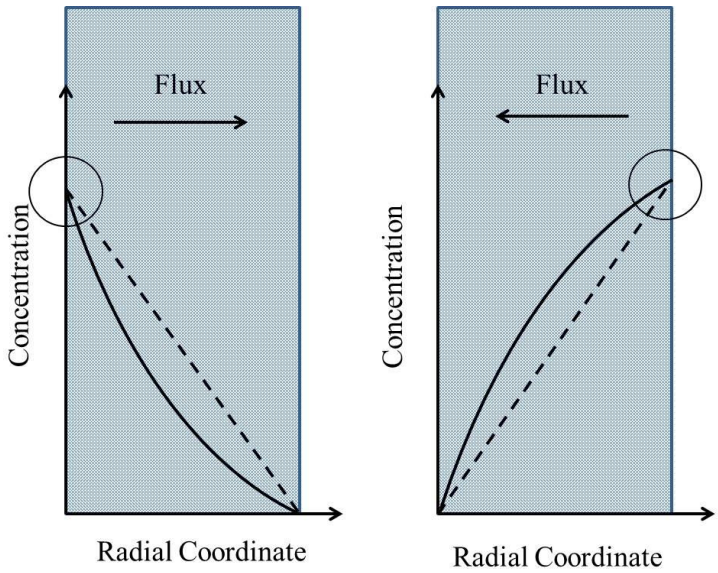

Figure 3.12 Effect of neglecting membrane curvature. For diffusion from lumen to shell (left), if using inner membrane area as basis for calculation, the concentration gradient will be underestimated, causing diffusion coefficients to be overestimated. The opposite occurs with diffusion from shell side to lumen when using outer membrane area for calculation.

3.5.2.2 Axial Gradient and Dead Volume

In this analysis, dead volume refers to the volume outside of the reservoir. The effect of neglecting axial gradient and dead volume is somewhat convoluted since when assuming no dead volume (the entire system is well mixed) and including the entire system volume in the calculation, axial gradient is implicitly omitted. Intuitively, including the dead volume will result in a higher apparent diffusion coefficient than only considering reservoir volume.

On the other hand, neglecting the axial gradient means assuming that the liquid concentration remains at the same level as in the liquid reservoir as the flow travels down the reactor length. However the assumption deviates further because for lower flow rates the longer residence time causes a significant drop in concentration along the reactor length. Still applying the reservoir concentration unrealistically overestimates the concentration driving force across the membrane and therefore the resulting diffusion coefficient is likely to be lower than the actual value.

3.5.2.3 Lumen Radial Gradient

In laminar flow, a concentration gradient exists between the center of the lumen liquid and inner surface of membrane due to the parabolic velocity profile. Neglecting this concentration difference would cause a similar effect as omitting axial gradient—underestimated diffusion coefficient.

The effects of the simplifications, as summarized in Table 3.8, can be used to explain the deviations of simplistic and rigorous calculation results from COMSOL simulation results:

1) Since the rigorous calculation omitted lumen radial gradient, its results were smaller than COMSOL simulation results. However, as the flow rate increases, the diffusion resistance in the model liquid film decreases, thus reducing the error.

2) The simplistic calculation resulted in higher D_{app} in the case of IBT and O_2, indicating that the effects of curvature and dead volume combined were significant enough to overwhelm that of axial gradient. However, as the flow rate increases, the effect of axial gradient becomes weaker, and therefore the simplistic calculation results deviate further from COMSOL results.
3) Since the effect of membrane curvature is reversed in the case of CO_2 diffusion, the simplistic calculation underestimated D_{app}.
4) In O_2 diffusion coefficient measurements, since the reservoir used is very small (16 mL), the error caused by including dead volume (12 mL) in the calculation was large enough that the calculated D_{app} was higher than aqueous diffusivity.

Table 3.8 Effects of simplifying assumptions on apparent diffusion coefficients

Simplification	Effect on calculated D_{app}	Simplistic calculation	Rigorous calculation	COMSOL
No membrane curvature	O_2 and IBT: overestimation CO_2: underestimation	√		
No axial gradient	Underestimation	√		
No dead volume	Possible overestimation	√		
No lumen radial gradient	Underestimation	√	√	

3.5.2.4 Effect of Pressure Fluctuation

The COMSOL simulation accounts for the effect of lumen radial gradient and the results should not be affected by the lumen flow rates. However, an effect is still observed in the case of CO_2 and IBT (Figure 3.10 and Figure 3.11, respectively), where the membrane diffusivity seems to increase with liquid flow rates. On the contrary, such effect is not observed with O_2

measurements (Figure 3.9). This effect is likely a result of convective flow as a result of pressure fluctuations caused by peristaltic pumps. Pressure pulsation is known to enhance mass transfer in membrane processes by way of enhancing dispersion and permeation.[74-77] The pressure fluctuation caused by peristaltic pumps increased in frequency as higher flow rates are delivered by the pump head thus causing an apparent increase in membrane diffusivity.

Larger diameter tubing (3/16'' I.D.) was used in IBT and CO_2 setups than for O_2 setup (1/16'' ID). All of the tubing had the same wall thickness (1/16''). Since the pressure fluctuations caused by peristaltic pumps stem from the deformation of tubing, with the same wall thickness, it is speculated that tubings with larger diameters would likely result in more prominent pressure fluctuations.

In conclusion, the diffusion coefficients of O_2, CO_2 and IBT were measured in hollow fiber membranes Experimental data were analyzed to obtain a value for the diffusivity using three methods. The values obtained using COMSOL simulations are considered to be the most accurate results, because the COMSOL simulations most accurately capture the effect of a laminar flow velocity profile on the concentration driving force for mass transfer. Due to the pressure fluctuation caused by peristaltic pumps, the diffusion coefficients obtained from COMSOL simulations are likely higher than the actual membrane diffusivity.

4 SIMULATION OF ISOBUTANOL PRODUCTION IN A BIOREACTOR FOR INCOMPATIBLE GASES (BIG)

4.1 Introduction

The BIG system described in Chapter 2 addresses the engineering challenges associated with aerobic fermentations with sparingly soluble flammable gases, such as H_2. The biocatalyst was immobilized in the porous walls of the hollow fibers, with O_2 and H_2 provided from opposite sides of the membrane wall. The BIG system is the first bioreactor that allows independent, enhanced mass transfer of O_2 and H_2 without creating hazardous gas-phase mixtures of an energy-rich gas and oxygen. This novel design de-risks fermentations with incompatible gases and may lead to an economically viable electrofuel platform. The BIG system could also be applied in methanotrophic fermentations.

During the BIG experiments, unexpected trends in IBT production levels were observed, including an initial spike in IBT concentration that subsequently disappeared, very low IBT production despite high cell densities, and little effect of increased substrate availability on reactor performance.

To help explain these results, it was hypothesized that under H_2-limiting conditions IBT was consumed by the *R. eutropha* cells as a carbon and/or energy source. Several of the experimental trends were consistent with this hypothesis. However, due to the novelty of the BIG design, very little literature exists to discuss the interaction between the reaction kinetics and mass transfer in a system configuration where substrates diffuse from opposite sides of the reaction site, changes in mass-transfer across the hollow-fiber wall due to cell growth, and product formation in one part of the reactor accompanied by consumption in another part. To validate the hypothesis and better understand the effects of operating conditions on IBT

production and obtain insights for future scale up of the bioreactor, a comprehensive, dynamic mathematical model was constructed to describe both mass transfer and cellular kinetics in BIG. The resulting partial differential equations were solved using COMSOL® Multiphysics, and the results were used to explore the system dynamics under various conditions. Results presented in this chapter explored the effect of cell density and H_2 and ammonium availability on IBT production.

4.2 Materials and Methods

4.2.1 Model Setup

The model was constructed to describe the conditions of the immobilized cells experiments with flow-through configuration on the shell side. A single hollow fiber within the reactor was described in cylindrical coordinates with 3 domains: lumen, membrane and shell. The hollow fiber membrane has an inner radius of 0.57 mm, an outer radius of 0.9 mm with a length of 42.5 cm. The lumen flow rates ranged between 160 mL/min and 800 mL/min, which correspond to a Reynolds number between 48 and 240. The laminar flow in the lumen was described with a parabolic velocity profile. Since the cross section of the reactor shell had a highly irregular shape, the high velocity shell gas flow (0.5 L/min) was assumed to be turbulent and have a uniform concentration. With immobilized cells, convection was considered negligible in the membrane domain. Equation 3.6 was used to describe the diffusive and convective mass transfer in lumen and shell space, and Equation 3.7 was used to describe the diffusion and biocatalytic reactions.

$$\frac{\partial C_i}{\partial t} + \nabla \cdot (-D_i \nabla C_i) + u \cdot \nabla C_i = 0 \quad (4.1)$$

$$\frac{\partial C_i}{\partial t} + \nabla \cdot (-D_i \nabla C_i) = r_i \quad (4.2)$$

In Equations 3.6 and 3.7, C_i is the concentration of a chemical species with diffusion coefficient D_i and membrane reaction rate r_i. The flow velocity in either lumen or shell is represented by u. The concentrations of all chemical species at the lumen-membrane interface are assumed to be continuous. Instantaneous gas-liquid equilibria are assumed for gaseous substrates and volatile chemical species, such as IBT, at the membrane-shell interface.

In the experiments, the BIG system was operated with liquid circulating from a reservoir, where the dissolved O_2 (DO) level was monitored and regulated, and CO_2 and O_2 flow rates were set at a fixed ratio. Therefore, it was assumed in the simulations that O_2 and CO_2 concentrations at the hollow fiber lumen inlet were fixed at 100% saturation and 20% saturation, respectively. In contrast, inlet IBT and ammonium concentrations were equal to their reservoir concentrations, which were dependent on the outlet concentrations and the liquid flow rate. Ordinary differential equations (Equation 3.8) were included in the model to update the IBT and ammonium reservoir concentrations, where V_R is the reservoir volume, $C_{i,reservoir}$ is the concentration in the reservoir, $C_{i,outlet}$ is the average concentration at the hollow fiber outlet, and F is the lumen flow rate.

$$V_R \frac{dC_{i,reservoir}}{dt} = F_L(C_{i,outlet} - C_{i,reservoir}) \quad 4.3$$

The modeling equations were solved using COMSOL Multiphysics®, which uses finite element methods to solve for the coupled differential equations that describe the spatial profiles and transient behaviors of the eight variables, including concentrations of substrates, products and cells in the 3 domains. The model was used to help interpret experimental results, identify rate-limiting steps, and optimize system performance, and it may also be suitable to help design and scale up practical BIG reactors for IBT production.

4.2.2 Mass Transfer Parameters in the Hollow Fiber Membrane

The membrane diffusivities of O_2, CO_2 and IBT were measured experimentally. The system setups (Figure 4.1) were designed so that the driving force for diffusion only depends on the reservoir concentration, and the natural log of the concentration changes linearly with respect to time. The experimental procedures and data analysis are detailed in Chapter 3.

Due to the low Reynolds number of the lumen flow, the parabolic profile of the liquid was taken into account in determining the diffusivities. Simulations were done using COMSOL Multiphysics to fit the experimental results and obtain the membrane diffusivities D_M, as summarized in Figure 4.1. Since the membrane diffusivities vary slightly with flow rate due to pressure fluctuations caused by peristaltic pumps,[74-76] the average value was used as the membrane diffusivity.

Table 4.1 Mass transfer parameters used in simulations.

Parameter	Value ($\times 10^{-10}$ m^2/s)	Parameter	Value ($\times 10^{-10}$ m^2/s)	Parameter	Value (mL/min)
D_{O_2}	21.0[49]	D_{M,O_2}	11.2	F_{Lumen}	160
D_{H_2}	45.0[49]	D_{M,H_2}	19.5	F_{Shell}	500
D_{CO_2}	19.2[49]	D_{M,CO_2}	4.87		
$D_{NH_4^+}$	19.6[49]	D_{M,NH_4^+}	6.70		
D_{IBT}	8.40[73]	$D_{M,IBT}$	2.13		

The highest cell density reached at the peak in the simulation is 50 g/L. As reviewed by Stewart,[70] the reported diffusivities of solutes, such as glucose, acetate and O_2, ranged between 30% and 45% of the corresponding value in water in biofilms with cell densities around 50 g/L. Therefore, for the other chemical species (H_2 and ammonium), the membrane diffusivities were conservatively assumed to be 35% of their aqueous diffusivities. Also, cell density is assumed to

have no effect on the membrane diffusivities of O_2, CO_2 and IBT. A list of mass transfer parameters used in the model is summarized in Table 4.1.

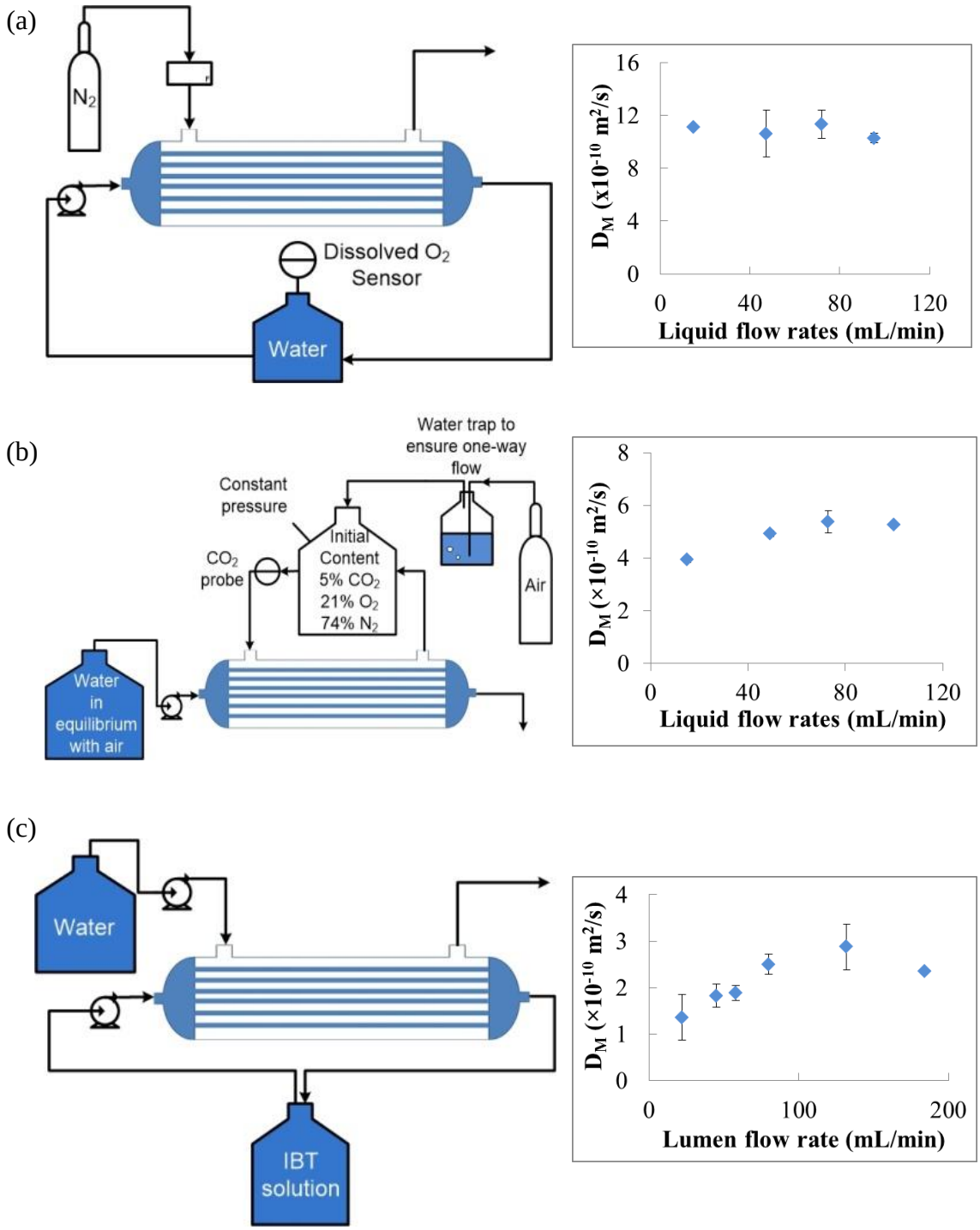

Figure 4.1 Experimental setups and results for measuring the membrane diffusivities of: (a) O_2, (b) CO_2, and (c) IBT

4.2.3 Estimation of Stoichiometry

Ralstonia eutropha is a facultatively autotrophic gram-negative bacterium that can use H_2 as an energy source to reduce CO_2 in the presence of O_2.[29, 78] The first part of the autotrophic pathway used by *R. eutropha* involves fixation of CO_2 and production of glyceraldehyde-3-phosphate (G3P) via the Calvin-Benson-Bassham (CBB) cycle. These reactions consume reducing equivalents (electrons) in the form of NADPH and energy in the form of ATP.[79] The subsequent reduction of G3P to IBT also consumes NADH, NADPH and ATP. To generate the electrons and ATP, *R. eutropha* uses a soluble hydrogenase (SH) that oxidizes H_2 while reducing NAD^+ to NADH.[4] It also uses a membrane-bound hydrogenase (MBH) to remove electrons from H_2 and direct them into an electron transport chain, which pumps protons across a membrane against a concentration gradient. The resulting "proton motive force" drives the protons back across the membrane in a process that generates ATP. Finally, the protons are recombined with the electrons and the terminal electron acceptor (O_2) to make water.[80] *R. eutropha* also has a transhydrogenase (TH) that converts NADH produced by the SH to NADPH, which is needed for CO_2 fixation via the CBB cycle.[81]

The stoichiometry for cell growth and IBT production can be estimated by combining the following reactions: (a) reduction of CO_2 to G3P using NADPH and ATP in the CBB cycle, (b) MBH-catalyzed H_2 oxidation and subsequent ATP production via the electron transport chain, (c) conversion of G3P to PYR via enzymatic reactions found in glycolysis, (d) conversion of NADPH to NADH, (e) conversion of PYR to IBT or cell mass, whose elemental composition can be approximated as $CH_{1.8}O_{0.5}N_{0.2}$,[82] and (f) SH-catalyzed reduction of NAD^+ to NADH by H_2. The final stoichiometry is affected by $Y_{P/O}$, the number of ATP molecules generated in the electron-transport chain by per molecule of O_2 consumed, which could range between 0.5 and 4

depending on the experimental conditions.[79] Assuming a $Y_{P/O}$ of 2.3, the reactions for cell growth and IBT productions were estimated as follows:

$$4CO_2 + 36H_2 + 12O_2 \rightarrow C_4H_{10}O + 31H_2O \quad 4.4$$

$$6CO_2 + 18.6O_2 + 50H_2 + 1.2NH_3 \rightarrow 6CH_{1.8}O_{0.5}N_{0.2} + 46.2\,H_2O \quad 4.5$$

The metabolic pathways for IBT consumption by the cells, either for anabolism (formation of cell mass) or catabolism (energy generation) are still unclear, but using energy and material balances, the stoichiometry for cell growth on IBT was estimated based on yield coefficient obtained experimentally (Equation 4.6), and the stoichiometry for IBT catabolism (Equation 4.7) was assumed to be the same as that of IBT aerobic combustion:

$$C_4H_{10}O + 4.52\,O_2 + 0.282\,NH_3 \rightarrow 1.41\,CH_{1.8}O_{0.5}N_{0.2} + 2.59\,CO_2 + 4.16\,H_2O \quad 4.6$$

$$C_4H_{10}O + 6\,O_2 \rightarrow 4\,CO_2 + 5\,H_2O \quad 4.7$$

4.2.4 Structured Cellular Kinetic

There are two types of kinetic models for microbial biocatalysts: unstructured and structured. Unstructured models assume that the cell mass is invariant in its properties, whereas structured models account for time-dependent changes in cellular composition and reactivity. For example, the commonly used unstructured Monod model[83] describes the effect of substrate concentration on microbial growth rate, but it cannot describe bacterial cells' adjustment to changes in growth conditions,[84] such as lag phases or transition between heterotrophic and autotrophic growth. Structured models are able to describe more complex cell behaviors by dividing biomass into compartments[85] and/or incorporating physiological variables such as intracellular concentration of RNA.[86] By recognizing the changes in physiological state of cells, structured models are able to more accurately describe various behaviors in cell growth and product formation. Because *R. eutropha* exhibits dramatic changes in its metabolism based on

changes in the nitrogen/carbon ratio, and because the immobilized cells are expected to exhibit variations in metabolic activity due to substrate gradient in the biofilm, a structured model was developed for growth and IBT production by *R. eutropha* in the bioreactor.

A number of structured kinetic models have been constructed for poly-β-hydroxybutyrate (PHB) production in wild type strains of *R. eutropha*. PHB is a biodegradable polymer and can accumulate up to 80% of cell dry weight.[87, 88] Given the high contents of product in cells, most of the models segregate the product (P) from the rest of biomass, which is denoted "rest mass" (R). However, the engineered IBT-producing strain differs from the PHB-producing wild type in that, instead of remaining part of the cell, the product IBT is secreted out of the cell membrane. However, IBT production is dependent on the cells' viability, which is described by Hills and Wright [89] by introducing the total biomass per cell (s^*) and defining a minimum cell weight (s_{min}) below which the cell is no longer considered viable. Since a typical bacterial culture contains around 10^{12} cells·L^{-1}·OD^{-1},[90] and a robust autotrophic culture of wild type *R. eutropha* H16 contains 0.383 g DCW L^{-1}·OD^{-1}, s_{min} was assumed to be 0.3×10^{-12} g/cell. The "excess cell mass" s is the difference between the minimum cell weight (s_{min}) and total cell mass (s^*) and contains the enzymatic components responsible for product synthesis, indicating the cell's metabolic activity. Only when excess cell mass is present does the cell reproduce (increase in cell number N) and synthesize the product. The structured model is described in Equations 4.8-4.10, where μ and μ_{IBT} are specific growth rates on autotrophic substrates and IBT; k_n and $k_{n,ibt}$ are specific cell division rates on autotrophic substrates and IBT, respectively; and k_s and k_d represents cell mass and cell number degradation constants, respectively.

$$M = Ns^* = N(s_{min} + s) \qquad 4.8$$

$$\frac{dM}{dt} = \mu M + \mu_{IBT} M - k_s s N \quad (4.9)$$

$$\frac{dN}{dt} = k_n s N + k_{n,ibt} s N - k_d N \quad (4.10)$$

4.2.5 Mixed Substrate Cell Kinetics

Bacterial consumption of mixed substrates could be either sequential (diauxic growth) or simultaneous (mixotrophic). It was assumed that the cells utilize IBT and H_2 as energy and carbon sources simultaneously. Several models have been proposed for mixotrophic growth, and, as reviewed by Kovárová-Kovar and Egli [91] most of them were modified from Monod-type saturation kinetics. One of the models[92] defines the mixotrophic specific growth rate to be the function of Monod parameters from single-substrate growth and the percentage of each substrate in the mixture. This model yielded the best fit for *E. coli* growth on multiple substrates, and therefore its form was adopted in the kinetic model to account for the mix substrate growth.

$$\mu = \mu_{max}\left(\frac{\alpha C_{H_2}}{\alpha C_{H_2}+(1-\alpha)C_{IBT}}\right)\left(\frac{C_{CO_2}}{C_{CO_2}+K_C}\bullet\frac{C_{H_2}}{C_{H_2}+K_H}\bullet\frac{C_{O_2}}{C_{O_2}+K_O}\bullet\frac{C_{NH_3}}{C_{NH_3}+K_N}\right)\left(1-\frac{C_{IBT}}{C_{IBT,max}}\right) \quad (4.11)$$

$$k_n = k_{n,max}\left(\frac{\alpha C_{H_2}}{\alpha C_{H_2}+(1-\alpha)C_{IBT}}\right)\left(\frac{C_{CO_2}}{C_{CO_2}+K_C}\bullet\frac{C_{H_2}}{C_{H_2}+K_H}\bullet\frac{C_{O_2}}{C_{O_2}+K_O}\bullet\frac{C_{NH_3}}{C_{NH_3}+K_N}\right)\left(1-\frac{C_{IBT}}{C_{IBT,max}}\right) \quad (4.12)$$

$$\mu_{IBT} = \mu_{max,IBT} M\left(\frac{(1-\alpha)C_{IBT}}{\alpha C_{H_2}+(1-\alpha)C_{IBT}}\right)\left(\frac{C_{IBT}}{C_{IBT}+K_{IBT}}\bullet\frac{C_{O_2}}{C_{O_2}+K_O}\bullet\frac{C_{NH_3}}{C_{NH_3}+K_N}\right)\left(1-\frac{C_{IBT}}{C_{IBT,max}}\right) \quad (4.13)$$

$$k_{n,IBT} = k_{n,max,IBT}\left(\frac{(1-\alpha)C_{IBT}}{\alpha C_{H_2}+(1-\alpha)C_{IBT}}\right)\left(\frac{C_{IBT}}{C_{IBT}+K_{IBT}}\bullet\frac{C_{O_2}}{C_{O_2}+K_O}\bullet\frac{C_{NH_3}}{C_{NH_3}+K_N}\right)\left(1-\frac{C_{IBT}}{C_{IBT,max}}\right) \quad (4.14)$$

$$r_M = \mu M + \mu_{IBT} M - k_s s N \quad (4.15)$$

$$r_N = k_n s N + k_{n,ibt} s N - k_d N \quad (4.16)$$

$$r_s = [1+s]\left[\mu - k_n s + \mu_{IBT} - k_{n,ibt} s + k_d\right] - k_s s \quad (4.17)$$

$$r_{IBT} = k_{IBT} sN \left(\frac{C_{CO_2}}{C_{CO_2}+K_C} \bullet \frac{C_{H_2}}{C_{H_2}+K_H} \bullet \frac{C_{O_2}}{C_{O_2}+K_O}\right)\left(1-\frac{C_{IBT}}{C_{IBT,max}}\right) - Y_{IBT/cell}\mu_{IBT}M - \left(\frac{(1-\alpha)C_{IBT}}{\alpha C_{H_2}+(1-\alpha)C_{IBT}}\right) k_{d,IBT} M \left(\frac{C_{IBT}}{C_{IBT}+K_{IBT}} \cdot \frac{C_{O_2}}{C_{O_2}+K_O}\right)\left(1-\frac{C_{IBT}}{C_{IBT,max}}\right) \quad 4.18$$

The kinetic model is described in Equation 4.11-4.18, where M is cell mass density, N is cell number density, and s is excess cell mass. $C_{H_2}, C_{CO_2}, C_{O_2}, C_{NH_3}$ are concentrations of H_2, CO_2, O_2 and NH_4^+; K_H, K_C, K_O, K_N are the corresponding Monod constants; $C_{IBT,max}$ is the IBT concentration above which the strain no longer grows; μ_{max} and $\mu_{max,IBT}$ are the maximum specific autotrophic growth rate and maximum specific growth rate on IBT respectively; $k_{n,max}$ and $k_{n,max,IBT}$ represent the maximum specific cell division rates using CO_2 and IBT as the only carbon source. The strain's relative preference to use H_2 as energy source is represented with α, with α=0 meaning the strain does not utilize H_2 at all and α=1 meaning the strain only utilizes H_2. The immobilized cells grow both autotrophically on H_2, CO_2, and O_2 and heterotrophically on IBT in the presence of nitrogen source, such as NH_4Cl. Since H_2 is most likely the limiting substrate in autotrophic growth (Table 2.1), the contributions of growth on autotrophic substrates and IBT in mixotrophic metabolism are assumed to be determined by the local ratio of H_2 and IBT concentrations. Growth on H_2 and IBT are both inhibited by IBT in a linear form $\left(1-\frac{C_{IBT}}{C_{IBT,max}}\right)$. IBT is also catabolized by the cells in the presence of O_2.

4.2.6 Estimation of Kinetic Parameters

Some of the kinetic parameters were estimated from experimental data. The maximum specific growth rate of *R. eutropha* on autotrophic substrates was estimated to be 0.065 ± 0.017 h-1, and since the autotrophic growth rate was likely affected by substrate limitations, μ_{max} is

assumed to be 0.11 h-1 in the simulations, which is a conservative estimation compared to the literature value of 0.29 h-1.[93]

The specific growth rate of *R. eutropha* on IBT ($\mu_{max,IBT}$) and the corresponding yield coefficient were estimated based on data from IBT-consumption experiments (2.3.3). The maximum specific growth rate on IBT was 0.033 h-1 with a yield of 2.13 g IBT/g DCW cell. The highest IBT consumption measured was 62 mg IBT/ (g DCW cell·h). IBT is known to be toxic towards *R. eutropha* cells, and concentrations above 1% v/v (0.12 mol/L) results in no cell growth,[33] and therefore $C_{IBT,max}$ is set to be 0.12 mol/L.

The specific IBT production rate was estimated to be 1.22 mg/ (g DCW h). If the maximum specific growth rate was used as a reference point for the carbon flux capacity of the engineered strain's metabolic pathways, the maximum IBT specific growth rate k_{IBT} would be $\mu_{max} \cdot Y_{cm}/Y_{c\_ibt}$, with Y_{cm} being the yield coefficient from CO2 to cell mass, and Y_{c_ibt} being the yield coefficient from CO2 to IBT. Based on the estimated stoichiometries in Equations 4.4 and 4.5, Y_{cm}=1.8, and Y_{c_ibt}=2.4, and therefore $k_{IBT} = \mu_{max} \cdot Y_{cm}/Y_{c\_ibt}$=0.0825 g/(g DCW h). In the model, however, a more ambitious value for k_{IBT} (0.25 g/ (g DCW h)) was assumed to simulate a much improved biocatalyst and assess mass transfer limiting scenarios that would provide valuable guidance in process optimization for the bioreactor system.

It was not feasible to obtain exact values of all the kinetic values based on the limited experimental data obtained. Due to limited quantitative studies on autotrophic growth of *R. eutropha*, very little can be found concerning the other kinetic parameters. Monod constant for ammonium chloride was estimated to be 0.167 mol/L from a paper by Patwardhan and Srivastava.[31] Monod constants for H_2 and O_2, were assumed to be 1×10-6 mol/L based on Monod constants obtained by Siegel and Ollis.[93] Monod constant for CO_2 was assumed to be

the same as that of H_2 and O_2. The maximum specific cell division rate on autotrophic substrates and IBT, $k_{n,max}$ and $k_{n,max,IBT}$, are assumed to be slightly lower than the corresponding maximum specific growth rate, since cell division is likely to occur at a slower pace than cell mass accumulation. Reasonable values were assumed for the rest of the kinetic parameters and are considered sufficient to elucidate trends in the performance properties of the novel BIG reactor. A list of kinetic parameters used in the model is summarized in Table 4.2.

Table 4.2 Kinetic parameters used in simulations.

Parameter	Value	Parameter	Value	Parameter	Value
μ_{max}	0.11 h^{-1}	k_s	0.033 h^{-1}	K_H	1×10^{-6} mol/L[93]
$\mu_{max,IBT}$	0.033 h^{-1}	k_d	1×10^{-14} h^{-1}	K_O	1×10^{-6} mol/L[93]
k_n	0.1 h^{-1}	k_{IBT}	0.25 g/ (g DCW h)	K_C	1×10^{-6} mol/L[93]
$k_{n,IBT}$	0.03 h^{-1}	$k_{d,IBT}$	0.062 h^{-1}	K_{IBT}	1×10^{-3} mol/L
α	0.5	$C_{IBT,max}$	0.12 mol/L	K_N	0.014 mol/L[31]

4.3 Results and Discussion

4.3.1 Evolution of Cell Density and Reaction Profile

Unlike planktonic culture in a continuous stirred tank reactor, in which the cells are uniformly distributed throughout the reactor, the immobilized cells within the BIG do not reach a steady state over the time period of the simulations. Even though the simulations were initiated with a uniform cell density, the profile soon developed a cell concentration peak that grows higher and thinner, as depicted in Figure 4.3. The peak formation is a result of the counter-directional diffusion of H_2 and O_2, as illustrated in Figure 4.4.

H_2 and O_2 diffuse from opposite sides of the membrane, with their concentration profiles overlapping in a finite "reaction zone" within the membrane. Only immobilized cells within the reaction zone are predicted to grow, while cells outside of the reaction zone become deprived of either O_2 (near the shell surface) or H_2 (in the vicinity of lumen surface) and degrade. The higher consumptions of both H_2 and O_2 in the reaction zone cause the concentration gradients to become steeper, resulting in a narrower reaction zone. Without nitrogen limitation, the cell density in the reaction zone continues to grow, and the active immobilized cell layer becomes thinner and more concentrated without reaching a true steady state. However, the total cell mass under the density peak reaches a plateau as the cell density that can be sustained by the maximum H_2 diffusive flux (Figure 4.2). If the simulation were extended indefinitely, a steady state could be reached when the cell density at the peak reached the maximum density allowed in the system. The maximum cell density could be defined as the largest number of cells the porous structures of the membrane could hold. However, as an extremely high cell density would significantly impacts the membrane porosity, the maximum cell density is likely to be restricted by local membrane diffusivities of the substrates and product.

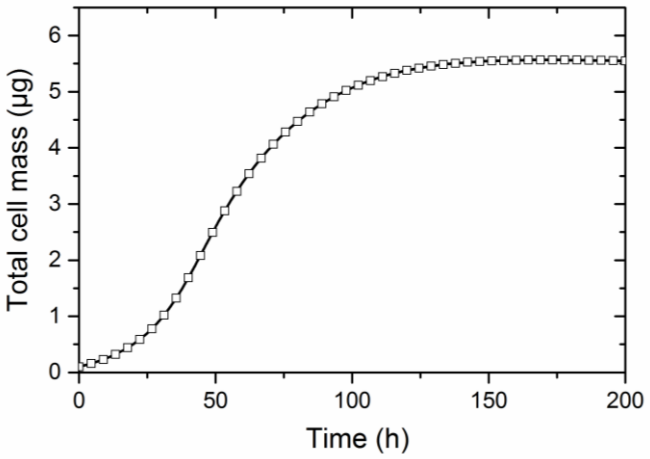

Figure 4.2 The trend for total immobilized cell mass in the BIG resembles the growth curve in a chemostat-exponential growth at low cell density follow by a plateau when mass transfer becomes limiting.

The position of the concentrated cell layer is affected by the relative availability of H_2 and O_2. As O_2 concentration drops along the length of the fiber, the reaction zone shifts closer to the lumen (Figure 4.3). *R. eutropha* are motile and have shown chemotactic activity towards certain nutrients.[12, 94] Random motility would tend to combat sharp cell concentration gradients. However, the pore structures in the hollow fiber walls are relatively rigid and are not likely to allow significant movement. Therefore, the cells' mobility was assumed negligible in the model, and the local cell density is only affected by cell growth and degradation based on local substrate and product concentrations.

In systems with immobilized cells where nutrients diffuse from a single direction, the active cell layer tends to migrate towards the nutrients and, eventually, out of the support material. In contrast, in this hollow fiber system, the active cell layer is well confined within the membrane.

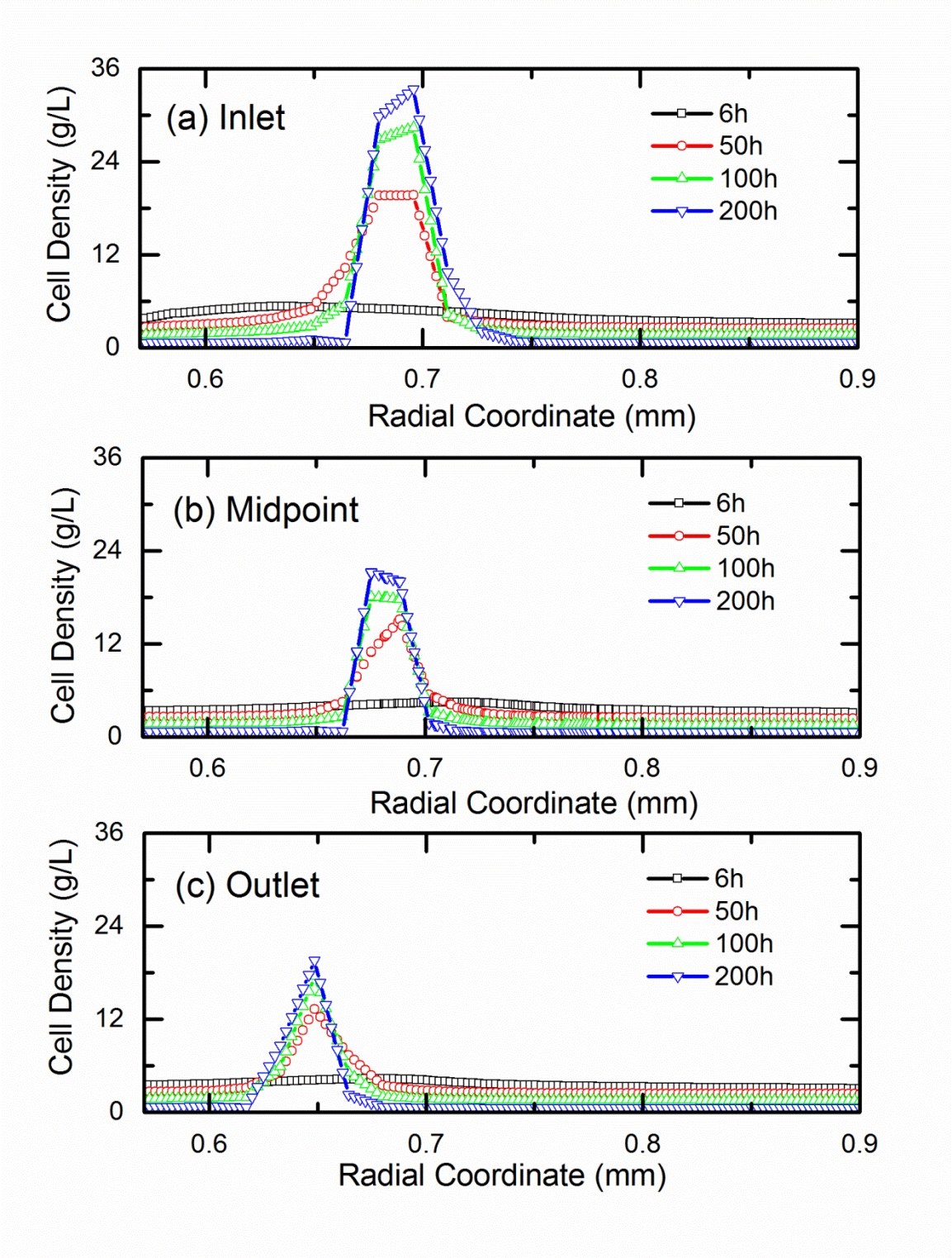

Figure 4.3 Evolution of cell density profile in the membrane at (a) inlet, (b) mid-point and (c) outlet of the hollow fiber reactor.

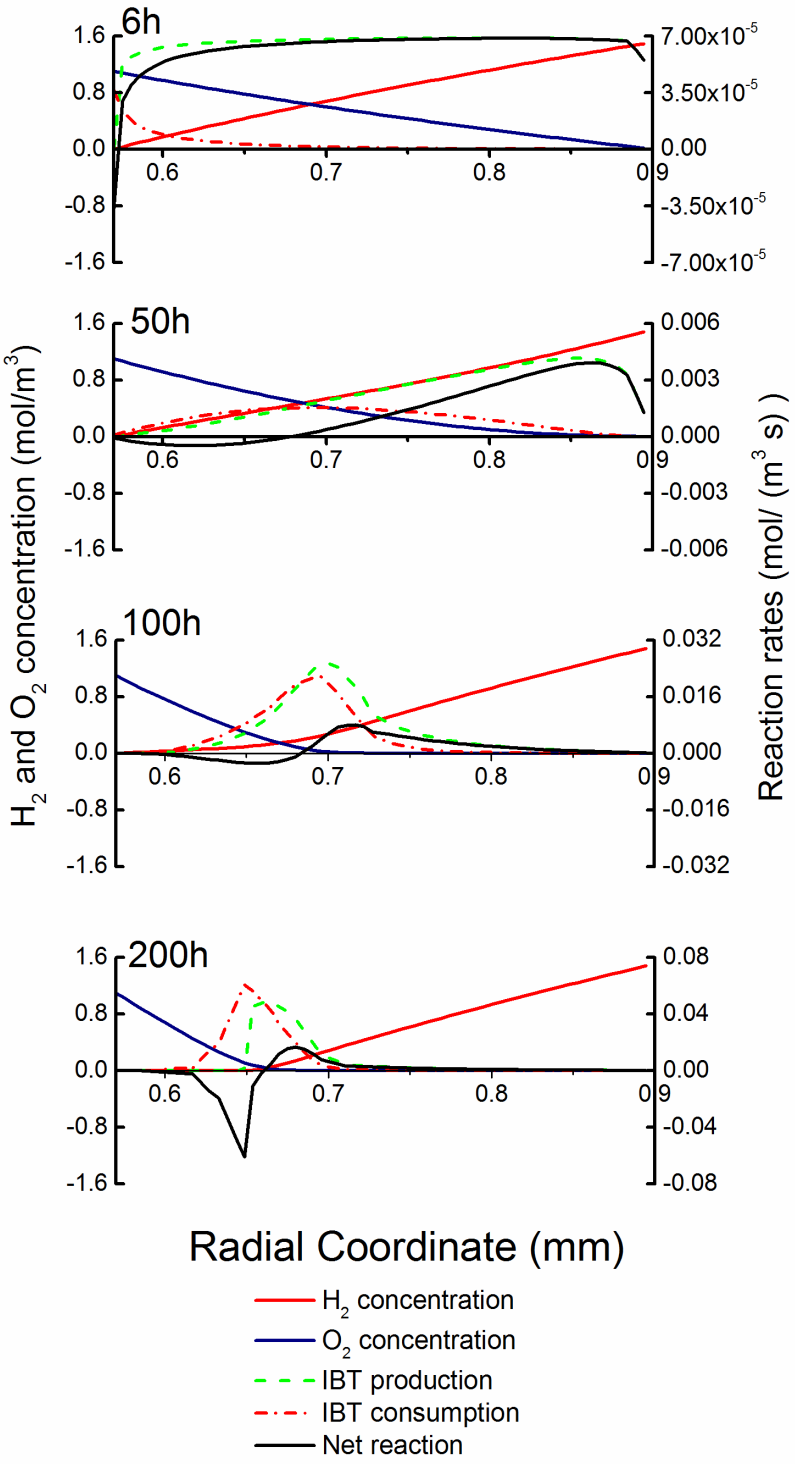

Figure 4.4 The evolution of O_2 and H_2 profiles as well as IBT production, consumption and net reaction rates at membrane inlet in the case with H_2 membrane diffusivity at 1×10^{-9} m^2/s.

Figure 4.4 shows the evolution of IBT production, consumption, and net reaction rates in the cross section of the fiber inlet at a H_2 membrane diffusivity of $1x10^{-9}$ m^2/s. As the cell density increases, the cells at the lumen surface become depleted of O_2 and start to consume IBT (6 h). As the peak in cell density profile develops, it also becomes the point of highest IBT production. However, due to high H_2 consumption, part of this dense cell layer does not receive enough H_2, and therefore a peak for IBT consumption forms next to the IBT production peak. As a result, a positive IBT net production only occurs in radial positions closer to the H_2 source, while IBT consumption (i.e., negative IBT production) is observed at positions farther from the H_2 source. Beyond a certain cell mass, the total IBT consumption by the cells overwhelms the total IBT production, and the IBT concentration decreases. This trend is consistent with our experimental observation that beyond a certain cell density, net IBT production decreases. Thus, the model provides support for the hypothesis that H_2 depletion by the cells triggers IBT consumption.

The general development of immobilized cell density distribution, H_2 and O_2 profile in the membrane and IBT production and consumption rates can be applied to explain the simulation results.

4.3.2 Predicted Effect of Experimental Conditions on IBT Production

4.3.2.1 Initial Cell Density

The model was used to explore the effect of initial cell density on BIG dynamics. The simulated results (Figure 4.5) show an initial increase in IBT concentration as cell concentration increases, followed by a relatively rapid drop in IBT concentration as cell density passes a threshold level. For higher initial cell densities, the rise in IBT concentration to the maximum

value and the onset of the decline in IBT concentration both occur sooner, and the final IBT concentration is lower.

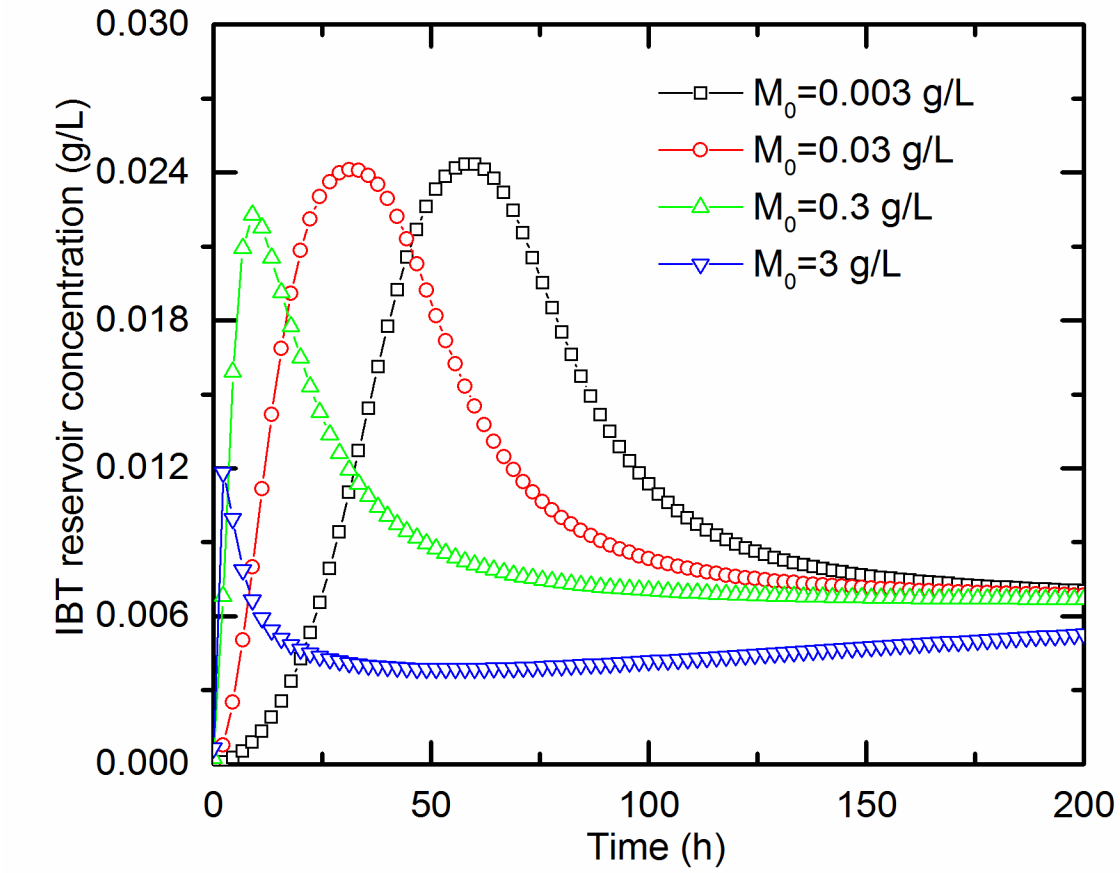

Figure 4.5 IBT concentration versus time at different initial cell densities in a recirculation mode.

As demonstrated in Section 4.3.1, the higher the initial cell density, the sooner H_2 mass transfer becomes rate-limiting and significant net IBT consumption shows effect. While the rate of IBT production is limited by H_2 mass transfer, the rate of IBT consumption is not. The higher the cell concentration, the more rapidly IBT is consumed. Also, in the region where H_2 becomes depleted, IBT production slows, leaving more O_2 available for IBT consumption. At the highest initial cell density (3 g/L), the IBT concentration drops the earliest, before the IBT concentration could reach above 0.012 g/L. These results suggest that with a high enough initial cell density,

no IBT net production would be observed, providing a reasonable explanation for the very low to no IBT production observed during experiments with high immobilized cell concentrations.

4.3.2.2 Effect of Membrane Thickness

Since all the gas substrates are delivered to the immobilized cells via diffusion through the membrane, membrane thickness would be expected to be an important process parameter. Immobilized-cell biocatalysts exhibiting standard Monod kinetics exhibit an optimum biofilm thickness. Biofilms thicker than the optimum are diffusion-limited and biofilms thinner than the optimum could be kinetically limited. IBT consumption further complicates the calculations and data interpretation. With a thicker membrane, more severe H_2 limitation results in more IBT consumption, thereby reducing net IBT production. These trends are evident in Figure 4.6, which shows simulation results for five biofilm thicknesses. The thinnest biofilm simulated gave the highest IBT concentration, although a much longer time was required for the cells to grow to a high enough cell mass within the thin membrane to achieve maximum IBT concentration.

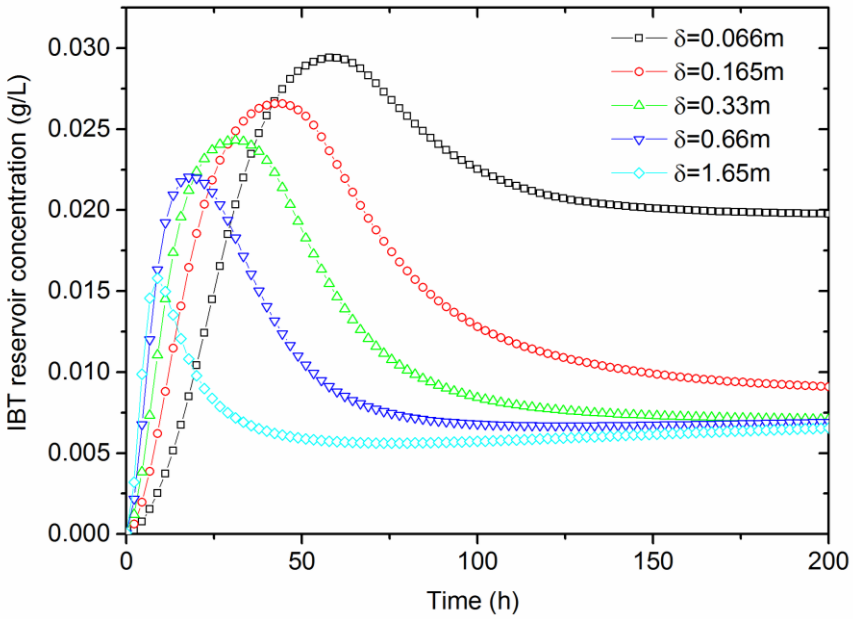

Figure 4.6 IBT concentration at various biofilm thicknesses.

Cell density and membrane thickness both affect the initial total cell mass in the membrane, but they influence IBT production in different ways. Cell density affects the consumption of substrate in a unit volume of the membrane and, as a result, the substrate concentration gradients. Moreover, extreme cell densities would affect the membrane diffusivities of all chemical species. On the other hand, as the overlap between O_2 and H_2 profile becomes thinner, membrane thickness determines the distance the substrates have to diffuse through to reach the active cell layer, which impacts the maximum diffusive flux.

4.3.2.3 Effect of Initial Ammonium Concentration

While the presence of a nitrogen source is essential to maintain cells' metabolic viability and ability to produce IBT, it also encourages cell growth, which diverts resources away from IBT formation. Therefore, BIG's productivity is highly sensitive to ammonium concentration in the lumen liquid.

Figure 4.7 summarizes the simulation results at various initial ammonium concentrations without IBT recovery. Two distinctly different trend lines are predicted. At the 2 highest initial ammonium concentrations, 1 g/L and 5 g/L, the ammonium is not depleted in the 100 hour time frame, allowing cell growth to exceed the threshold cell mass beyond which H_2 depletion occurs and rapid IBT consumption takes place. As a result, the IBT concentration peaks and decays rapidly, as was reported above. On the other hand, for the two lowest ammonium concentrations, 0.01 and 0.1 g/L, the nitrogen source becomes depleted, and cell growth stops at 5.6 h and 12.8 h, respectively. Afterwards the cell densities decrease slowly due to cell degradation, causing the IBT levels to gradually drop. However, because the cell density never achieves levels at which H_2 becomes depleted throughout much of the biofilm, the rapid drop in IBT concentration attributed to consumption does not occur. These results suggest that an intermediate cell density

would maximize IBT production when using strains that catabolize IBT, and that the IBT productivity is very sensitive to the effect of ammonium concentration. This result suggests that *in situ* control of ammonium level might be useful in optimizing the system's IBT productivity.

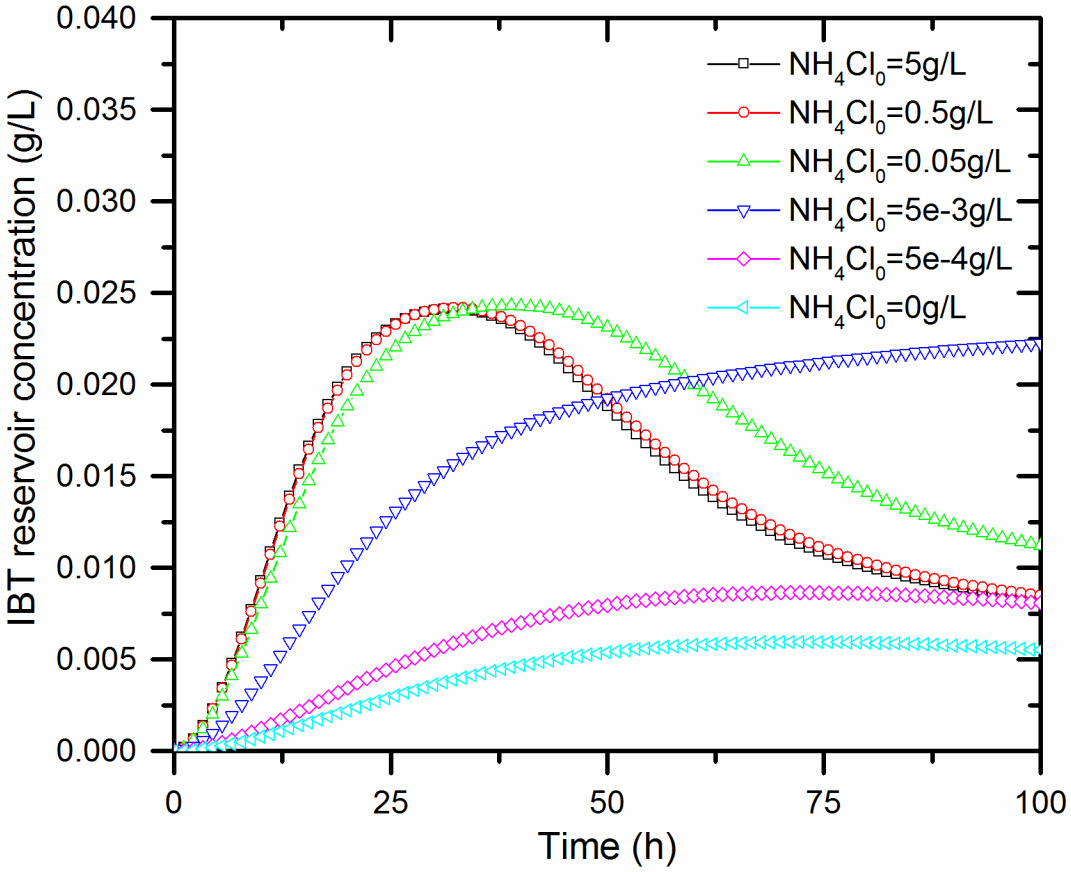

Figure 4.7 IBT concentration at various initial ammonium concentrations.

4.3.2.4 Effect of H_2 Pressure

Since H_2 has the lowest solubility and the highest mass transfer demand among the three gaseous substrates, it is intuitively most likely to be the rate-limiting reactant. Therefore, simulations were carried out to study the extent to which IBT production can be improved when higher H_2 pressure is used in the shell space. Increasing H_2 mass transfer was predicted to increase the predicted IBT concentration (Figure 4.8). Examination of the H_2 and O_2 profiles at

inlet, midpoint and outlet revealed that as the H_2 pressure increases, the higher H_2 availability cause the H_2-O_2 overlap region to be closer to the lumen surface, shrinking the H_2 depletion region and thereby reducing IBT consumption.

However, further increasing H_2 pressure could result in excessive mass transfer, as demonstrated in Figure 4.9. At 200 h and a shell pressure of 4 atm, the H_2 flux into the membrane exceeds the consumption by the cells, leading to a non-zero concentration at the lumen surface. Even though and elevated H_2 level in membrane wall helps curb IBT consumption, it can also result in H_2 diffusion into the liquid flowing through the lumen and subsequent mixing of H_2 and O_2 in the liquid reservoir head space, raising safety concerns.

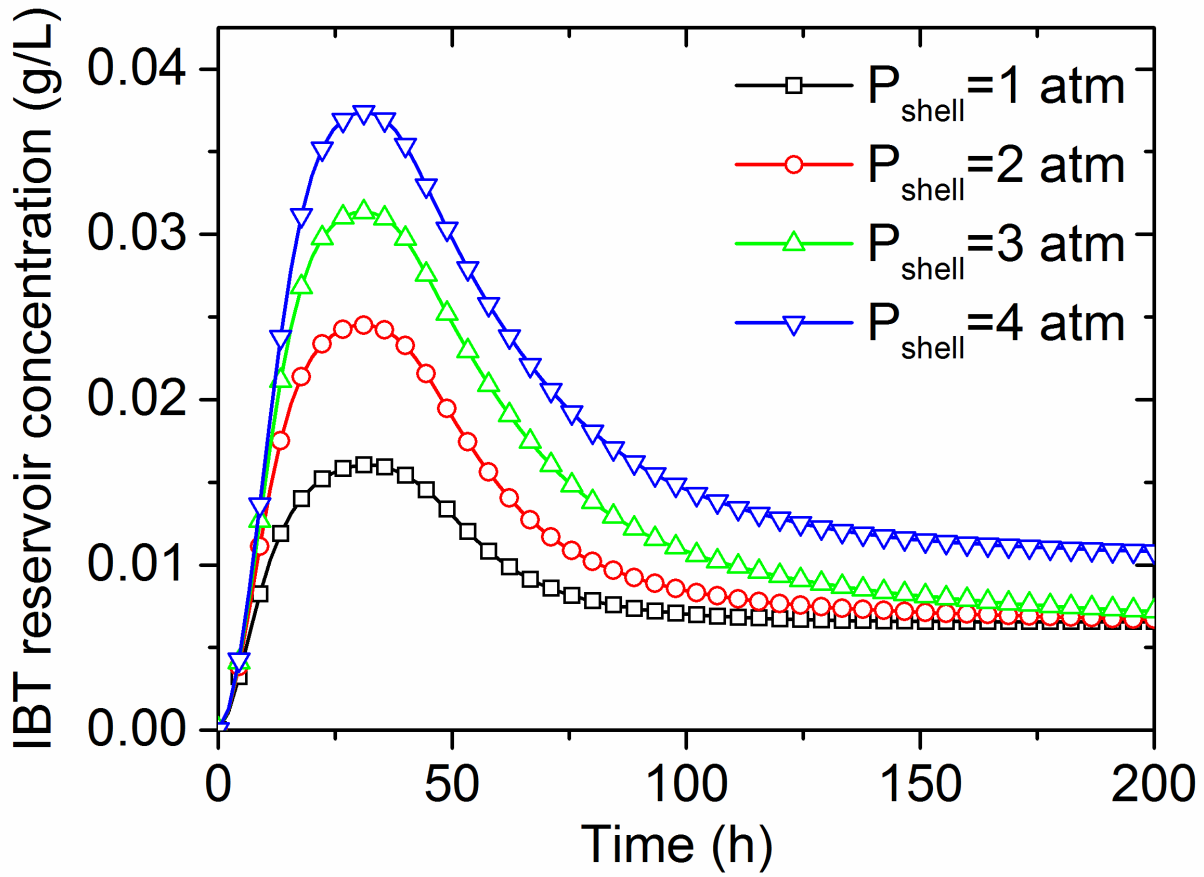

Figure 4.8 Average IBT outlet concentration at various H_2 pressures.

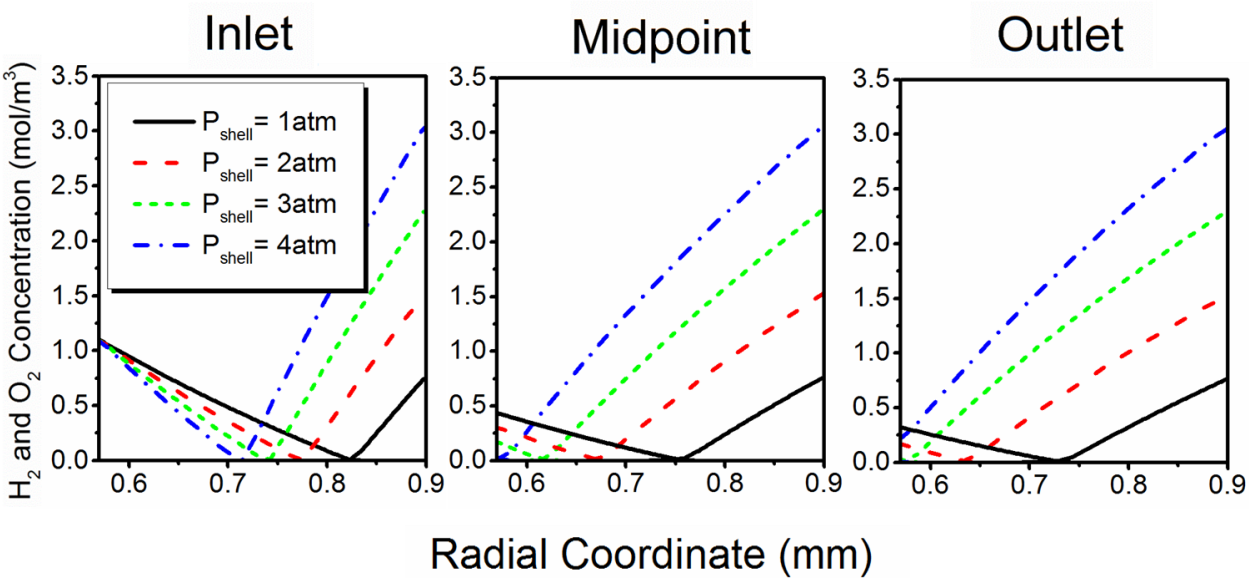

Figure 4.9 H_2 and O_2 concentration profiles at the reactor inlet, midpoint and outlet at 200 h. At the highest shell pressure, H_2 becomes excessive at the outlet, resulting in H_2 and O_2 mixing in the lumen liquid.

4.3.2.5 Effect of Lumen Flow Rates

In most of the BIG experiments, O_2 was provided via the liquid flowing through the lumen. Therefore, the lumen's liquid flow rate affects the O_2 availability to immobilized cells. Simulations were conducted to explore the effect of lumen flow rate on BIG performance. The simulation was initiated with a relatively low ammonium concentration (0.05 g/L). The resulted trends in IBT concentrations in Figure 4.10 showed two distinct inflection points as described below.

In the presence of ammonium (0 h-100 h), increased O_2 availability allows O_2 to penetrate deeper into the immobilized cell layer, and therefore the reaction zone is positioned closer to the shell with higher lumen flow rate (Figure 4.10c), resulting in a larger H_2-depleted zone. Therefore, even though at 50 h a higher O_2 availability yields a higher cell mass, as evidenced by the faster ammonium consumption shown in Figure 4.10a inset and the cell density

distribution in Figure 4.10c, it also encourages IBT consumption. Therefore, the final IBT concentration is lower.

After ammonium depletion (at 100 h, 200 h and 250 h in each case), cell mass generation was immediately halted, causing the carbon flux to be re-directed, creating a surge in IBT production, which soon slowed down due to cell degradation in the absence of ammonium. Eventually IBT consumption became dominant, and the IBT concentration dropped again.

IBT consumption not only competes with IBT production for O_2, it also makes increasing O_2 availability an unsuitable strategy for increasing IBT yield unless H_2 mass transfer limitation is removed. The extent to which IBT consumption is exacerbated by added O_2 is determined by the relative magnitudes of the rate constant for IBT consumption compared to that of IBT production. If IBT consumption occurred at a lower rate, increased O_2 availability would presumably have a significant positive impact on IBT productivity.

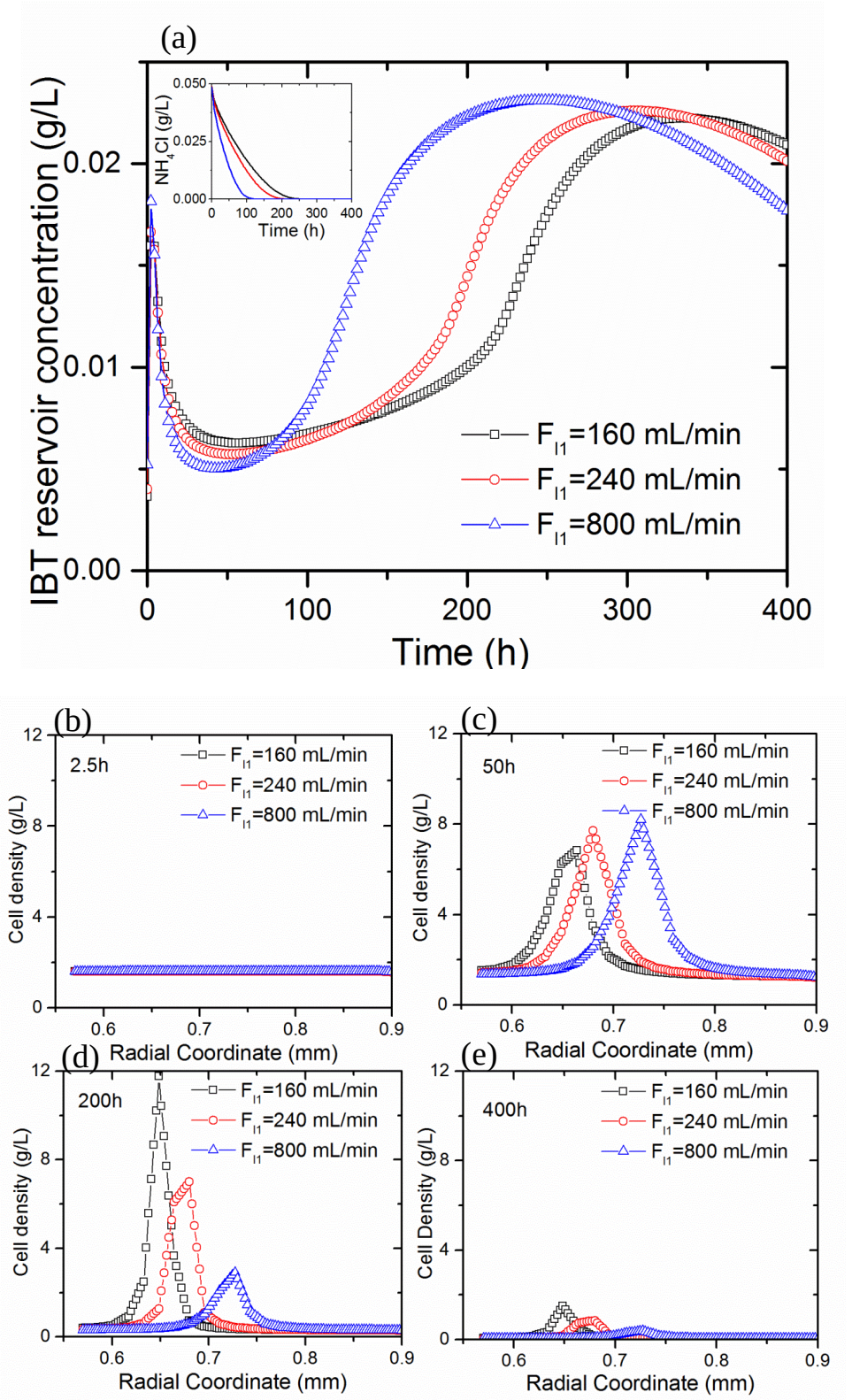

Figure 4.10 Effect of lumen flow rates: (a) reservoir IBT concentration, inset-reservoir NH_4Cl concentration; (b)-(e) cell density distribution at fiber outlet at 2.5h, 50h, 200h and 400h. into the biofilm, where the cell density peak occurs.

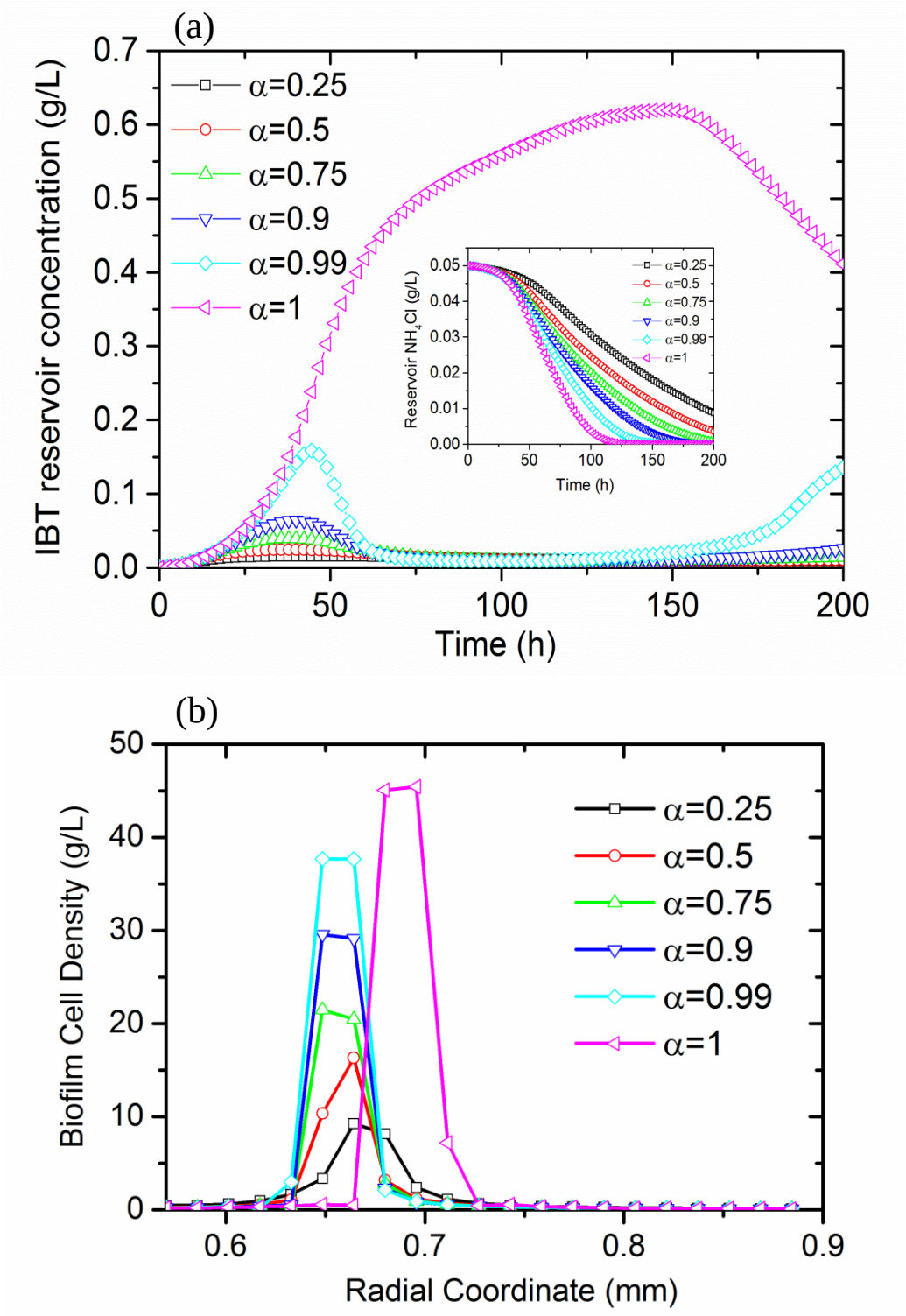

Figure 4.11 (a) Reservoir IBT concentration with an initial NH_4Cl concentration of 0.05g/L at various H_2 preferences. Inset: corresponding reservoir NH_4Cl concentrations. (b) Outlet cell density profiles at 200h.

4.3.2.6 Effect of Substrate Preference

In the kinetic model, the immobilized cells grow both autotrophically on H_2, CO_2 and O_2 and heterotrophically on IBT and O_2 in the presence of NH_4^+ ions. The effects of growth on autotrophic substrates are described by the expression $\frac{\alpha C_{H_2}}{\alpha C_{H_2}+(1-\alpha)C_{IBT}}$, a function of the local ratio of H_2 and IBT concentrations and the strains preference for autotrophic substrates α. An Increased α value could be used to represent progress in strain improvement, such as elimination of carbon sinks in the IBT utilization pathway or increased dehydrogenase activity. An α value of 1 would indicate a "perfect" strain that does not consume the product IBT in the presence of O_2.

Figure 4.11a summarizes the effect of strain improvement on IBT production. With α=0.25-0.99, the reservoir IBT concentration exhibited the hallmark trend of an initial increase followed by a precipitous drop. Even though an increase in the strain's bias towards H_2 from 0.25 to 0.99 increases the IBT peak value from 0.016 g/L to 0.16 g/L, as the reaction zone narrows, the bias towards autotrophic metabolism becomes irrelevant in the H_2-depletion zone as IBT becomes the only source of energy. Since growth on H_2 is faster than that on IBT, the higher cell density as a result of a stronger H_2 preference also causes IBT to be consumed faster. At 100 h, the highest H_2 preference yields the lowest IBT concentration before the trend reverses due to NH_4^+ depletion. The most drastic change comes when the cells' ability to consume IBT is entirely eliminated. The IBT concentration in the reservoir steadily increases until NH_4^+ is depleted and the IBT concentration starts to decrease due to halted production compounded with IBT loss to gas stream in the shell.

The outlet cell density distribution at 200 h (Figure 4.11b) reveals that the more the strain prefers H_2 as the substrate, the faster the cells grow (specific growth rate on autotrophic

substrates are higher than that on IBT), which results in a higher O_2 consumption rate and therefore the H_2-O_2 overlap area lays closer to the lumen. However, with IBT consumption eliminated (preference to H_2 =1), O_2 uptake is lessened and the oxygen profile penetrates further into the biofilm, where the cell density peak occurs (Figure 4.11b).

4.3.2.7 Effect of Product Removal

The model was also used to explore the strategy of reducing IBT consumption by removing IBT as it is produced. As discussed in 4.3.2.5, without IBT recovery, a higher O_2 availability leads to lower IBT concentrations. However, the IBT consumption is encouraged by the presence of IBT in the lumen flow. As the IBT concentration data in Figure 4.10a are converted into IBT production as shown in Figure 4.12a, a negative IBT reaction rate is observed immediately after the initial surge in IBT concentration. The IBT consumption then slows down as IBT concentration significantly decreases, and the IBT net production reaches a dynamic equilibrium with IBT consumption, resulting in a near zero productivity throughout the simulation even under nitrogen limitation (Figure 4.12b).

However, when the simulations are carried out with total IBT recovery, IBT production is strongly encouraged, as can be seen in Figure 4.13a. Because IBT consumption is suppressed by the removal of this product, higher O_2 availability as provided by the higher lumen flow results in a higher productivity, regardless of the nitrogen availability (Figure 4.13b).

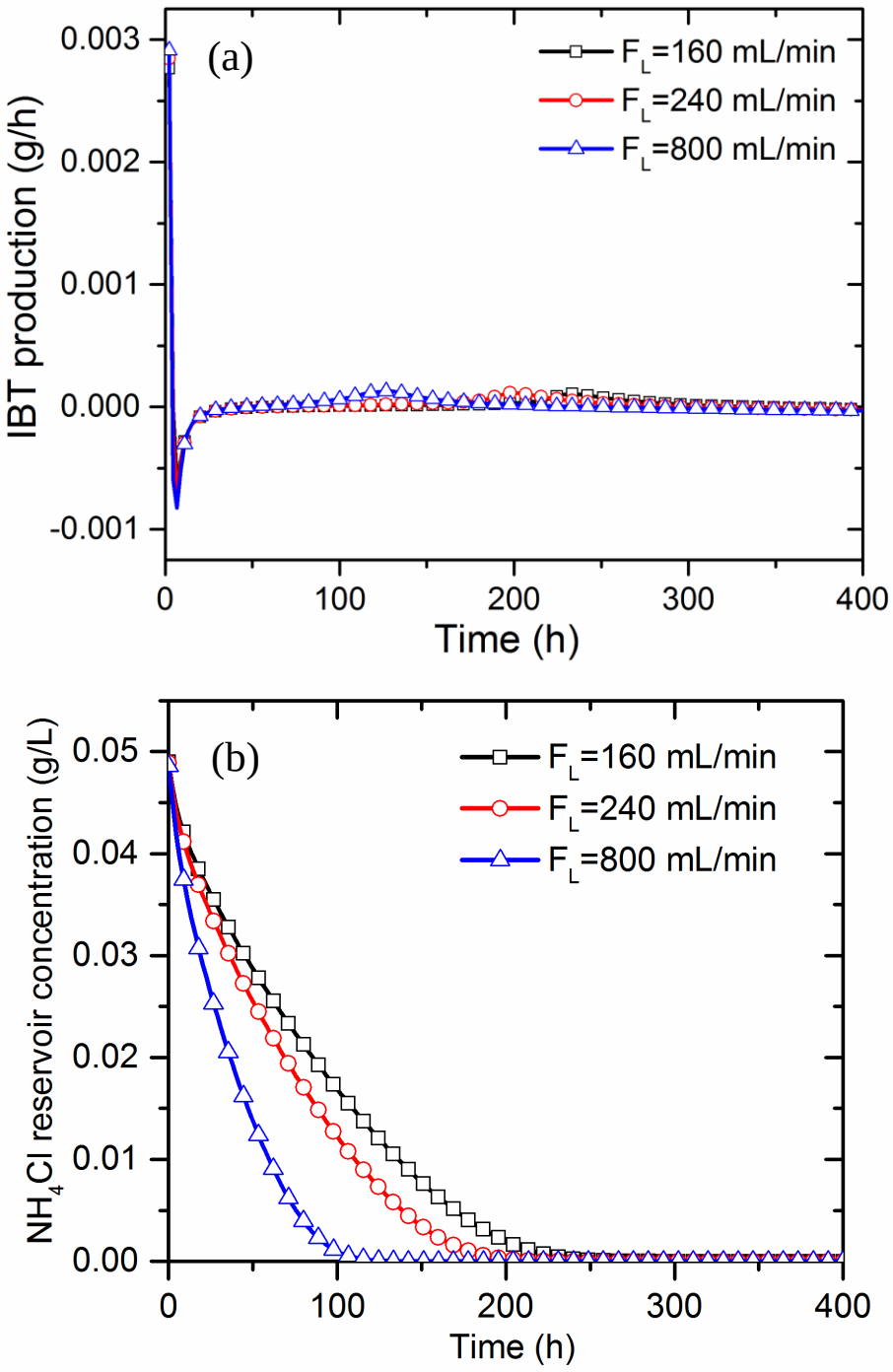

Figure 4.12 (a) IBT production rate; (b) NH_4Cl concentration under various flow rates without IBT recovery.

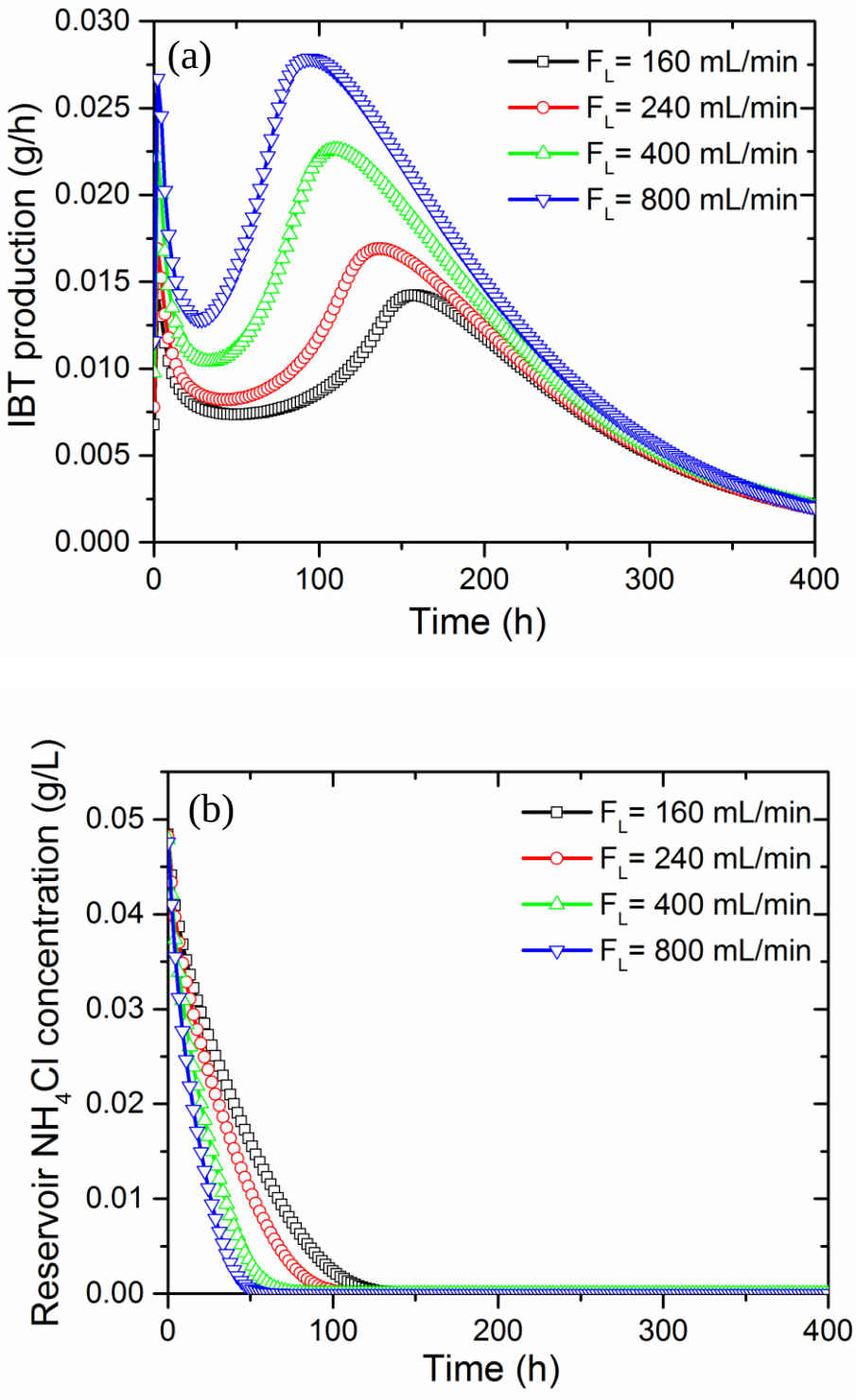

Figure 4.13 (a) IBT production rate; (b) NH_4Cl concentration under various flow rates with IBT recovery.

4.4 Conclusions

The dynamic mathematical model of the BIG takes into account both structured cell kinetics and diffusional mass transfer in a novel hollow fiber based BIG system. The model was used to explore the BIG's dynamics and reproduce non-intuitive experimental results, including a decrease in IBT productivity as the cell concentration increased. The model provides strong support for the hypothesis that IBT consumption is triggered by H_2 limitation, causing the reduction in IBT production. The model's predictions also provide valuable insights that would help fully realize the potential of this reactor design. For example, the following strategies should be considered in designing future generations of the BIG:

(1) optimize membrane thickness and immobilized cell mass based on the highest H_2 flux deliverable by the system;

(2) utilize more robust membrane materials that can endure higher H_2 pressure required for enhanced mass transfer;

(3) monitor ammonium level and employ online control;

(4) recover the product IBT *in situ* to minimize consumption;

(5) if H_2 mass transfer limitation cannot be overcome and IBT cannot be removed from the system *in situ*, operate the reactor under O_2-limiting conditions.

The model could also provide guidance in setting boundaries for operating conditions (O_2 flow rate, ammonium concentration, etc.) and design parameters (fiber length and membrane thickness, etc.) for scale-up of the BIG system.

CONCLUSIONS

The rising availability of CH_4 and solar-derived H_2 makes these gases promising low-cost gas feedstocks for bioconversion processes that are able to produce liquid transportation fuels such as IBT. These energy-rich gases have low aqueous solubilities and their utilization by microbes often requires O_2 as electron acceptor, creating engineering challenges in both mass transfer and process safety. This dissertation focused on developing the first bioreactor that is able to facilitate such processes with enhanced mass transfer and maximized safety. The BIG design concept simultaneously enhances mass transfer of two incompatible gases while preventing formation of hazardous gas-phase mixtures of those gases. The use of hollow fiber membranes to separate a continuous gas phase and a continuous liquid phase that contains microbubbles enables independent control on the mass transfer of each gas by pressurization and/or increased interfacial area.

A bench-scale prototype BIG system was constructed and integrated with an *in situ* IBT recovery system and an Opto22 control network. Continuous autotrophic IBT production by engineered *Ralstonia eutropha* was demonstrated for the first time in both immobilized and planktonic cultures. The IBT productivity was found to increase with cell concentration to a peak value of 325 mg/ (L·day). The productivity then decreased as cell concentration increased further, consistent with the hypothesis that the cells consumed IBT under H_2 limiting conditions.

A dynamic mathematical model was constructed to describe the interactions between mass transfer and cellular kinetics. The model's constants, including using mass transfer coefficients and kinetic constants for a structured kinetic model, were evaluated obtained from experimental results whenever possible. The model was solved using COMSOL Multiphysics®, and the model predictions were used to interpret experimental results from the bench-scale BIG

system under various operating conditions. The simulation results reproduced a counter-intuitive peak in IBT productivity as cell mass increased, providing further verification for our hypothesis that H_2 limitation triggered product consumption in the BIG. The simulation results allowed the effect of system parameters on BIG performance to be elucidated and provided guidance on process optimization strategies to minimize the effects of product consumption and product inhibition. Strategies considered in the modeling studies included enhancing H_2 mass transfer, controlling ammonium concentration regulation, and implementing *in situ* IBT recovery. The mathematical model could be used to aid in future BIG system design and scale-up efforts.

The BIG system developed in this study is the first continuous bioreactor system with the potential to achieve high product yields from incompatible gaseous substrates without forming potentially hazardous gas mixtures, and therefore offers promise in making electrofuels an economically viable option.

APPENDIX

A. Derivation of Rigorous Calculation of Membrane Diffusion Coefficient

The appendix details the derivation of Equation 3.5, 3.8 and 3.14, which describe the relationship between the solute concentration in the reservoir and time. The derivation takes into account the membrane curvature, axial concentration gradient, and system dead volume.

For all species, at a certain reactor length z, the mass balance on a very thin ring in the membrane at a given radius gives the following equation.

$$\frac{1}{r}\frac{d}{dr}\left(r\frac{dC}{dr}\right) = 0 \qquad \text{A.1}$$

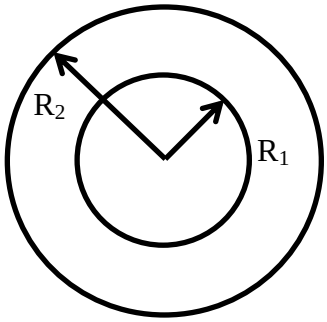

Figure A.1 Cross section of a hollow fiber with inner radius R_1 and outer radius R_2.

$$\frac{d}{dr}\left(r\frac{dC}{dr}\right) = 0 \qquad \text{A.2}$$

$$r\frac{dC}{dr} = N_1 \qquad \text{A.3}$$

$$dC = N_1\frac{dr}{r} \qquad \text{A.4}$$

$$C = N_1 lnr + N_2 \quad \text{A.5}$$

A.1 O_2

Boundary Conditions $C_{O_2}\big|_{r=R_1} = C_{O_2}^o$

$$C_{O_2}\big|_{r=R_2} = 0$$

C_o is the O_2 concentration on the inner surface of membrane

Use the boundary conditions to solve for N_1 and N_2 in A.5

$$N_1 = -\frac{C_{O_2}^o}{lnR_2 - lnR_1}$$

$$N_2 = \frac{C_{O_2}^o lnR_2}{lnR_2 - lnR_1}$$

Hence at a given length,

$$C_{O_2} = -\frac{C_{O_2}^o}{lnR_2 - lnR_1} \cdot lnr + \frac{C_{O_2}^o lnR_2}{lnR_2 - lnR_1} \quad \text{A.6}$$

Where $C_{O_2}^o$ is O_2 concentration at the inner membrane surface at the given fiber length.

The next step is to describe $C_{O_2}^o$ as a function of fiber length assuming no radial concentration gradient in the lumen liquid.

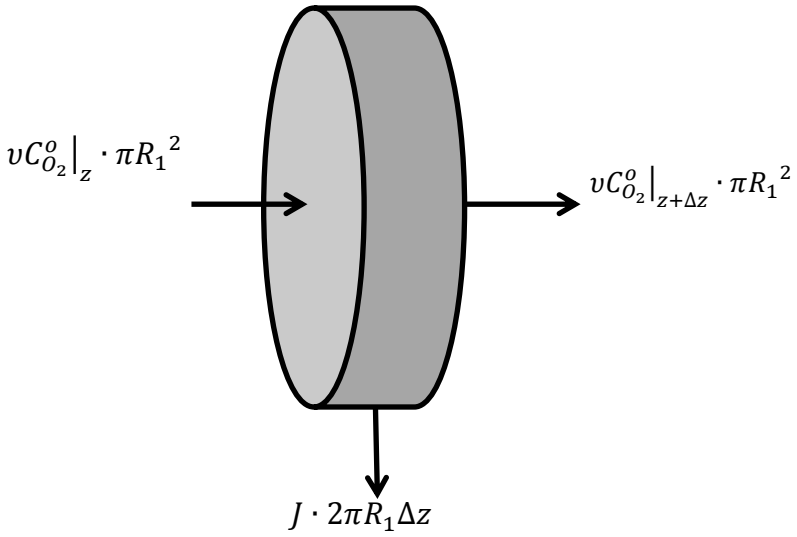

Figure A.2 A thin slice of lumen space with thickness Δz.

At steady state, for a very thin slice of lumen space (thickness Δz)

$$0 = \upsilon C_{O_2}^o\big|_z \cdot \pi {R_1}^2 - \upsilon C_{O_2}^o\big|_{z+\Delta z} \cdot \pi {R_1}^2 - J \cdot 2\pi R_1 \Delta z \quad \text{A.7}$$

$$J = -D_{O_2} \frac{dC_{O_2}^o}{dr}\bigg|_{=R_1} = D_{O_2} \frac{C_{O_2}^o}{lnR_2 - lnR_1} \cdot \frac{1}{R_1} \quad \text{A.8}$$

Substitute A.8 into A.7 gives

$$0 = \upsilon C_{O_2}^o\big|_z \cdot \pi {R_1}^2 - \upsilon C_{O_2}^o\big|_{z+\Delta z} \cdot \pi {R_1}^2 - D_{O_2} \frac{C_{O_2}^o}{lnR_2 - lnR_1} \cdot \frac{1}{R_1} \cdot 2\pi R_1 \Delta z \quad \text{A.9}$$

Dividing both sides by $\pi R_1 \Delta z$ and let $\Delta z \to 0$

$$\upsilon R_1 \frac{dC_{O_2}^o}{dz} = -2D_{O_2} \frac{C_{O_2}^o}{lnR_2 - lnR_1} \cdot \frac{1}{R_1} \quad \text{A.10}$$

Rearranging gives

$$\frac{dC_{O_2}^o}{C_{O_2}^o} = -\frac{2D_{O_2}}{\upsilon {R_1}^2} \frac{dz}{lnR_2 - lnR_1} \quad \text{A.11}$$

Integrate

$$\int_{C_{O_2,reservoir}}^{C_{O_2,outlet}} \frac{dC_{O_2}^o}{C_{O_2}^o} = \int_0^L -\frac{2D_{O_2}}{\upsilon {R_1}^2} \frac{dz}{lnR_2 - lnR_1} \quad \text{A.12}$$

$$lnC_{O_2,outlet} - lnC_{O_2,reservoir} = -\frac{2D_{O_2}}{\upsilon {R_1}^2} \frac{L}{lnR_2 - lnR_1} \quad \text{A.13}$$

$$\upsilon = \frac{F_L}{N\pi {R_1}^2} \quad \text{A.14}$$

$$lnC_{O_2,outlet} - lnC_{O_2,reservoir} = -\frac{2D_{O_2}\pi NL}{F_L ln\frac{R_2}{R_1}} \quad \text{A.15}$$

Since the lumen liquid is recycled from a reservoir, consider the reservoir

$$V_{reservoir} \frac{dC_{O_2,reservoir}}{dt} = F_L(C_{O_2,outlet} - C_{O_2,reservoir}) \quad \text{A.16}$$

Rearranging A.15

$$C_{O_2,outlet} = C_{O_2,reservoir} exp\left(-\frac{2D_{O_2}\pi NL}{F_L ln\frac{R_2}{R_1}}\right) \quad \text{A.17}$$

Substitute A.17 into A.16 yields

$$V_{reservoir}\frac{dC_{O_2,reservoir}}{dt} = F_L C_{O_2,reservoir}\left(exp\left(-\frac{2D_{O_2}\pi NL}{F_L ln\frac{R_2}{R_1}}\right) - 1\right) \quad \text{A.18}$$

Rearrange and integrate

$$V_{reservoir}\frac{dC_{O_2,reservoir}}{C_{O_2,reservoir}} = F_L\left(exp\left(-\frac{2D_{O_2}\pi NL}{F_L ln\frac{R_2}{R_1}}\right) - 1\right)dt \quad \text{A.19}$$

$$\int_{C_{O_2,reservoir,0}}^{C_{O_2,reservoir}} V_{reservoir}\frac{dC_{O_2,reservoir}}{C_{O_2,reservoir}} = \int_0^t F_L\left(exp\left(-\frac{2D_{O_2}\pi NL}{F_L ln\frac{R_2}{R_1}}\right) - 1\right)dt \quad \text{A.20}$$

$$lnC_{O_2,reservoir} = \frac{F_L}{V_R}\left(exp\left(-\frac{2D_{O_2}\pi NL}{F_L ln\frac{R_2}{R_1}}\right) - 1\right)t + lnC_{O_2,reservoir,0} \quad \text{A.21}$$

Therefore there is a linear relationship between natural log of reservoir concentration and time, and the slope is $\frac{F_L}{V_{reservoir}}\left(exp\left(-\frac{2D_{O_2}\pi NL}{F_L ln\frac{R_2}{R_1}}\right) - 1\right)$

A.2 Isobutanol

The derivation for isobutanol is the same as O_2.

A.3 CO_2

Assuming the outer surface concentration is always in equilibrium with the partial pressure in the shell.

Boundary Conditions $C_{CO_2}\big|_{r=R_1} = 0$

$$C_{CO_2}\big|_{r=R_2} = C^o_{CO_2} = k_{H,CO_2} P_{CO_2}$$

$C^o_{CO_2}$ is the CO_2 concentration on the outer surface of membrane

Use the boundary conditions to solve for N_1 and N_2 in A.5

$$N_1 = \frac{C^o_{CO_2}}{lnR_2 - lnR_1}$$

$$N_2 = -\frac{C^o_{CO_2} lnR_1}{lnR_2 - lnR_1}$$

Hence at a given length,

$$C_{CO_2} = \frac{C^o_{CO_2}}{lnR_2 - lnR_1} \cdot lnr - \frac{C^o_{CO_2} lnR_1}{lnR_2 - lnR_1} \quad \text{A.22}$$

Where $C^o_{CO_2}$ is CO_2 concentration at the outer membrane surface at the given fiber length.

The next step is to describe $C^o_{CO_2}$ as a function of fiber length assuming no radial concentration gradient in the shell gas.

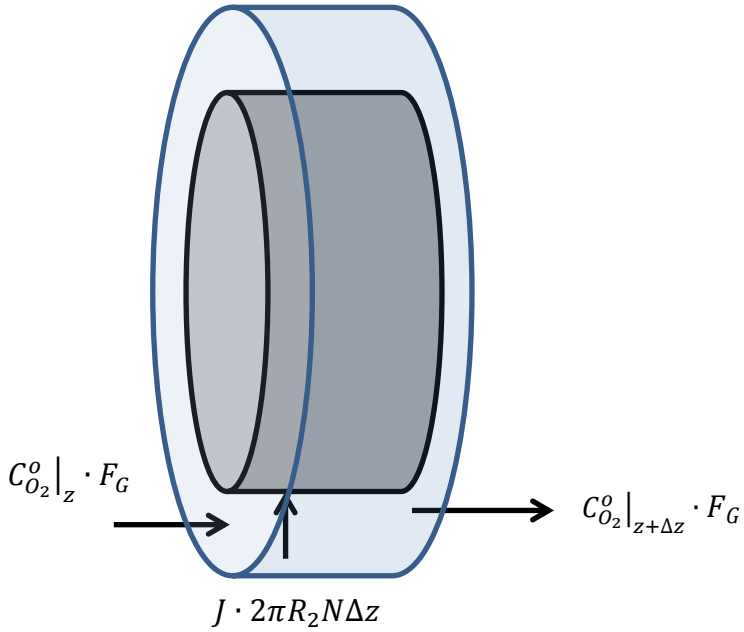

Figure A.3 A thin slice of the annular shell space with thickness Δz.

At steady state, for a very thin slice of shell space (thickness Δz)

$$0 = C^o_{CO_2}\big|_z \cdot F_G - C^o_{CO_2}\big|_{z+\Delta z} \cdot F_G - J \cdot 2\pi R_2 N \Delta z \qquad \text{A.23}$$

$$J = -D_{CO_2} \frac{dC^o_{CO_2}}{dr}\bigg|_{r=R_2} = -D_{CO_2} \frac{C^o_{CO_2}}{lnR_2 - lnR_1} \cdot \frac{1}{R_2} \qquad \text{A.24}$$

The negative sign here means the flux direction is towards the center of cross section area where radius is smaller.

Substitute A.24 into A.23 gives

$$0 = \left.\frac{P_{CO_2}}{RT}\right|_z \cdot F_G - \left.\frac{P_{CO_2}}{RT}\right|_{z+\Delta z} \cdot F_G - D_{CO_2} \frac{C_{O_2}^o}{lnR_2 - lnR_1} \cdot \frac{1}{R_2} \cdot 2\pi R_2 N \Delta z \quad \text{A.25}$$

Dividing both sides by Δz and let $\Delta z \to 0$

$$\frac{F_G}{RT}\frac{dP_{CO_2}}{dz} = -2\pi N D_{CO_2} \frac{C_{O_2}^o}{lnR_2 - lnR_1} = -2\pi N D_{CO_2} \frac{k_{H,CO_2} P_{CO_2}}{lnR_2 - lnR_1} \quad \text{A.26}$$

Rearranging gives

$$\frac{dP_{CO_2}}{P_{CO_2}} = -2\pi N D_{CO_2} \frac{k_{H,CO_2}}{lnR_2 - lnR_1} \cdot \frac{RT}{F_G} dz \quad \text{A.27}$$

Integrate

$$\int_{P_{CO_2,reservoir}}^{P_{CO_2,outlet}} \frac{dP_{CO_2}}{P_{CO_2}} = -2\pi N D_{CO_2} \frac{k_{H,CO_2}}{lnR_2 - lnR_1} \cdot \frac{RT}{F_G} dz \quad \text{A.28}$$

$$lnP_{CO_2,outlet} - lnP_{CO_2,reservoir} = -2\pi N D_{CO_2} L \frac{k_{H,CO_2}}{lnR_2 - lnR_1} \cdot \frac{RT}{F_G} \quad \text{A.29}$$

$$lnP_{CO_2,outlet} - lnP_{CO_2,reservoir} = -\frac{2\pi N D_{CO_2} L k_{H,CO_2} RT}{F_G ln\frac{R_2}{R_1}} \quad \text{A.30}$$

Since the lumen liquid is recycled from a reservoir, consider the mass balance on the reservoir liquid:

$$V_{reservoir} \frac{dC_{CO_2,resevoir}}{dt} = F_G(C_{O_2,outlet} - C_{O_2,reservoir}) \quad \text{A.31}$$

$$V_{reservoir} \frac{dP_{CO_2,reservoir}}{\cancel{RT}dt} = F_G(\frac{P_{CO_2,outlet}}{\cancel{RT}} - \frac{P_{CO_2,reservoir}}{\cancel{RT}}) \quad \text{A.32}$$

Rearranging A.15

$$P_{CO_2,outlet} = P_{CO_2,reservoir} exp\left(-\frac{2\pi N D_{CO_2} L k_{H,CO_2} RT}{F_G ln\frac{R_2}{R_1}}\right) \quad \text{A.33}$$

Substitute A.33 into A.32 yields

$$V_{resrvoir}\frac{dP_{CO_2,reservoir}}{dt} = F_G P_{CO_2,reservoir}(exp\left(-\frac{2\pi N D_{CO_2} L k_{H,CO_2} RT}{F_G ln\frac{R_2}{R_1}}\right) - 1) \quad \text{A.34}$$

Rearrange and integrate

$$V_{reservoir}\frac{dP_{CO_2,reservoir}}{P_{CO_2,reservoir}} = F_G(exp\left(-\frac{2\pi N D_{CO_2} L k_{H,CO_2} RT}{F_G ln\frac{R_2}{R_1}}\right) - 1)dt \quad \text{A.35}$$

$$\int_{P_{CO_2,reservoir,0}}^{P_{CO_2,reservoir,t}} V_{reservoir}\frac{dP_{CO_2,reservoir}}{P_{CO_2,reservoir}} = \int_0^t F_G(exp\left(-\frac{2\pi N D_{CO_2} L k_{H,CO_2} RT}{F_G ln\frac{R_2}{R_1}}\right) - 1)dt \quad \text{A.36}$$

$$lnP_{CO_2,reservoir} = \frac{F_G}{V_{reservoir}}\left(exp\left(-\frac{2\pi N D_{CO_2} L k_{H,CO_2} RT}{F_G ln\frac{R_2}{R_1}}\right) - 1\right)t + lnP_{CO_2,reservoir,0} \quad \text{A.37}$$

Therefore, there is a linear relationship between natural log of reservoir concentration and time, and the slope is $\frac{F_G}{V_{reservoir}}\left(exp\left(-\frac{2\pi N D_{CO_2} L k_{H,CO_2} RT}{F_G ln\frac{R_2}{R_1}}\right)-1\right)$.

REFERENCES

REFERENCES

1. Flavin, C., *Alternative energy sources.* Applied Energy, 1994. **47**(2-3): p. 123-146.

2. Ogden, J.M. and R.H. Williams, *Solar hydrogen: Moving beyond fossil fuels*. 1989. Medium: X; Size: Pages: (131 p).

3. Gnansounou, E. and A. Dauriat, *Techno-economic analysis of lignocellulosic ethanol: A review.* Bioresource Technology, 2010. **101**(13): p. 4980-4991.

4. Lynd, L.R., et al., *Fuel ethanol from cellulosic biomass.* Science, 1991. **251**(4999): p. 1318-23.

5. Wooley, R., et al., *Process Design and Costing of Bioethanol Technology: A Tool for Determining the Status and Direction of Research and Development.* Biotechnology Progress, 1999. **15**(5): p. 794-803.

6. Govindjee, G.a.R.; Available from: http://www.life.illinois.edu/govindjee/whatisit.htm.

7. Corporation, S., *E20/435 solar panel document*, S. Corporation, Editor.

8. Eggeman, T. and R.T. Elander, *Process and economic analysis of pretreatment technologies.* Bioresource Technology, 2005. **96**(18): p. 2019-2025.

9. Jiang, H., et al., *Methanotrophs: Multifunctional bacteria with promising applications in environmental bioengineering.* Biochemical Engineering Journal, 2010. **49**(3): p. 277-288.

10. Brigham, C., et al., *Engineering Ralstonia eutropha for Production of Isobutanol from CO_2, H_2, and O_2*, in *Advanced Biofuels and Bioproducts*, J.W. Lee, Editor. 2013, Springer New York. p. 1065-1090.

11. Raghoebarsing, A.A., et al., *A microbial consortium couples anaerobic methane oxidation to denitrification.* Nature, 2006. **440**(7086): p. 918-921.

12. Pohlmann, A., et al., *Genome sequence of the bioplastic-producing "Knallgas" bacterium Ralstonia eutropha H16.* Nat Biotech, 2006. **24**(10): p. 1257-1262.

13. Bredwell, M.D., P. Srivastava, and R.M. Worden, *Reactor design issues for synthesis-gas fermentations.* Biotechnology Progress, 1999. **15**(5): p. 834-844.

14. Brigham, C.J., et al., *Engineering Ralstonia eutropha for Production of Isobutanol from CO2, H2, and O2*, in *Advanced Biofuels and Bioproducts* J.W. Lee, Editor. 2012, Springer Science New York.

15. Lynd, L., *Application of material and energy balances to biological systems*, in *Chemical engineering problems in biotechnology*, M. Shuler, Editor. 1989, American Institute of Chemical Engineers New York. p. 29-49.

16. Sun, Y. and J. Cheng, *Hydrolysis of lignocellulosic materials for ethanol production: a review.* Bioresource Technology, 2002. **83**(1): p. 1-11.

17. Connor, M.R. and J.C. Liao, *Microbial production of advanced transportation fuels in non-natural hosts.* Current Opinion in Biotechnology, 2009. **20**(3): p. 307-315.

18. Karabektas, M. and M. Hosoz, *Performance and emission characteristics of a diesel engine using isobutanol-diesel fuel blends.* Renewable Energy, 2009. **34**(6): p. 1554-1559.

19. Gui, F., N. Sridhar, and M. Peters, *Compatibility Of Carbon Steel With Isobutanol*, NACE International.

20. Klasson, K.T., et al., *Bioconversion of synthesis gas into liquid or gaseous fuels.* Enzyme and Microbial Technology, 1992. **14**(8): p. 602-608.

21. Park, J.H., S. Kim, and A.J. Bard, *Novel Carbon-Doped TiO2 Nanotube Arrays with High Aspect Ratios for Efficient Solar Water Splitting.* Nano Letters, 2005. **6**(1): p. 24-28.

22. Hou, Y., et al., *Bioinspired molecular co-catalysts bonded to a silicon photocathode for solar hydrogen evolution.* Nat Mater, 2011. **10**(6): p. 434-438.

23. Bolton, J.R., *Solar photoproduction of hydrogen: A review.* Solar Energy, 1996. **57**(1): p. 37-50.

24. Schlegel, H. and R. Lafferty, *Novel energy and carbon sources A. The production of biomass from hydrogen and carbon dioxide*, in *Advances in Biochemical Engineering, Volume 1*. 1971, Springer Berlin / Heidelberg. p. 143-168.

25. Kim, B.S., et al., *Production of poly(3-hydroxybutyric acid) by fed-batch culture of Alcaligenes eutrophus with glucose concentration control.* Biotechnology and Bioengineering, 1994. **43**(9): p. 892-898.

26. Sinskey, A. and R.M. Worden, *Engineering Ralstonia eutropha for Production of Isobutanol (IBT) Motor Fuel from Carbon Dioxide, Hydrogen and Oxygen*. 2010, The US Department of Energy.

27. Atsumi, S., W. Higashide, and J.C. Liao, *Direct photosynthetic recycling of carbon dioxide to isobutyraldehyde.* Nat Biotech, 2009. **27**(12): p. 1177-1180.

28. Glassner, D.A., M. Peters, and P.R. Gruber. *Hydrocarbon Fuels from Plant Biomass*. in *31st Symposium on Biotechnology for Fuels and Chemicals*. 2009. San Francisco, CA.

29. Ishizaki, A., K. Tanaka, and N. Taga, *Microbial production of poly-D-3-hydroxybutyrate from CO2.* Applied Microbiology and Biotechnology, 2001. **57**(1-2): p. 6-12.

30. Park, J., T. Kim, and S. Lee, *Genome-scale reconstruction and in silico analysis of the Ralstonia eutropha H16 for polyhydroxyalkanoate synthesis, lithoautotrophic growth, and 2-methyl citric acid production.* BMC Systems Biology, 2011. **5**(1): p. 101.

31. Patwardhan, P.R. and A.K. Srivastava, *Model-based fed-batch cultivation of R. eutropha for enhanced biopolymer production.* Biochemical Engineering Journal, 2004. **20**(1): p. 21-28.

32. Volova, T.G. and N.A. Voinov, *Kinetic Parameters of a Culture of the Hydrogen-Oxidizing Bacterium Ralstonia eutropha Grown under Conditions Favoring Polyhydroxybutyrate Biosynthesis.* Applied Biochemistry and Microbiology, 2003. **39**(2): p. 166-170.

33. Lu, J., et al., *Studies on the production of branched-chain alcohols in engineered Ralstonia eutropha.* Applied Microbiology and Biotechnology, 2012: p. 1-15.

34. Bredwell, M.D., P. Srivastava, and R.M. Worden, *Reactor Design Issues for Synthesis Gas Fermentations.* Biotechnology Progress, 1999. **15**(5): p. 834-844.

35. Worden, R.M., M.D. Bredwell, and A.J. Grethlein, *Engineering Issues in Synthesis-Gas Fermentations*, in *Fuels and Chemicals from Biomass*. 1997, American Chemical Society. p. 320-335.

36. Klasson, K.T., et al., *Bioreactors for synthesis gas fermentations.* Resources, Conservation and Recycling, 1991. **5**(2-3): p. 145-165.

37. Ungerman, A.J. and T.J. Heindel, *Carbon Monoxide Mass Transfer for Syngas Fermentation in a Stirred Tank Reactor with Dual Impeller Configurations.* Biotechnology Progress, 2007. **23**(3): p. 613-620.

38. Klasson, K.T., et al., *Bioreactor design for synthesis gas fermentations.* Fuel, 1991. **70**(5): p. 605-614.

39. Datar, R.P., et al., *Fermentation of biomass-generated producer gas to ethanol.* Biotechnology and Bioengineering, 2004. **86**(5): p. 587-594.

40. Bredwell, M.D. and R.M. Worden, *Mass-Transfer Properties of Microbubbles. 1. Experimental Studies.* Biotechnology Progress, 1998. **14**(1): p. 31-38.

41. Chatterjee, S., et al., *Evaluation of support matrices for an immobilized cell gas lift reactor for fermentation of coal derived synthesis gas.* Journal of Fermentation and Bioengineering, 1996. **81**(2): p. 158-162.

42. Hawkins, A.S., et al., *Biological conversion of carbon dioxide and hydrogen into liquid fuels and industrial chemicals.* Current Opinion in Biotechnology, 2013. **24**(3): p. 376-384.

43. Toone, E. and H. de Winde, *Energy biotechnology in 2013: advanced technology development for breakthroughs in fuels and chemicals production.* Current Opinion in Biotechnology, 2013. **24**(3): p. 367-368.

44. Atsumi, S., T. Hanai, and J.C. Liao, *Non-fermentative pathways for synthesis of branched-chain higher alcohols as biofuels.* Nature, 2008. **451**(7174): p. 86-89.

45. Tanaka, K., et al., *Production of poly(D-3-hydroxybutyrate) from CO2, H2, and O2 by high cell density autotrophic cultivation of Alcaligenes eutrophus.* Biotechnology and Bioengineering, 1995. **45**(3): p. 268-275.

46. Wang, J. and H.-Q. Yu, *Biosynthesis of polyhydroxybutyrate (PHB) and extracellular polymeric substances (EPS) by Ralstonia eutropha ATCC 17699 in batch cultures.* Applied Microbiology and Biotechnology, 2007. **75**(4): p. 871-878.

47. Dean, J.A., *Lange's Handbook of Chemistry*. 1992: McGraw-Hill, Inc.

48. Ferrell, R.T. and D.M. Himmelblau, *Diffusion coefficients of hydrogen and helium in water.* AIChE Journal, 1967. **13**(4): p. 702-708.

49. Cussler, E.L., *Diffusion: Mass transfer in fluid systems*. 1997: Cambridge Univ Pr.

50. Vologa, T., *Hydrogen-Based Biosynthesis*. 2010: Nova Science Publishers Inc, New York, NY.

51. Weber, J. and F. Agblevor, *Microbubble fermentation of Trichoderma reesei for cellulase production.* Process Biochemistry, 2005. **40**(2): p. 669-676.

52. Munasinghe, P.C. and S.K. Khanal, *Biomass-derived syngas fermentation into biofuels: Opportunities and challenges.* Bioresource Technology, 2010. **101**(13): p. 5013-5022.

53. Hensirisak, P., et al., *Scale-Up of Microbubble Dispersion Generator for Aerobic Fermentation.* Applied Biochemistry and Biotechnology, 2002. **101**(3): p. 211-228.

54. GE. *ZeeWeed* Hollow-Fiber Membranes*. [webpage]; Available from: http://www.gewater.com/products/zeeweed-500-membrane.html.

55. Siemens. *MEMCOR® CP - Ultrafiltration System* Available from: http://www.water.siemens.com/en/products/membrane_filtration_separation/ultrafiltration_membrane_systems/Pages/memcor_product_cp_membrane_system.aspx.

56. Freeman, A., T. Blank, and Y. Aharonowitz, *Protein determination of cells immobilized in cross-linked synthetic gels.* Applied Microbiology and Biotechnology, 1982. **14**(1): p. 13-15.

57. *Diffusion in Polymers*. 1968, London and New York: Academic Press.

58. Crank, J., *The mathematics of diffusion*. 1979: Oxford university press.

59. Mignot, L. and G.-A. Junter, *Diffusion in immobilized-cell agar layers: influence of microbial burden and cell morphology on the diffusion coefficients ofl-malic acid and glucose.* Applied Microbiology and Biotechnology, 1990. **32**(4): p. 418-423.

60. Hannoun, B.J.M. and G. Stephanopoulos, *Diffusion coefficients of glucose and ethanol in cell-free and cell-occupied calcium alginate membranes.* Biotechnology and Bioengineering, 1986. **28**(6): p. 829-835.

61. Ruthven, D.M., *Diffusion through Porous Media: Ultrafiltration, Membrane Permeation and Molecular Sieving.* 2009.

62. Qi, Z. and E.L. Cussler, *Microporous hollow fibers for gas absorption : II. Mass transfer across the membrane.* Journal of Membrane Science, 1985. **23**(3): p. 333-345.

63. Ergas, S.J., et al., *Membrane process for biological treatment of contaminated gas streams.* Biotechnology and Bioengineering, 1999. **63**(4): p. 431-441.

64. Renkin, E.M., *Filtration, diffusion, and molecular sieving through porous cellulose membranes.* J Gen Physiol, 1954. **38**(2): p. 225-43.

65. Matsunaga, T., I. Karube, and S. Suzuki, *Some observations on immobilized hydrogen-producing bacteria: Behavior of hydrogen in gel membranes.* Biotechnology and Bioengineering, 1980. **22**(12): p. 2607-2615.

66. Sakaki, K., T. Nozawa, and S. Furusaki, *Effect of intraparticle diffusion in ethanol fermentation by immobilized Zymomonas mobilis.* Biotechnology and Bioengineering, 1988. **31**(6): p. 603-606.

67. Pluen, A., et al., *Diffusion of Macromolecules in Agarose Gels: Comparison of Linear and Globular Configurations.* Biophysical Journal. **77**(1): p. 542-552.

68. Klein, J., J. Stock, and K.D. Vorlop, *Pore size and properties of spherical Ca-alginate biocatalysts.* European journal of applied microbiology and biotechnology, 1983. **18**(2): p. 86-91.

69. Guo, L. and P.H. Santschi, *Ultrafiltration and its Applications to Sampling and Characterisation of Aquatic Colloids*, in *Environmental Colloids and Particles*. 2007, John Wiley & Sons, Ltd. p. 159-221.

70. Stewart, P.S., *A review of experimental measurements of effective diffusive permeabilities and effective diffusion coefficients in biofilms.* Biotechnology and Bioengineering, 1998. **59**(3): p. 261-272.

71. Ghosh, R.N., et al., *Optical dissolved oxygen sensor utilizing molybdenum chloride cluster phosphorescence.* Applied Physics Letters, 2011. **98**(22): p. 221103-221103-3.

72. Sander, R., *Compilation of Henry's Law Constants for Inorganic and Organic Species of Potential Importance in Environmental Chemistry (Version 3)*. 1999.

73. Lewis, J.B., *Some determinations of liquid-phase diffusion coefficients by means of an improved diaphragm cell.* Journal of Applied Chemistry, 1955. **5**(5): p. 228-237.

74. Krasuk, J.H. and J.M. Smith, *Mass transfer in a pulsed column.* Chemical Engineering Science, 1963. **18**(9): p. 591-598.

75. Han, H.S., et al., *Effect of flow pulsation on mass transport in a cathode channel of polymer electrolyte membrane fuel cell.* Journal of Power Sources, 2012. **213**(0): p. 145-155.

76. Saremirad, P., H.G. Gomaa, and J. Zhu, *Effect of flow oscillations on mass transfer in electrodialysis with bipolar membrane.* Journal of Membrane Science, 2012. **405–406**(0): p. 158-166.

77. Gupta, B.B., P. Blanpain, and M.Y. Jaffrin, *Permeate flux enhancement by pressure and flow pulsations in microfiltration with mineral membranes.* Journal of Membrane Science, 1992. **70**(2–3): p. 257-266.

78. Ishizaki, A. and K. Tanaka, *Batch culture of Alcaligenes eutrophus ATCC 17697^T using recycled gas closed circuit culture system.* Journal of Fermentation and Bioengineering, 1990. **69**(3): p. 170-174.

79. Bowien, B. and H.G. Schlegel, *Physiology and Biochemistry of Aerobic Hydrogen-Oxidizing Bacteria.* Annual Review of Microbiology, 1981. **35**(1): p. 405-452.

80. Komen, R., K. Schmidt, and B. Friedrich, *Hydrogenase mutants of Alcaligenes eutrophus H16 show alterations in the electron transport system.* FEMS Microbiol Lett, 1992. **75**(2-3): p. 173-8.

81. Cramm, R., *Genomic view of energy metabolism in Ralstonia eutropha H16.* J Mol Microbiol Biotechnol, 2009. **16**(1-2): p. 38-52.

82. Ratledge, C. and B. Kristiansen, *Basic Biotechnology*. 3rd ed. Basic Biotechnology. 2006: Cambridge University Press.

83. Monod, J., *La technique de culture continue. Théorie et applications.* Ann. Inst. Pasteur, 1950. **79**: p. 390-410.

84. Fredrickson, A.G., *Formulation of structured growth models.* Biotechnology and Bioengineering, 1976. **18**(10): p. 1481-1486.

85. Sonnleitner, B., et al., *Formal Kinetics of Poly-Beta-Hydroxybutyric Acid (PHB) Production in Alcaligenes eutrophus H16 And Mycoplana Rubra R14 With Respect to the Dissolved-Oxygen Tension in Ammonium-Limited Batch Cultures.* European Journal of Applied Microbiology and Biotechnology, 1979. **7**(1): p. 1-10.

86. Votruba, J., B. Volesky, and L. Yerushalmi, *Mathematical model of a batch acetone–butanol fermentation.* Biotechnology and Bioengineering, 1986. **28**(2): p. 247-255.

87. Du, G., et al., *Continuous production of poly-3-hydroxybutyrate by Ralstonia eutropha in a two-stage culture system.* Journal of Biotechnology, 2001. **88**(1): p. 59-65.

88. Lee, S.Y., *Bacterial polyhydroxyalkanoates.* Biotechnology and Bioengineering, 1996. **49**(1): p. 1-14.

89. Hills, B.P. and K.M. Wright, *A New Model for Bacterial Growth in Heterogeneous Systems.* Journal of Theoretical Biology, 1994. **168**(1): p. 31-41.

90. Volkmer, B. and M. Heinemann, *Condition-Dependent Cell Volume and Concentration of Escherichia coli to Facilitate Data Conversion for Systems Biology Modeling.* PLoS ONE, 2011. **6**(7): p. e23126.

91. Kovárová-Kovar, K. and T. Egli, *Growth Kinetics of Suspended Microbial Cells: From Single-Substrate-Controlled Growth to Mixed-Substrate Kinetics.* Microbiology and Molecular Biology Reviews, 1998. **62**(3): p. 646-666.

92. Lendenmann, U. and T. Egli, *Kinetic models for the growth of Escherichia coli with mixtures of sugars under carbon-limited conditions.* Biotechnology and Bioengineering, 1998. **59**(1): p. 99-107.

93. Siegel, R.S. and D.F. Ollis, *Kinetics of growth of the hydrogen-oxidizing* bacterium *Alcaligenes eutrophus* (ATCC 17707) in chemostat culture. Biotechnology and Bioengineering, 1984. **26**(7): p. 764-770.

94. Hawkins, A.C. and C.S. Harwood, *Chemotaxis of Ralstonia eutropha JMP134 (pJP4) to the herbicide 2, 4-dichlorophenoxyacetate.* Applied and environmental microbiology, 2002. **68**(2): p. 968-972.